AI-Enabled Optimization of 3D-Printed Microneedles for Simultaneous Epidermal and Dermal Delivery

by

Misagh Rezapour Sarabi

A Dissertation Submitted to the
Graduate School of Sciences and Engineering
in Partial Fulfillment of the Requirements for
the Degree of
Doctor of Philosophy
in
Biomedical Sciences and Engineering

KOÇ ÜNİVERSİTESİ

June 13, 2024

AI-Enabled Optimization of
3D-Printed Microneedles for
Simultaneous Epidermal and Dermal Delivery

Koç University
Graduate School of Sciences and Engineering
This is to certify that I have examined this copy of a doctoral dissertation by

Misagh Rezapour Sarabi

and have found that it is complete and satisfactory in all respects,
and that any and all revisions required by the final
examining committee have been made.

Committee Members:

Assoc. Prof. Savaş Taşoğlu

Assoc. Prof. Seçil Vural

Prof. İsmail Lazoğlu

Assoc. Prof. Ali K. Yetisen

Assoc. Prof. Zihni Onur Uygun

Prof. Metin Sitti

Date: June 13, 2024

TO THE BEAUTY AND MAGNIFICENCE OF OCEANS,

MY EVER-BLUE SOURCE OF INSPIRATION

AND

TO THE YOUNGER ME, WHO DARED TO DREAM.

ABSTRACT

AI-Enabled Optimization of 3D-Printed Microneedles for Simultaneous Epidermal and Dermal Delivery

Misagh Rezapour Sarabi

Doctor of Philosophy in Biomedical Sciences and Engineering

June 13, 2024

Conventional needle technologies are being revolutionized by nano- and micro-fabrication methods to create microneedles, organization of microscale needles on an array, which aim to reduce penetration pain and tissue damage while providing precise channels for administering bioagents and collecting body fluids. This thesis explores the advancements in 3D printing methods for microneedle fabrication and particularly focusing on their applications in biomedical engineering and healthcare. For the case of sampling body fluids, a finger-actuated microneedle array integrated with a microfluidic chip was visualized for simple and efficient self-collection of blood and interstitial fluid, eliminating the need for healthcare workers. The processes of fluid extraction and flow within the device were simulated to optimize efficiency. The thesis also explores the integration of artificial intelligence in 3D printing of microneedles, using machine learning and deep learning algorithms to optimize manufacturing processes and predict fabrication outcomes. This multidisciplinary approach enhances the quality control and precision of biodegradable microneedles fabricated through fused deposition modeling 3D printing and chemical etching. In the context of biomedical applications, for the case of Basal Cell Carcinoma skin cancer treatment, microneedles loaded with Marshmallow root extract and Imiquimod are explored, offering controlled release and targeted delivery with minimal side effects. This approach enhances therapeutic efficacy while minimizing patient discomfort and infection risks. Another significant focus is on the customization of microneedle arrays for treating various skin diseases, such as skin cancers and infections, which occur at different skin depths. By engineering the design of the microneedles in nonlinear ways with diverse needle heights on the array, the thesis introduces concurrent drug delivery to various skin layers. Additionally, varying the base diameter of the needles in the array facilitates prolonged or intermittent drug release, depending on the biodegradation kinetics of these needles. This approach enabled long-lasting simultaneous epidermal and dermal drug delivery. The thesis concludes that microneedle arrays hold significant potential in drug delivery due to their ability to administer treatments in a painless and minimally invasive manner, paving the way for more personalized and advanced healthcare solutions.

ÖZETÇE

Eşzamanlı Epidermal ve Dermal ilaç teslimat için 3D baskılı mikroiğnelerin yapay zeka destekli optimizasyonu

Misagh Rezapour Sarabi

Biyomedikal Bilimler ve Mühendisliği Doktora

13 Haziran 2024

Geleneksel iğne teknolojilerinde nano ve mikro üretim yöntemleriyle devrim yaratılıyor. Bu yöntemler, bir yama veya dizi üzerinde mikro ölçekli iğnelerin organizasyonu olan mikroiğneler oluşturabilir. Mikroiğneler, biyoajanların uygulanması ve vücut sıvılarının toplanması için hassas kanallar sağlarken, penetrasyon ağrısını ve doku hasarını azaltmayı amaçlamaktadır. Bu tez, mikroiğne üretimi için 3 boyutlu baskı yöntemlerindeki gelişmeleri araştırıyor ve özellikle biyomedikal mühendisliği ve sağlık alanındaki uygulamalarına odaklanıyor. Vücut sıvılarının örneklenmesi durumunda, kanın ve interstisyel sıvının basit ve etkili bir şekilde kendi kendine toplanması için mikroakışkan bir çip ile entegre edilmiş, parmakla çalıştırılan bir mikroiğne dizisi görselleştirildi ve cihaz, sağlık çalışanlarına olan ihtiyacı ortadan kaldırdı. Cihaz içindeki sıvı çıkarma ve akış işlemlerin verimliliğini optimize etmek için simülasyon yapıldı. Tez aynı zamanda üretim süreçlerini optimize etmek ve üretim sonuçlarını tahmin etmek için makine öğrenimi ve derin öğrenme algoritmalarını kullanarak yapay zekanın mikroiğnelerin 3 boyutlu baskısına entegrasyonunu da araştırıyor. Bu multidisipliner yaklaşım, kaynaştırılmış biriktirme modelleme 3D baskı ve kimyasal gravür yoluyla üretilen biyolojik olarak parçalanabilen mikroiğnelerin kalite kontrolünü ve hassasiyetini artırır. Bazal Hücreli Karsinom cilt kanseri tedavisi durumunda, Marshmallow kökü ekstraktı ve Imiquimod yüklü mikroiğneler araştırılarak, minimum yan etkiyle kontrollü salım ve hedefe yönelik teslimat sunulmaktadır. Bu yaklaşım, hastanın rahatsızlığını ve enfeksiyon riskini en aza indirirken terapötik etkinliği artırır. Bir diğer önemli odak noktası ise farklı cilt derinliklerinde meydana gelen cilt kanserleri ve enfeksiyonlar gibi çeşitli cilt hastalıklarının tedavisi için mikroiğne dizilerinin özelleştirilmesidir. Mikroiğnelerin tasarımını dizi üzerinde farklı iğne yükseklikleriyle doğrusal olmayan şekillerde tasarlayarak tez, çeşitli cilt katmanlarına eş zamanlı ilaç dağıtımını sağlar. Ek olarak dizideki iğnelerin taban çapının değiştirilmesi, bu iğnelerin biyolojik bozunma kinetiğine bağlı olarak uzun süreli veya aralıklı ilaç salınımını kolaylaştırır. Bu yaklaşım, uzun süreli eş zamanlı epidermal ve dermal ilaç dağıtımını mümkün kıldı. Tez, mikroiğne dizilerinin, tedavileri ağrısız ve minimal invaziv bir şekilde uygulama yetenekleri nedeniyle ilaç dağıtımında önemli bir potansiyele sahip olduğu ve daha kişiselleştirilmiş ve gelişmiş sağlık çözümlerinin önünü açtığı sonucuna varıyor.

ACKNOWLEDGMENTS

Coming to an end to the episode of my life in Koç University, I will take the chance to express my thankfulness to the people whom I have shared this adventure with. This thesis could not have existed without a crowded cast of supervisors, colleagues, collaborators, friends, good friends, better friends, best friends, family, and life partner, who all provided limitless intellectual, physical, and emotional support during the past years, and who gave me the courage to open my wings.

To my supervisor Savaş, a great thank you for your guidance over the past five years, for all the scientific support, for always pushing me to challenge my limits, for giving me the opportunity to pursue my ideas and helping to shape them together and teaching me soft skills that empowered me the most.

To my co-supervisor Metin, a big thank you for your guidance and scientific support and offering me the opportunity to visit Max Planck Institute for Intelligent Systems which helped me a lot for personal growth and stepping into international cooperation.

To our collaborator Ali, a great thank you to your scientific support by being in my committee, and your super-fast responding and reviewing. And a heartfelt thank you for accepting and supporting my authentic self. Our talk in Cihangir Roof while having Aperol has been and will be a true inspirational moment for me.

To our collaborator Seçil, thank you for accepting to be in my committee and putting your valuable time and input, especially in the dermatological and pathobiological aspects.

To our collaborator Onur, thank you for accepting to be in my committee and putting your valuable time and input in reviewing my thesis.

And the biggest thank you to myself, for believing in me, for being my authentic self, and for chasing my dreams.

TABLE OF CONTENTS

List of Tables

List of Figures

Abbreviations

3D	Three Dimensional
AI	Artificial Intelligence
CAD	Computer-Aided Design
DL	Deep Learning
FDM	Fused Deposition Modeling
H&E	Hematoxylin and Eosin
ISF	Interstitial Fluid
ML	Machine Learning
MN	Microneedle
MNA	Microneedle Array
PBS	Phosphate Buffered Saline
PDMS	Polydimethylsiloxane
PMMA	Poly Methyl Methacrylate
PVA	Polyvinyl Alcohol
RhB	Rhodamine B
SLA	Stereolithography
UV	Ultraviolet

Chapter 1: Introduction

Conventional needle technologies can be advanced with emerging nano- and micro-fabrication methods to fabricate microneedles. Nano-/micro-fabricated microneedles (MNs) seek to mitigate penetration pain and tissue damage, as well as providing accurately controlled robust channels for administrating bioagents and collecting body fluids. MNs introduced a novel injection alternative to conventional needles, offering a decreased administration pain and phobia along with more efficient delivery mechanism. MNs are devices composed of various materials such as polymers, ceramics, and metals, designed with the purpose of epidermal and intradermal delivery of vaccines, bioactive molecules, or recreational agents and also collecting substances and bio-signals from the body (Chang, Zheng, Yu, Than, Seeni, Kang, Tian, Khanh, Liu, et al., 2017; Ren et al., 2017) while decreasing insertion pain and minimizing tissue damage.

The first report of the term "microneedle" dates back to 1921 (Chambers, 1921), as a means of micro-dissection of echinoderm eggs. The concept of MNs for drug delivery was reported in 1971, including both solid and hollow MNs (Gerstel & Place, 1976). Subsequently, the first drug-coated MN was patented in 1975 (Pistor, 1975). In 1998, the first use of MN for in vivo studies was reported (Henry et al., 1998), followed by genetic material delivery (2001) (Bevers, 2001), vaccine delivery by MNs (2002) (Mikszta et al., 2002), MN assisted delivery of nano-particles (2003) (McAllister et al., 2003), dissolvable MNs (2005) (Miyano et al., 2005), hollow MNs for sample extraction (2005) (Mukerjee et al., 2004; Wang et al., 2005), cosmetic application of MNs (2005) (Fernandes, 2005), and MNs in diagnostic applications (2005) (Bhatnagar et al., 2017).

MNs are an emerging subset of vehicles to exploit the physiology of skin tissue, the human body's largest organ with an area around 1.5-2.0 m^2 on an adult (Gallo, 2017). **Figure 1.1** depicts the inner structure and different layers of human skin. In terms of anatomical and histological structure, cutaneous tissue is a waterproof external barrier to prevent the entrance of different biomolecules into the body while this natural structure is helpful for *in situ* and systemic delivery of therapeutic agents (Yang et al., 2019). Cutaneous tissue consists of three layers: epidermis, dermis, and hypodermis (Figure 1b). The epidermis is the outermost of the three layers composed of tightly packed epithelial cells with a continuous sheet. Histologically, the epidermis is made up of two distinct layers stratum corneum and viable epidermis. Stratum corneum which consists of dead keratinized epithelial cells, has a thickness of 10-40 μm. The hydrophobic nature of stratum corneum prohibits the entry of biomolecules and exogenous components. The epidermis layer has multilayer epithelial cell sheets of 100-200 μm thickness. The dermis is a dense connective tissue that harbors blood vessels, nerves, hair follicles, and sebaceous and sweat glands (Russell et al., 2008). The hypodermis (subcutaneous layer) lies beneath the dermis and is composed of loosely fatty and connective tissues (Ni et al., 2020). Therefore, MNs with proper design and size, can pierce the outermost layer of skin and reach underneath layers to either deliver drugs and reagents, or to acquire signals or samples.

Fabrication strategies for MNs include micromilling (wet and/or dry cutting) (García-López et al., 2018), wet and dry etching (Y. Li et al., 2019), photolithography which can also be combined with thermal- and photo-

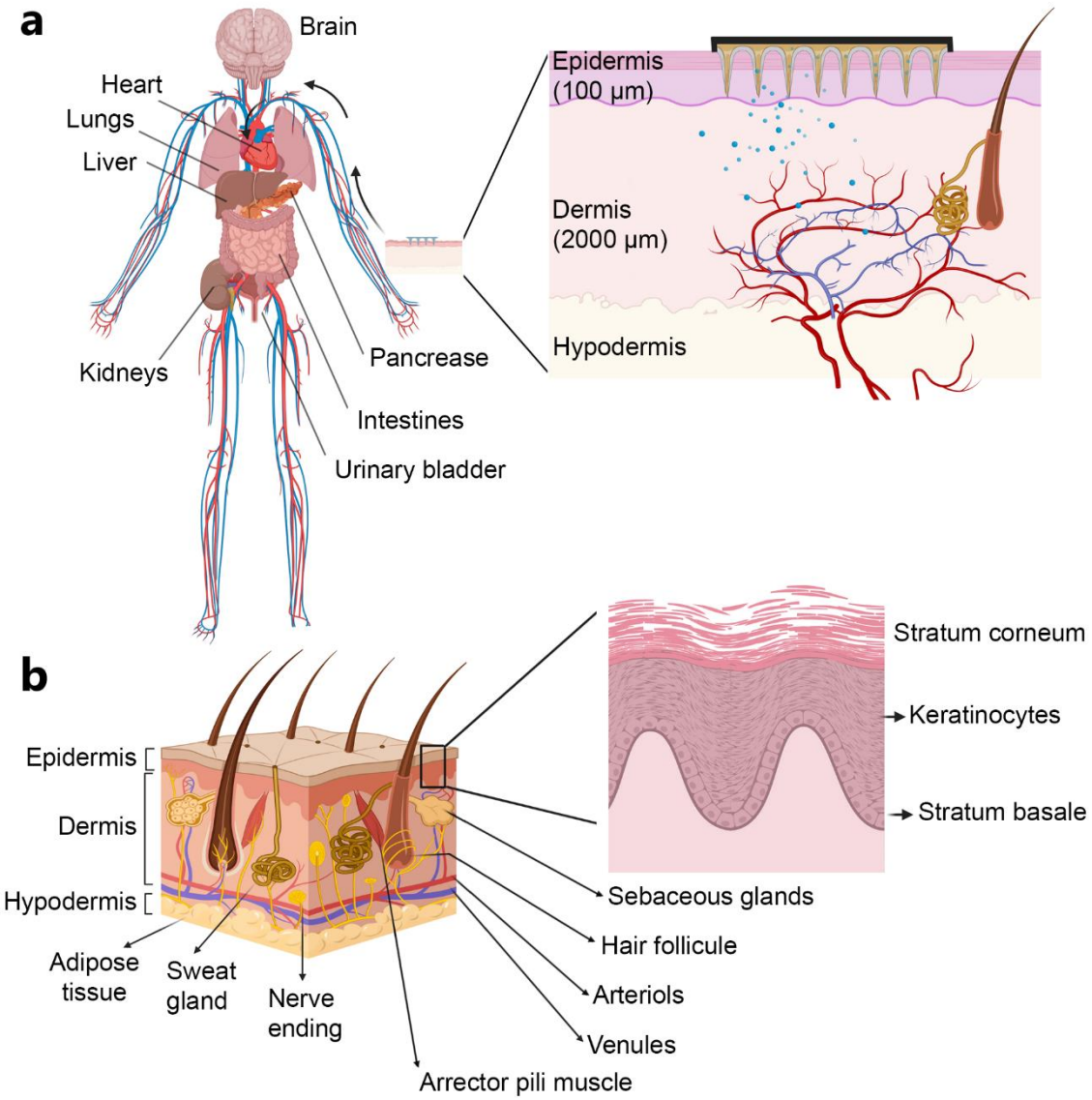

Fig 1.1. The main purpose of the microneedles (MNs) patch application is to deliver the active biomolecules to the close or remote sites inside the body. (A) A cutaneous tissue consists of three layers: epidermis, dermis, and hypodermis. (B) The outermost layer, the epidermis, is a keratinized stratified squamous epithelium with closely packed epithelial cells. The dermis layer lies beneath the epidermis and is composed of connective tissue with vessels and nerves ending. The innermost layer of the skin is so-called hypodermis, which is characterized by the loose connective tissue and the existence of adipocytes.

polymerization (Kathuria et al., 2020; Knowlton, Yenilmez, et al., 2017), molding based techniques (H. Chen et al., 2019), cleanroom-free molding (Nejad et al., 2018a), injection molding (Li et al., 2017), laser patterning (Donnelly et al., 2011), drawing lithography (Chen et al., 2018), and photolithography with an elasto-capillarity-driven self-assembly mechanism (Lim et al., 2018). Many of these conventional fabrication methods have some limitations in cost-efficiency, require manual steps, and are labor-intensive. Hence, accessible, and cost-efficient technologies are needed for the production of MNs.

3D printing is an additive manufacturing process that creates structures, prototypes, and architectures in a layer-by-layer fashion via the translation of a 3D computer-aided design (CAD) model input to a physical object. The process of 3D printing can be categorized as: vat polymerization, material extrusion, material as well as binder jetting, and powder bed fusion (Ligon et al., 2017). Each 3D printing method has a unique set of tradeoffs in resolution, cost-efficiency, biocompatibility, and output volume, enabling the use of 3D printing in a wide range of applications (Bakhshinejad & D'souza, 2015; Park et al., 2015). The ability to use biomaterials in 3D printing processes (Chia & Wu, 2015), along with microscale and nanoscale 3D printing (You et al., 2018), can enable the fabrication of a wide range of laboratory instruments, clinical and point-of-care applications (Aimar et al., 2019; Amin, Knowlton, Yenilmez, et al., 2016; Douroumis, 2019; Stephanie Knowlton, Chu Hsiang Yu, et al., 2015; Yenilmez, Knowlton, & Tasoglu, 2016) including organ-on-a-chip devices (Jain et al., 2020; Knowlton & Tasoglu, 2016; Knowlton, Yenilmez, & Tasoglu, 2016; Knowlton, Yu, et al., 2016), tissue engineering (Knowlton et al., 2018; Sears et al., 2016; L. Zhang et al., 2019), wound healing (Joseph et al., 2019; Tabriz et al., 2020), fertility and embryology research (Kanakasabapathy et al., 2019; S. M. Knowlton et al., 2015; Potluri et al., 2018), cancer research (Knowlton, Joshi, et al., 2016; Stephanie Knowlton, Sevgi Onal, et al., 2015), stem cell research (Javaid & Haleem, 2020; Tasoglu & Demirci, 2013) and circulating tumor cell isolation (Chen et al., 2020). 3D printing can address the limitations in the fabrication of MNs and microneedle arrays (MNAs).

Here in this thesis, in the next chapter, 3D printing methods are introduced from the perspective of materials and technology. Emerging applications of 3D printed MNs in biomedical engineering and healthcare systems are reviewed. These applications include drugs or bioagents delivery, sample extraction from the human body (Economidou et al., 2019; Luzuriaga et al., 2018; Miller et al., 2018), single-cell analysis (Kavaldzhiev et al., 2017), and biological signal acquisition (Ren et al., 2017). The application of MNs for minimally invasive biological fluid sampling is rapidly emerging, offering a user-friendly approach with decreased insertion pain and less harm to the tissues compared to conventional needles. In the third chapter, a finger actuated MNA integrated with a microfluidic chip was conceptualized to extract body fluid samples. Actuated by finger pressure, the microfluidic device enables an efficient approach for the user to collect their own body fluids in a simple and fast manner without the requirement for a healthcare worker. The processes for extracting human blood and interstitial fluid (ISF) from the body and the flow across the device, estimating the amount of the extracted fluid were simulated. The design in this work can be utilized for the minimally invasive personalized medical equipment offering a simple usage procedure.

3D printing methods have emerged in the field of MNs for their time- and cost-efficient manufacturing. Tuning 3D printing parameters with artificial intelligence (AI), including machine learning (ML) and deep learning (DL), is an emerging multidisciplinary field for optimization of manufacturing biomedical devices. In the fourth chapter, an AI framework is presented to assess and predict 3D-printed MN features. Biodegradable MNs were fabricated using fused deposition modeling (FDM) 3D printing technology followed by chemical etching to enhance their geometrical precision. DL was used for quality control and anomaly detection in the fabricated MNAs. Ten different MN designs and various etching exposure doses were used create a data library to train ML models for extraction of similarity metrics in order to predict new fabrication outcomes when the

mentioned parameters were adjusted. The integration of AI-enabled prediction with 3D printed MNs will facilitate the development of new healthcare systems and advancement of MNs' biomedical applications.

Different skin diseases, such as cancers, inflammatory conditions, and bacterial infections, manifest at distinct skin depths. MNAs, recognized for their painless and minimally invasive drug administration, can be customized to penetrate these layers simultaneously. In the fifth chapter, the design of the MNs is engineered in non-linear ways with diverse needle heights on the array enabling concurrent drug delivery to various skin layers. Additionally, varying the base diameter of the needles in the array facilitates prolonged or intermittent drug release, depending on the biodegradation kinetics of these needles. MNs, microfabricated with a biocompatible and biodegradable polymer, were validated by skin administration. The non-linear design of the MNs on the array introduces a novel perspective on addressing skin diseases at varying depths of the skin.

Basal Cell Carcinoma (BCC) is a prevalent form of skin cancer with increasing global incidence, primarily affecting sun-exposed areas. Traditional treatments, while effective, can lead to scarring and recurrence. MNAs offer a promising alternative, delivering drugs directly to the target site with minimal side effects. Marshmallow root extract (MRE) and Imiquimod are two compounds showing potential for BCC treatment, but their controlled delivery to the tumor site remains a challenge. In the sixth chapter, MRE-Imiquimod-loaded MNAs as a novel approach for BCC treatment is presented, offering controlled release, minimal invasiveness, enhanced efficacy, and sustainability. MNAs can be engineered to gradually release the drugs, ensuring sustained therapeutic levels while reducing patient discomfort and infection risk. By directly targeting the tumor, MRE-Imiquimod-loaded MNAs have the potential to enhance therapeutic efficacy while minimizing systemic exposure. This study explores the use of MAs to facilitate controlled drug delivery for localized BCC treatment, combining the therapeutic potential of natural medication with controlled and targeted drug delivery.

In the last chapter, it is concluded that MNAs have garnered considerable attention within the realm of drug delivery, owing to their noteworthy characteristics, particularly the ability to administer substances in a painless and minimally invasive manner. Hence, they can further contribute to advancements in drug delivery methodologies utilizing MNAs and enable more personalized treatment procedures.

Chapter 2: 3D-Printed Microneedles in Biomedical Applications

2.1 Fabrication of MNs

2.1.1 Design Structures and Materials

MNs are classified into coated, solid, hollow, hydrogel-based, porous, and swellable formats, which can feature complex shapes such as honeybee inspired, angled, and arrow-head MNs (**Figure 2.1**) (Camović et al., 2019; Kevin J. Krieger et al., 2019). Enabling high-throughput fabrication of MNs requires a high uniformity in their structures (Nejad et al., 2018a). Several geometrical factors such as MNs' height, width, aspect ratio, and tip thickness should be considered in the design and fabrication process to reach a final product with optimized mechanical integrity, desired target capacity of the inserted drug, robust extraction of signals, and the minimized pain by the patient. For example, a higher aspect ratio of needles can lead to a more convenient insertion, less pain, but weaker mechanical strength and integrity (Kevin J. Krieger et al., 2019; Mansor et al., 2019).

A diverse range of materials has been reported in the fabrication of MNs. These include polymers, metals, and inorganic materials (Ali et al., 2020; Bhatnagar et al., 2019; Gholami et al., 2019; Zhu, Zhou, Kim, et al., 2020). While the group of inorganics, such as glass, silicon, and ceramics, and a group of metals, including titanium and aluminum, were initially used for the fabrication of MNs, recently polymers and hydrogels have been of higher interest because of the need for biodegradable and dissolvable MNs. Polymeric MNs have become feasible by advances in polymer science, and the emergence of new fabrication tools such as

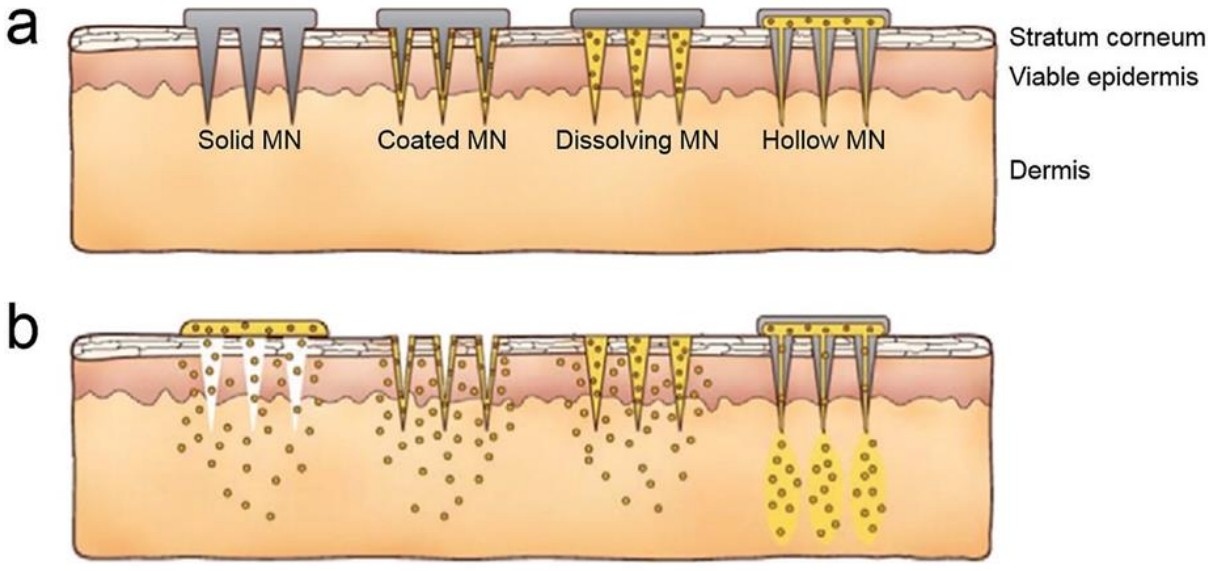

Fig 2.1. An illustration of the different types of microneedles (MNs) and delivery means. (a) The most common types of MNs are solid, coated, dissolving, and hollow. (b) MNs pass drugs through the outermost layers of skin to deliver desired cargo to the dermis layer, with different approaches. Adapted with permission from (Kim et al., 2012). Copyright 2013, Elsevier.

3D printing (Bhatnagar et al., 2019). **Table 2.1** shows the typical materials used in 3D printing technologies.

Table 2.1. Most common additive manufacturing methods, used material, spatial resolution, advantages, and drawbacks of each.

Method	Typical Materials	Resolution	Advantages	Drawbacks
SLA	Resins with photo-active monomers acrylates – epoxides (Ligon et al., 2017) - DC 100 (high accuracy) - DC 500 - DL 350/360 (high flexibility) - AB 001 - GM 08 (high flexibility) - DM 210 - DM 220 -	10 µm (Ngo et al., 2018)	Fine spatial resolution - high quality (Ngo et al., 2018) - good surface quality - good precision (Ligon et al., 2017)	Supports limited materials - slow printing - expensive (Ngo et al., 2018) - poor biocompatibility - limited mechanical properties (Ligon et al., 2017)
DLP (Ligon et al., 2017)	Acrylates - epoxides - plas range (High resolution and chemically resistant) - superCAST - superWAX	25-100 µm	High printing accuracy - low cost - shorter build time than SLA - less affected by oxygen inhibition compared to SLA - better surface quality - low initial vat volume is needed	Limited mechanical properties
CLIP (Ligon et al., 2017)	Acrylates - rigid polyurethane (RPU) - flexible polyurethane (EPU) (impact resistant) - elastomeric polyurethane - cyanate ester (CE) - prototyping (PR) -	75 µm	Higher build speed than DLP	Low viscosity resin is needed

TPP / MPP (Ligon et al., 2017)	Acrylates	100 nm - 5 µm	High spatial resolution	Low build speed - limited material
Powder-bed Based Methods (SLS-SLM)	Compact fine powder metals - alloys and limited polymers (Ngo et al., 2018) - PA12 – PEEK (Ligon et al., 2017) Titanium (biocompatible) - Stainless Steel - Aluminum - Cobalt/Chrome - Nickel based alloys	50 – 250 µm (Ligon et al., 2017)	Fine resolution - high quality - durable - large surface area, good for scaffolds of tissue engineering - good mechanical properties (SLM) - less anisotropy (Ligon et al., 2017)	Slow printing - expensive - porosity - lower mechanical properties due to the porous structure (SLS) - high power supply - high printing temp - rough surface - poor reusability of unsintered powder (Ligon et al., 2017)
FDM	Continuous filament of thermoplastic polymers - continuous fiber-reinforced polymers (Ngo et al., 2018) – PLA (Ligon et al., 2017) - ABS - ASA - Nylon 12 - PC - PPSF/PPSU - PEI or ULTEM (Biocompatible) - PLA – TPU	50 - 200 µm (Ngo et al., 2018)	Low cost - high speed – simplicity (Ngo et al., 2018)	Weak mechanical properties - limited material (thermoplastics) – layer-by-layer finish (Ngo et al., 2018) - rough surface - high temperature during the extrusion process (incompatible for cells) (Ligon et al., 2017)
3D dispensing (Ligon et al., 2017)	Thermoplastics - photoresins - composites - hydrogels - biomaterials	100 µm - 1cm	Wide range of materials	Rough surface - narrow viscosity process window
3D printing (Binder jetting) (Ligon et al., 2017)	Strech - PLA - ceramics	100 µm	Fast - allow multi-material AM	Rough surface - limited strength of parts
Inkjet printing	A concentrated dispersion of particles in a	5-200 µm	Quick printing	Weak adhesion between layers

(Ngo et al., 2018)	liquid (Ink or paste)			
PolyJet (Ligon et al., 2017)	Acrylates - veroWhitePlus - digital ABS - fullcure RGD 720 - rigur RGD 450 - biocompatible Mterial	25 µm	Fast - allow multimaterial AM	Low viscosity ink is needed
Direct Energy deposition (DED) (Ngo et al., 2018)	Metals and alloys in the form of powder or wire ceramics and polymers	250 µm	Reduced manufacturing time and cost - Good mechanical properties - Accurate composition control - Good for repair and retrofitting	Low accuracy - Low surface quality - Dense support structure is needed - Limitation in printing complex shapes

2.1.2 Introduction to 3D Printing Technologies

Stereolithography (SLA), one of the earliest 3D printing technologies (Amin, Knowlton, Hart, et al., 2016), works based on photochemical processes in which, using ultraviolet (UV) light and a digital micromirror device, a photocurable liquid polymer is cured in a layer-by-layer process to shape the product (Amin, Knowlton, Hart, et al., 2016; Ghaderinezhad et al., 2020; Quan et al., 2020; Yenilmez, Knowlton, et al., 2016). Digital light processing (DLP) is another 3D printing technology, similar to SLA, which uses several mirrors along with a lightbulb, instead of UV light, to cure the photopolymer to shape the final structure (Zhang et al., 2020). Additionally, curing in the SLA method is in a point-to-point manner while in DLP each layer is cured at once (Ligon et al., 2017; Zhang et al., 2020).

Multiphoton polymerization (MPP) is another method of 3D printing, featuring high resolution for the fabrication of structures in submicron scales. An MPP 3D printer consists of an fs laser and pairs of laser scanners. By focusing the laser beam to a highly restricted region, the nonlinear absorption of two or more photons by polymers solidifies the photoresist in the exposed regions (Geng et al., 2019). Two-photon polymerization (TPP) lithography, also called 3D direct laser printing (Lightman et al., 2017) and Direct Laser Writing (DLW) (Gissibl et al., 2016; Ligon et al., 2017), employs fs laser pulses and simultaneous absorption of photons to cure the material. In this method, the laser's focal point can be directed in all directions unlike the SLA and DLP technologies, in which the curing occurs layer by layer (Lee et al., 2007).

Fused deposition modeling (FDM) 3D printers melt a thermoplastic filament and extrude it through a nozzle on the build platform to shape a layer of the structure (Knowlton, Joshi, et al., 2017; SM Knowlton et al., 2015). FDM allows the usage of different filaments in a single process. For instance, the filament of the main structure can vary from the filament used for the fabrication of the supporting structures, making the post-processing of the product easier. After cooling down and solidification of the deposited layer, the next layer is fabricated by repeating the process, leading to the formation of the final product (Dhinakaran et al., 2020).

Co-axial extrusion is another 3D printing technology mainly used for bioprinting and fabrication of cell-laden structures. Although the process for this method is similar to extrusion-based printers, there are two material feeders for co-axial extrusion 3D printers, in which one of the materials is printed as a coating on the other one (Liu et al., 2018).

The principle of selective laser sintering (SLS) 3D printers is based on utilizing a laser beam, as a concentrated heating beam, to sinter tightly compact thermoplastic powder in a build tank. Sintering means the process of heating powder particles so that particles can stick together, without reaching the melting point of the powder, to form a solid structure (Mazzoli, 2013). After the sintering of each layer, the new powder is loaded into the build tank and the process is carried out repeatedly to shape the final structure (Lepowsky & Tasoglu, 2018). Selective laser melting (SLM) uses a similar 3D printing technique to SLS, whereas SLM needs support structures, and metal powder is usually used. By reiterating laser and dot matrix data patterns, each layer solidifies, leading to the final product. Electron beam melting (EBM) is also used for 3D printing of metallic materials with a similar method to laser melting, except that the beams of electrons perform the melting instead of laser light (Amin, Knowlton, Hart, et al., 2016).

Material jetting is another 3D printing method which shapes the object and supporting structures by jetting the material onto the build platform, in a layer-by-layer process, using inkjet print heads to shape the product. Photopolymer jetting is also an analogous process in which the layers of liquid photopolymer are jetted onto the build platform, followed by a UV light curation. Similar to material jetting, inkjet print heads are used in the binder jetting technique. However, in this method, a liquid adhesive is jetted onto the layers of powder in the build tank. By feeding new powder, the next layers are created successively, leading to the final product. Unlike material jetting, no support structures are needed for the fabrication of complex designs by binder jetting (Amin, Knowlton, Hart, et al., 2016). Table 1 illustrates the advantages and disadvantages of each technology and the printing resolution each method offers.

There are various tradeoffs and limitations of 3D printing techniques, that have to be considered in the design iteration and prototyping stage of MN fabrication. To avoid fracture and perilous leftovers in the skin during insertion, physiologically relevant mechanical properties such as the compliance of elastic moduli between skin and MN are desired. Powder-bed based methods (e.g., SLS and SLM) offer fine mechanical properties since metallic alloys (e.g., stainless steel, nickel, aluminum, and titanium) can be used. However, the biocompatibility of metal alloys or their compliance with biocompatible coatings should be

considered before proceeding with the fabrication method. Moreover, MNs fabricated by powder-based methods possess undesired rough surfaces. Additionally, the high temperature of the sintering process confines the use of biological material (e.g., cells). Overall, considering the smallest attainable size features, powder-bed based methods are not practical for the production of MNs. Extrusion-based methods (e.g., FDM) are simple, cost-effective techniques, which can operate with biocompatible materials. However, the final resolution of this approach is lower than that of vat polymerization methods. Furthermore, low mechanical properties, layer-by-layer finish of the surface, and high temperature utilized in the process pose challenges against the implementation of extrusion methods for MN fabrication. Vat polymerization techniques have attracted more attention for the fabrication of MNs compared to other 3D printing methods. All vat polymerization methods offer a relatively high resolution (Table 1). The selection of the fabrication method should be based on the proposed application. For instance, MPP has the highest resolution, whereas the process is quite slow and supports limited materials. Therefore, MPP may be considered as a suitable method for prototyping and research applications rather than mass production. Likewise, DLP is a faster method, which is less affected by oxygen inhibition compared to SLA, while SLA has a higher resolution.

2.1.3 3D Printing Technologies in Fabrication of MNs

SLA, DLP, MPP methods, and photopolymer jetting are of high interest for the fabrication of MNs due to the higher resolution and wide material choice offered by these methods. SLA, for instance, was used for the fabrication of poly(propylene fumarate) (PPF) MNs in a dynamic mask projection microstereolithography (μSLA) setup. The fabricated MNs had 1000 μm height, 200 μm base diameter, and 20 μm apex diameter (Lu et al., 2015). Also, the SLA 3D printer, with a z-axis resolution of 25 μm and x-axis resolution of 140 μm, was employed to fabricate biocompatible polymeric MNs and then insulin solutions were deposited on the needles using inkjet printing (Pere et al., 2018). In another case, SLA 3D printing was used for the fabrication of 1000 μm height cross-shaped polymeric MNs, followed by coating chemotherapy medication (cisplatin) formulations on the needles, via inkjet printing, for skin cancer treatment (Uddin et al., 2020). DLP was utilized to produce MNAs on personalized curved surfaces using castable resin, post cured to cure any remaining uncured resin for 2 h. Using this 3D printing method, with XY resolution as well as a printing layer height of 50 μm, 300 μm base diameter, and 900 μm height were obtained for MNAs (Lim et al., 2017). TPP lithography was utilized to produce cylindrical, pyramidal, and conical biocompatible magnetic MNs, using drop cast IP-DIP resist, on a single-side polished silicon wafer. MNs fabricated by TPP had a base diameter of 630 nm, aspect ratio of 1:10, pitch of 12 μm, and coated by a 120 nm thickness iron coating (Kavaldzhiev et al., 2017). Also, TPP lithography 3D printing was employed to fabricate MNs, with IP-S (Nanoscribe GmbH) photoresist, for performing perforations on the scale of millimeters. MNs had a shaft diameter of 100 μm, a height of 350 μm, and a taper angle of 60° (Chiang et al., 2020). In another study, the TPP 3D printing method enabled the fabrication of hollow MNs using IP-S photoresist, with an outer tip diameter of 50 μm, an inner diameter of 30 μm, tapered angle of 5°, and height of 200 μm (Moussi et al., 2020). In another study, an extrusion-based 3D printer with 2 nozzles was used to produce patches of MNs for drug delivery (Wu et al., 2020). One of the nozzles of the printer is used to extrude substrate material, where the other nozzle prints the material contains the

drug to form the cylindrical shape of the MNs. The achieved resolutions reported in this study were 601 µm for base diameter, 24 µm for tip diameter, and 643 µm for height.

Additive manufacturing can be used to fabricate MNs by directly 3D printing MNs or by producing female master molds. Mold-based techniques are suitable for the mass production of MNs with a diversity of materials such as biocompatible hydrogels (Tejavibulya et al., 2019). Nonetheless, to make any changes in the dimensions of MNs, the entire process of design and fabrication of mold should be repeated. An SLA-based two-step "print and fill" method was developed (Kevin J. Krieger et al., 2019) for fabricating customizable replica molds (**Figure 2.2**). Firstly, the MNA master was printed using an SLA 3D printer. Subsequently, a

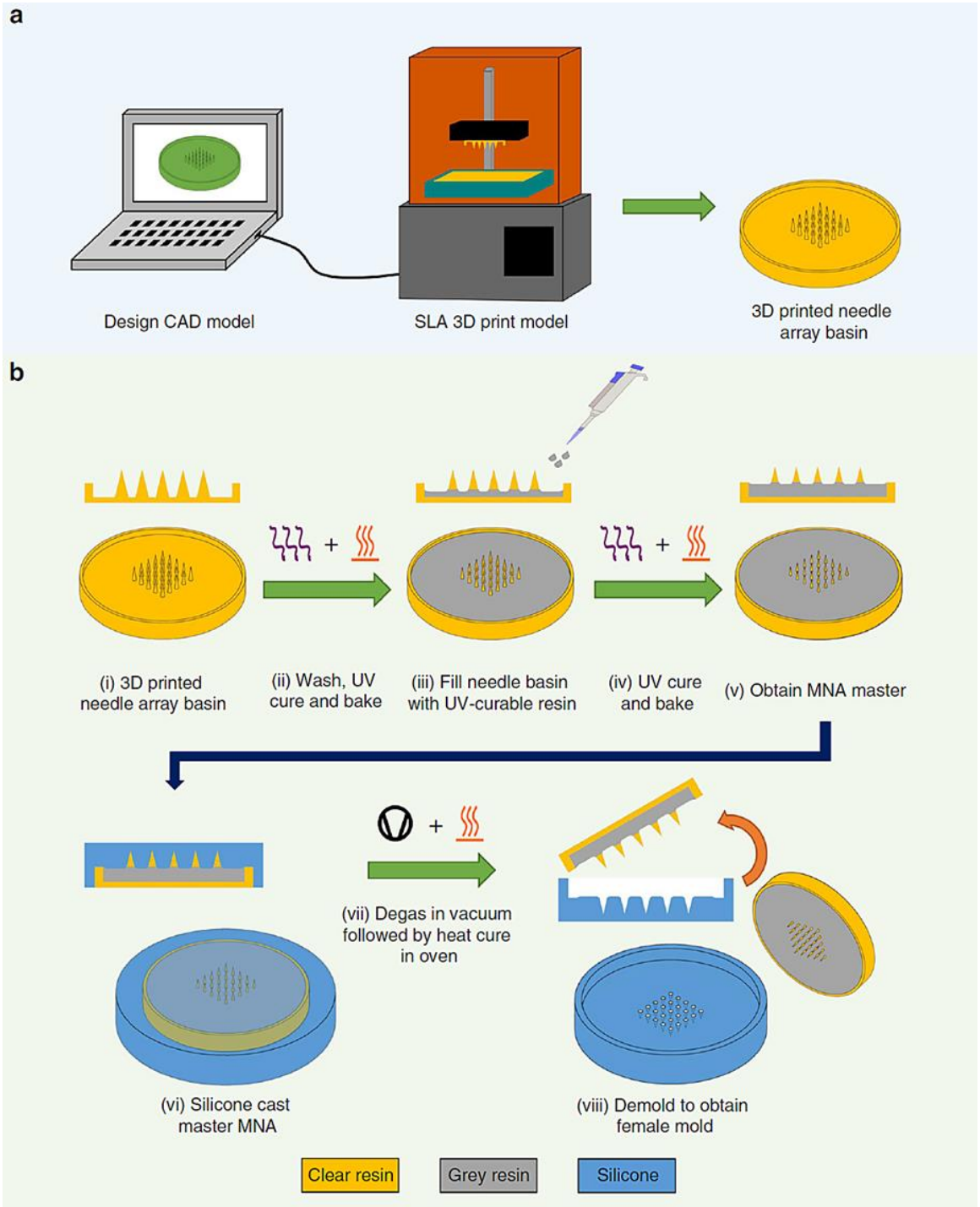

Fig 2.2. Step by step illustration of fabricating microneedles (MNs) with stereolithography (SLA) 3D printing and replica mold method. (a) The design procedure was followed by 3D printing of the designed structure using an SLA printer. (b) The 3D printed MNs were washed and then cured with ultraviolet (UV) light, followed by filling the basin with UV-curable resin to obtain the desired MN height, resulting in a microneedle arrays (MNA) master. In the next step, using silicone, degassing by the vacuum chamber, and heat curing in the oven, the final female master mold can be produced. Adapted with permission from (Kevin J. Krieger et al., 2019). Copyright 2019, Springer Nature.

UV-curable resin was used to obtain the desired MN length. Finally, a silicon female master mold was produced using the 3D printed MNA master (Kevin J. Krieger et al., 2019). UV curable resin was used to produce MNs with different aspect ratios (3:1, 4:1, and 5:1) and layer heights (25, 50, 100 μm) to determine the discrepancy between the desired and resulted height, needle's tip angle, and tip ratios (**Figure 2.3**). Despite changing design features, the tip radii of MNs were at the range of 20-40 μm. Furthermore, higher printing layer heights results in faster printing, while yielding lower surface quality (Kevin J. Krieger et al., 2019; Yao et al., 2020). Two-photon polymerization with a 780 nm light wavelength was used to produce soft elastomeric MN replica molds. Using these molds, MNs with 700 μm height and 150 μm shaft diameter were fabricated (Rad et al., 2017). 3D

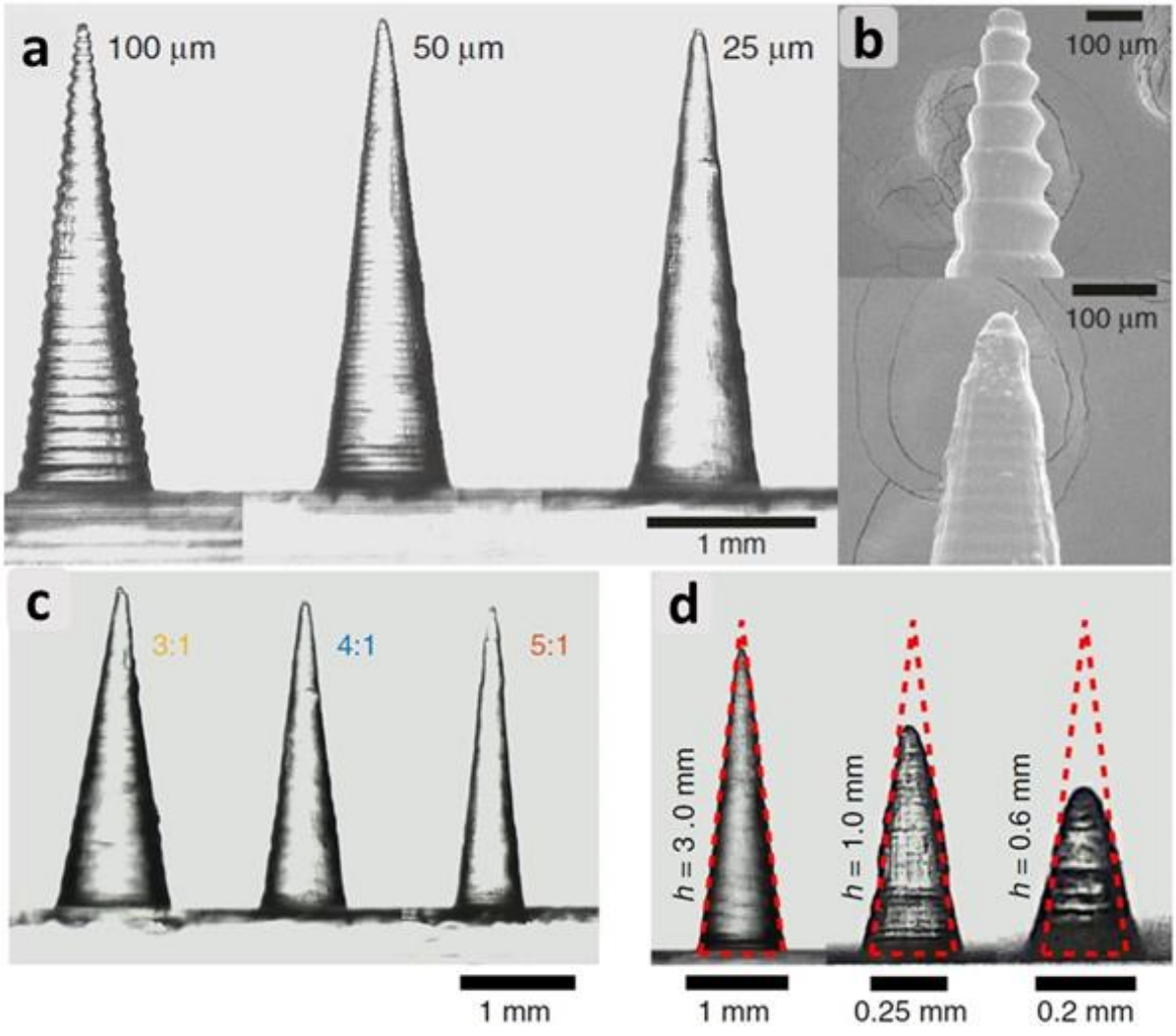

Fig 2.3. Scanning electron microscope (SEM) images of microneedles (MNs), fabricated by stereolithography (SLA), with different feature sizes. (a) Fabricated MNs via various printing layer heights,100, 50, and 25 micrometers. Although lower layer heights bring about better surface quality, the printing process will be slower. Hence, choosing the proper layer height is a trade-off between surface quality and time. (b) Tip of fabricated MNs (top:100 µm, bottom: 25 µm layer height). (c) Different aspect ratios. A higher aspect ratio here means a gradual increase of shaft thickness which results in a painless insertion of MN. However, thinner needles possess low mechanical strength which can result in breaking the needle in the insertion process. (d) The discrepancy between the input and output height. Higher aspect ratios suffer more from discrepancy issues. Adapted with permission from (Kevin J. Krieger et al., 2019). Copyright 2019, Springer Nature.

direct laser printing along with micro molding was employed to fabricate undercut MNs (Balmert et al., 2020). The 3D printed master MNA was used to generate replicas that were organized on a 3D printed photosensitive resin holder. Using this holder, a production mold was fabricated with polydimethylsiloxane, which enabled the fabrication of multiple MNAs at once (**Figure 2.4**). While micro molding is a suitable method for large-scale production, disassembling MN with an undercut is complex and susceptible to failure. Using micro molding and flexible production molds not only addressed the disassembling problem, but also the production molds can be used several times, which reduced the fabrication cost of MNAs (Balmert et al., 2020). In another study, drawing lithography was used to fabricate MN molds using UV-curable resin (Lin et al., 2016). This method

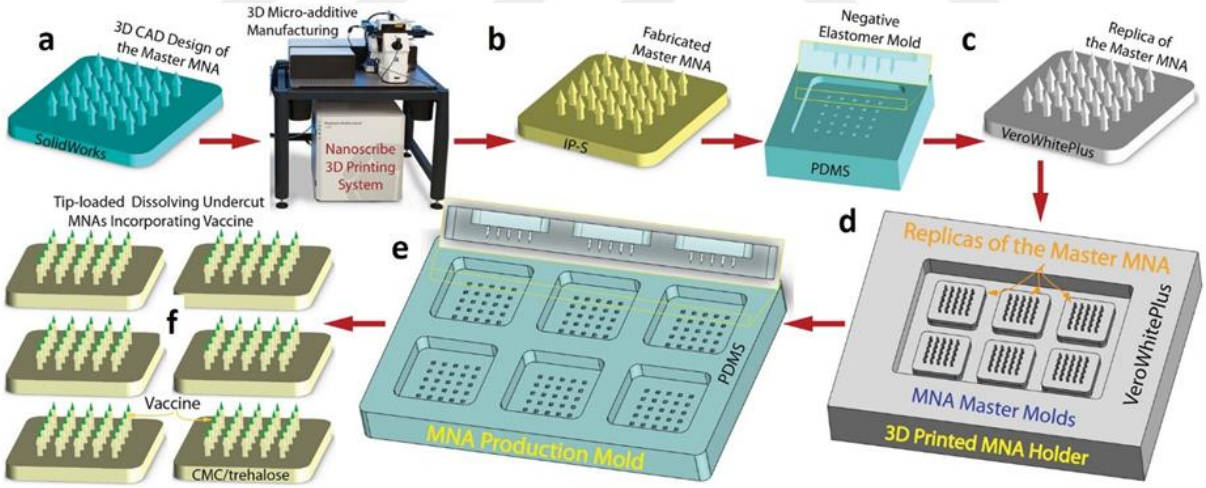

Fig 2.4. Scalable MNA fabrication in 6 steps, using 3D direct laser printing and molding. (a) 3D design of size features of the MNA, based on the proposed application. (b) Direct production of designed MNA using 3D direct laser printing. MNs with a height of 750 µm, base diameter of 150 µm, arrow base radius of 250 µm, and a tip angle of 30 degrees were produced. (c) Replicating the master MNA mold with high fidelity by a two-step micro molding process. (d) Arranging multiple MNA master molds on a 3D printed holder. (e) Production of MNA fabrication molds by polydimethylsiloxane (PDMS). (f) Loading the desired drug on the tip of the fabricated MNAs by a spin-casting method. Adapted with permission from (Balmert et al., 2020). Copyright 2020, Elsevier.

is faster and less costly compared to photolithography and etching techniques. However, the main drawbacks of drawing lithography approach are low control over the geometry of MNs, and incapability to produce different MN profiles (e.g., cylindrical and pyramidical) (Lin et al., 2016).

One of the impediments of achieving desired geometrical factors is the restricted resolution of the employed fabrication method. While several studies have been conducted to enhance the resolution of 3D printers by modifying the printer itself (Gong et al., 2020; Johnson & Procopio, 2019; Serex et al., 2018), integrating 3D printing with other techniques can enhance the resolution of the final MN without manipulating the printer. To overcome the resolution limit of 3D printers, the SLA 3D printing technique was integrated with shrinkable hydrogels (Ochoa et al., 2015). MNs with tips down to 9.6 μm radius of curvature were fabricated. The resolution of MNs produced with this method was higher than MNs printed with the same 3D printer without utilizing shrinkable hydrogel.

3D printing with programmed shape deformation, also known as 4D printing, is one of the approaches to produce bioinspired MNs with curved barbs (Han et al., 2020), increasing the adhesion of MNs to the tissue by 18 times (Morde, 2018). Using μSLA, MNs with a base diameter of 400 μm, length of 4 mm, and cone tip angle of 10° was fabricated. The barbs possess a 200 μm base diameter with 450 μm length. Sudan I as a photoabsorber (PA), poly(ethylene glycol) diacrylate, phenylbis (2,4,6-trimethylbenzoyl) phosphine oxide as a photoinitiator (PI), and Mn ≈ 250 (PEGDA 250) as a monomer were used to produce MNs with curved barbs (Han et al., 2020). One of the issues which adversely affects the surface quality of 3D printed MNs is the layer-by-layer nature of the 3D printing process. To solve this limitation, Continuous Liquid Interface Production (CLIP), a single step, based on vat polymerization, continuous AM method was devised to prototype MNs rapidly (Caudill et al., 2018; Johnson et al., 2016). Using polyacrylic acid, trimethylolpropane triacrylate, and photopolymerizable derivatives of polyethylene glycol as well as polycaprolactone, MNs with 1000 μm height, 333 μm base width, and 2.3 μm tip radius were produced by CLIP (Johnson et al., 2016). Furthermore, magnetorheological drawing lithography (MRDL) AM method, which needs no masks and molds, has been introduced (Chen et al., 2018; Zhipeng Chen et al., 2019) for fabricating flexible MNAs (Ren et al., 2017). To achieve cost-effective rapid mass production, droplets of the polymerized mix of epoxy novolac resin with iron microparticles on a polyimide substrate were drawn, assisted by a magnetic field, to form liquid MNAs, which were solidified by applying hot air and vacuuming. MNs with a height of 600 μm and a tip radius of 12 μm were produced with this method. Finally, a coating of the Ti-Au film was applied to the MNAs to ensure compatibility and conductivity (**Figure 2.5**).

There have been attempts to fabricated even smaller needles. Nanoneedles (NNs) have been fabricated by optical vortex pulses, confined laser spinning (CLS), and metal-assisted chemical etching. Each of these fabrication methods offers pros and cons. Etching, for instance, is not a suitable method for producing NNs made of hard metals (e.g., gold, silver). In this regard, femtosecond DLW was used to produce different sizes of NNs by controlling laser pulse energy with a combination of half-wave plates and Brewster polarizer (Yendeti & Soma, 2020). Since no chemicals were involved in the fabrication process, this approach was considered an environmentally friendly method. Microscope objectives (20× and 60× lenses) were examined to focus laser pulses which resulted in producing NNs

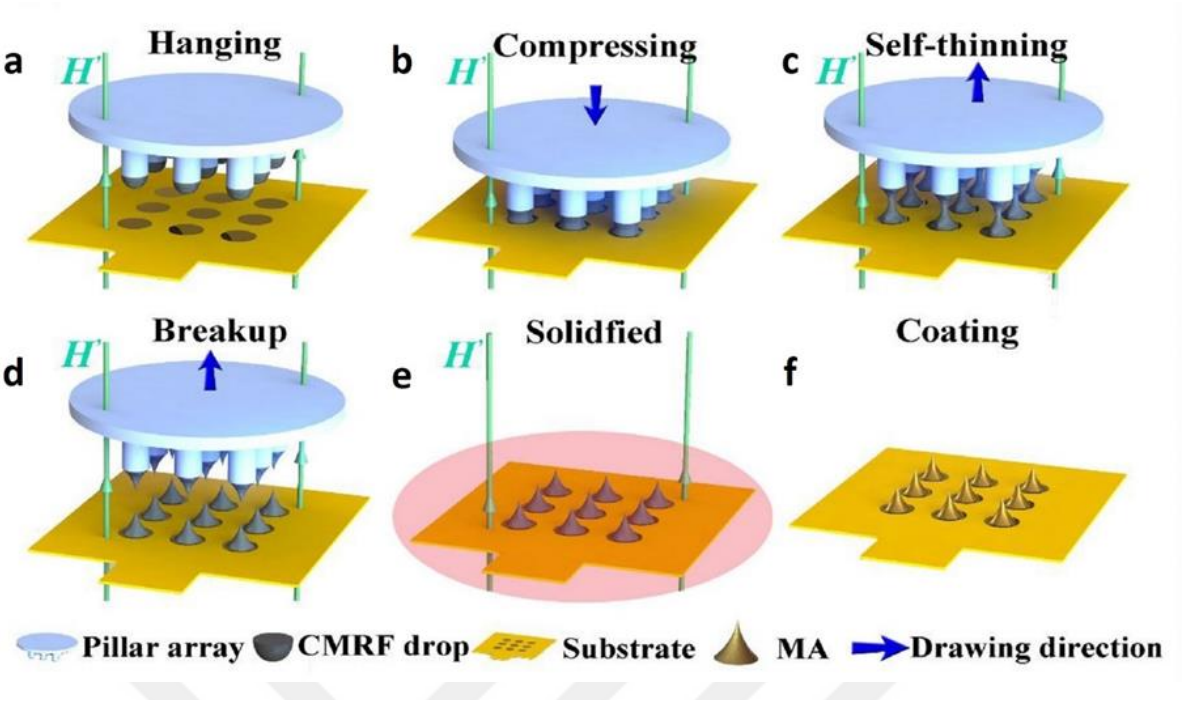

Fig 2.5. Sequential steps of microneedles (MNs) fabrication by magneto-rheological drawing lithography (MRDL), an additive manufacturing method. (a) Pillar tips, with a diameter of 700 μm, were coated by dipping in curable magnetorheological fluid (CMRF). (b) Then, the pillars were moved downward, toward a substrate, with a constant speed of 1.5 mm/s to press droplets to the substrate for 1 s. (c) Pillars moved upward with the speed of 1.5 mm/s, and stopped in 12 mm from the substrate, resulting in a necking effect. (d, e) When the thinned CMRF lines broke up at room temperature, the MNs were solidified at 100 °C for 1 h. (f) Subsequently, the fabricated MNs were coated by titanium (Ti) and gold (Au) using a magnetron sputtering machine. Adapted with permission from (Ren et al., 2017). Copyright 2017, Elsevier.

with higher packing densities using 60× lenses. However, NNs fabricated by 60× lens had poor bonding with glass coverslip compared to that of the 20× lens. In an LDW process to fabricate NNs, carried out by evaporating metal, the laser focuses on a certain spot where the center of the laser beam which has higher intensity (Gaussian distribution) increases the temperature above the evaporation temperature of the metal. On the other hand, the edges of the laser beam with lower intensity raises the temperature above the melting temperature and below the evaporation temperature of the material. Thus, when the evaporated metal at the center wants to expand and escape with high pressure, it expels the melted metal at the edges and forms NNs.

2.2. Emerging Applications in Biomedical Engineering

2.2.1 Drug Delivery

MN patches have applications in immunology, cosmetics, diagnostics (Yang et al., 2019), and continuous and constant release of therapeutic agents through the skin after topical treatment (Kim et al., 2019). Generally, there are a few facile tailored systems to deliver specific molecules into the body. The presence of immunologically active cells, namely antigen-presenting cells (APCs), allows the

skin to be an active immune organ. Hence, delivering drugs through the skin is more efficient and durable than intramuscular delivery owing to the presence of fewer immuno-cells in muscles than skin (Lambert & Laurent, 2008). However, delivering drugs through the skin has not been developed to its full potential due to the shortage of minimally-invasive, efficacious, user-friendly, and ubiquitous technologies (Kabashima et al., 2019). Drug delivery through the skin can obviate the need for conventional intramuscular injections. The disadvantages of conventional needles are fear of needles (trypanophobia), complex transport and storing requirements, contamination, the possibility of disease transmission, demanding trained personnel to perform vaccination, chance of injuries, and pain brought about by needles (Norman et al., 2014; Prausnitz, 2004; Prausnitz & Langer, 2008). MN patches deliver target biomolecules to the local area under the administration site or send bioactive compounds to the remote sites through the circulatory system. In clinical settings, the local delivery of certain chemicals, factors, and drugs could be achieved via intradermal, subcutaneous, and intramuscular approaches (Yang et al., 2019). The direct injection of target molecules to the muscles and subcutaneous tissue facilitates the passive diffusion of the drug to the systemic blood system. A major challenge in the application of MNs is to release the target molecules via the cutaneous barrier (Indermun et al., 2014). In the delivery of target molecules, the cutaneous tissue is temporarily disrupted after piercing the stratum corneum to bypass the hydrophobic layer and beneath viable keratinocytes. In most cases, target molecules placed in the epidermis or upper dermis reach systemic circulation through passive diffusion. Therefore, MN patches are candidates for painless and self-administrated hypodermal and dermal injection (Baek et al., 2017).

Polymer MNs were developed by μSLA 3D printing with programmed deformation (4D printing) to study their adhesive properties in the cutaneous system for application in biosensors and long-term monitoring and delivery systems (Han et al., 2020). The fabricated MNs included curved barbs to improve adhesion capacity. By tuning the curving thickness, angle, and material composition, the adhesion of MNs with barbs to the tissue was increased by 18 times compared to a needle without barbs (Morde, 2018). The fabricated MNAs were tested to deliver a drug in an *ex vivo* chicken tissue (Han et al., 2020).

MNs were integrated with microfluidic channels including multiple inlets (Yeung et al., 2019). Using a biocompatible and transparent resin based on methacrylic acid esters as the building material, SLA 3D printing allowed rapid cost-efficient fabrication of 12 devices in 2.5 h. The integrated microfluidic chamber was designed as a hydrodynamic mixer of fluids which enabled transdermal drug delivery. Different parameters and geometries were tuned to achieve an optimized performance, including a high aspect ratio needle tip. The optimal radii of curvature of MNs were as low as 25 μm, in +45° printing orientation, with a base width of 800 μm and a central bore of 600 μm. The device was tested in an *ex vivo* porcine skin (**Figure 2.6**). SLA 3D printing has been also utilized to fabricate MNAs with a biocompatible photopolymer, Class I resin, Dental SG, by Formlabs, coated by insulin and drug carriers on the needles using inkjet printing (Economidou et al., 2019). The 3D printer has a resolution of 25 μm on the z-axis, and 140 μm on the x-axis, resulting MNs with a height of 1 mm and tip size of 100 μm. The fabricated MNA was tested on *in vitro* porcine cutaneous tissue. The needle was designed in two shapes of a pyramid (1×1×1 mm) and a spear (0.08×1×1 mm), in which the geometry of the pyramid needed a lower force to

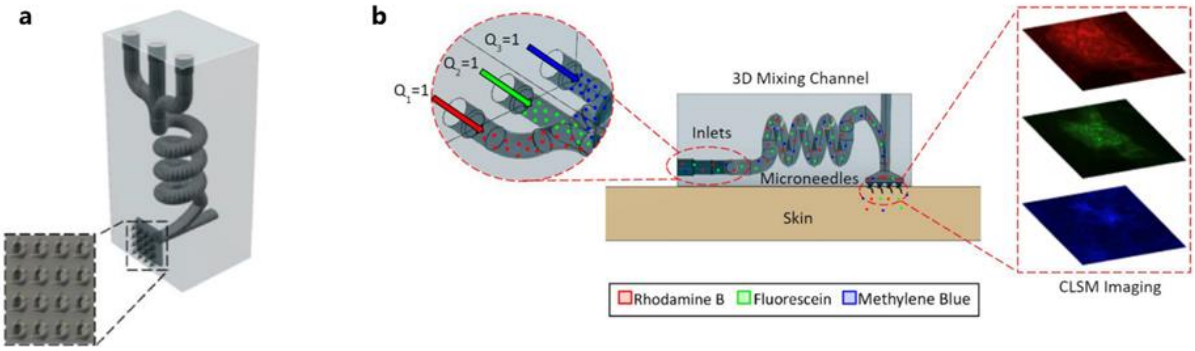

Fig 2.6. The integration of microfluidic devices with microneedles offers better fluid management abilities, resulting in a more advanced level of controlled drug delivery. (a) An illustration of the proposed device fabricated by stereolithography 3D printing, with 3 separate microfluidic inlets and microneedles (MN) as the outlet. The zoomed section shows the MNs. (b) *Ex vivo* transdermal delivery of three model drugs, from multiple inlets, into a porcine skin. Adapted with permission from (Yeung et al., 2019). Copyright 2019, American Institute of Physics.

penetrate the skin and reach deeper layers. Xylitol had the optimum performance as the drug carrier in the system. *In vivo* testing in a diabetic mouse model showed that insulin lowered the glucose level in the blood within 60 min. In another study, the same method, material, and coating technique was used to fabricate cone shape MNs to study the effect of MN shape on delivery time as well as the required force for insertion (Pere et al., 2018). The device was tested *in vitro* porcine skin, in which insulin was released within 30 min. Among the drug carriers used, xylitol showed the optimal result. Although the needle design did not affect the delivery time, the cone shape needed lower applied force for penetrating the skin as compared to the pyramid pattern. In another case, the SLA 3D printing technology was used in the fabrication of MNAs with a polymer resin (Xenikakis et al., 2019). The printed needle height was shorter than the CAD model because of the solidification shrinkage. The tip radius was set to the best resolution of the SLA printer, 50 μm. Although MN heights of 1090, 875, 470 μm were printed, only the 875 μm MN was suitable for clinical tests, since 1090 μm MN can cause pain by reaching the nerve system while 470 μm was not efficient due to its short length. Mechanical property analysis indicated reasonable strength in the fabricated MNAs against fracture in high forces. Employing Finite Element Analysis, the force required for the needle to penetrate the skin was calculated. This estimation met the experimental amount when the fabricated MNAs were tested on human skin *in vitro*. Transdermal delivery and permeation of two model dyes were also tested, demonstrating satisfactory penetration and higher cumulative amount in both cases after treating with the MNs.

Using 3D laser lithography, (also known as DLW), and micromolding, a scalable manufacturing method, was developed for the fabrication of soluble undercut MNAs for drug delivery (Balmert et al., 2020). The MNs were fabricated by CMC/trehalose hydrogel, prepared by dissolving a mixture of sodium carboxymethylcellulose (CMC) and D-(+)-trehalose dihydrate, at a total solute concentration of 30% w/w in endotoxin-free water. Soluble MNAs were rigid enough to endure the penetration process in a dry state. Right after insertion, MNs dissolve into the skin rapidly. Undercutting MNAs allows retention of the MNs in

the skin as well as in the non-cutaneous tissues. This device may be utilized for either intradermal or non-cutaneous drug delivery (e.g., cardiac and liver tissues). To evaluate the performance of a dissolving MNA, penetration, solubility, and efficiency of delivery should be considered. 10 min of MN insertion into living human skin explant resulted in 80% drug delivery, where increasing insertion duration to 20 min did not substantially amplify the delivery rate. MNs had a height of 750 μm, an apex angle of 30°, stem width of 150 μm, and arrow base width of 250 μm.

TPP 3D printing technique, with 780 nm wavelength, was used to fabricate high-quality master templates of MN arrays using polylactic acid (PLA) and silicone elastomer mix. Two types of MNs were developed in this study; first, dissolving MNs (DMNs) which were efficacious in the delivery of both hydrophilic and hydrophobic drugs; second, hydrogel forming MNs (HFMNs) which were useful in interstitial fluid extraction from the body and delivery of drug molecules. Different designs (e.g., conical, and pyramidal MNs), needle sizes, the spacing between needles, and needle density were examined to find the optimum features to achieve the most optimum mechanical properties as well as drug delivery efficiency. Longer MNs possess a more efficient drug deposition rate, due to the deeper penetration into skin, with lower mechanical strength. Additionally, by increasing the interspacing of MNs, although, because of the reduced number of MNs per array, the overall amount of delivered drug decreases, the drug delivery efficiency improves (Cordeiro, Tekko, Jomaa, Vora, McAlister, Volpe-Zanutto, Nethery, Baine, Mitchell, & McNeill, 2020). Besides the delivery of the substances to the treatment area, it is important to penetrate MN without damaging the surroundings in the sensitive organs. One of the challenging examples is the safe and precise delivery of therapeutics to the inner area of the ear to treat hearing diseases. MNs have been employed to delicately perforate the round window membrane, one of the two openings from the middle ear to the inner ear (Aksit et al., 2018). Using TPP lithography 3D printing, MNs with a tip radius of 500 nm, a height of 200 μm, and a shank radius of 50 μm were fabricated using IP-S photoresist. The MN was used to perforate the round window membrane of a guinea pig ear *in vitro*. Although the membrane was not torn, a separation in the fibers of the membrane was reported because of the fiber-to-fiber decohesion.

One of the challenges of vaccination is the need for the repetition of vaccination with a specific time interval, which imposes further expenses and agitates patients. One-off administration systems are a preferable replacement for applications that requires multiple injections, such as cancer therapeutics or growth hormones (Tran et al., 2020). MNs, with a core-shell structure, were fabricated using TPP (for silicon wafer patterning) and photolithography (for the fabrication of molds for the MN caps and the supporting array), followed by a 3D manufacturing process to assemble the shell and the cap of the MN along with a drug core (**Figure 2.7**), enabling programmable drug-releasing kinetics with time intervals (Tran et al., 2020). Each MN had a height of 600 μm, a core height of 400 μm, a base diameter of 300 μm, and a core diameter of 200 μm. Modifying the degradation of the shell, which was made of poly(D,L-lactide-*co*-glycolide) (PLGA), a biodegradable polymer, provided the ability to control the release time of the drug. Using this approach, with only one-time insertion, vaccine antigens can be controllably released over defined periods of time, which was tested for Prevnar-13 vaccine on rats (Tran et al., 2020).

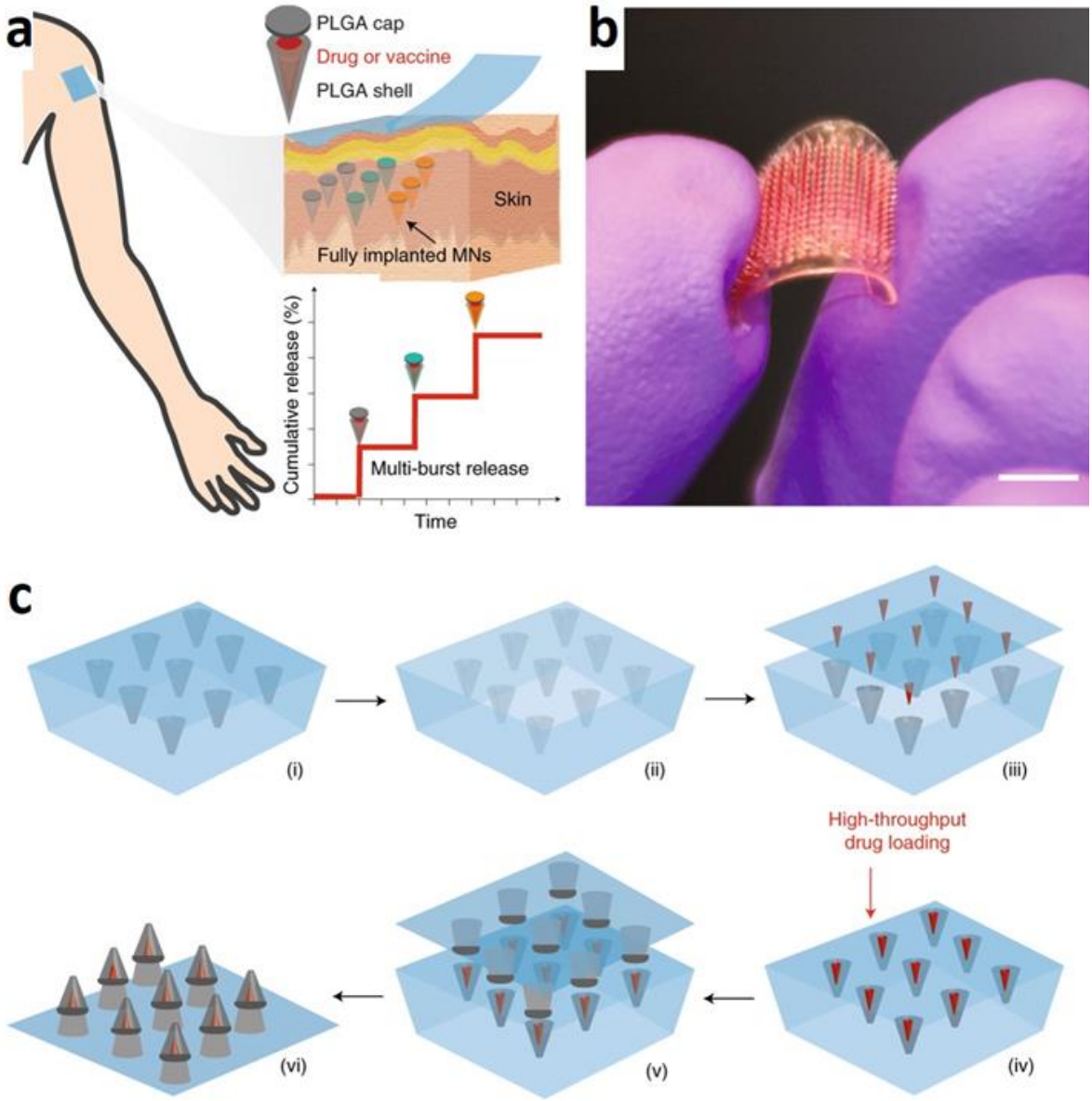

Fig 2.7. MNs with a core-shell structure featuring programmable drug-releasing kinetics with a one-time insertion mimicking the multi-injection drug or vaccine delivery systems. (a) Schematic view of the three constituent elements of the fabricated MNs: shell, cap, and drug core, demonstrating the underlying principle of the kinetics of controlled drug delivery. (b) Optical image of the fabricated MNs. Scale bar = 0.5 cm. (c) Step-by-step 3D manufacturing process of MNs: (i) a PDMS negative mold of MNs was filled with PLGA. (ii) a positive polylactide (PLA) mold was used to encroach the MNs inside the PDMS mold. (iii and iv) arrays of drug cores were aligned and loaded into MNs in a high-throughput drug-loading process. (v) PLA supporting patch including the cap layer was attached to the MNs in a heat-sintering process. (vi) The MNs were ready after peeling off the PDMS mold. Adapted with permission from (Tran et al., 2020). Copyright 2020, Springer Nature.

An extrusion-based 3D printer with 2 nozzles was used to produce patches of MNs with 643 μm height and 24 μm tip diameter for insulin delivery (Wu et al.,

2020). Following the insertion of insulin loaded MNs to the skin of mice with type 1 diabetes, after ~1 h, the blood glucose concentration decreased to the normoglycemic range, with no report of hypoglycemia during drug delivery. Moreover, the blood glucose concentration remained in the normoglycemic range up to 40 h after insertion, demonstrating the adequate drug delivery performance of the proposed MNs.

The treatment of cancers imposes substantial financial burdens on health systems worldwide (Semin et al., 2020). In cancer biology and therapy, most of the published data have focused on the stimulation of innate and adaptive immune cells by the introduction of specific antigens, genetic elements, and adjuvants or direct delivery of anticancer agents (either alone or in combination with nanoparticles) (**Figure 2.8**) (Wang et al., 2016), and the use of conventional and novel approaches to deliver chemotherapeutic agents exhibited sub-optimal results in animal models or clinical settings (Jacinto et al., 2020). MN patches have applications in drug delivery in cancers and metabolic disorder diagnosis (Yang et al., 2019) by opening new avenues to support fast-acting sophisticated drug delivery with specified doses in a controlled manner (Queiroz et al., 2020). Moreover, efficient delivery of chemotherapeutic agents to the cancer growth sites while diminishing leakage to the systemic circulation as well as neighboring tissues, and minimizing adverse side effects are of great importance (Mojeiko et al., 2019). In this regard, MN patch technology can allow the treatment of metabolic diseases by enabling patients to painlessly self-administer injections (**Figure 2.8**) (Yang et al., 2019). Hence, the integration of advantages of 3D printing with the potency of MNs for controlled cancer drug delivery can increase the effectiveness of cancer diagnosis methods.

2.2.2 Sample Extraction

Other applications of MNAs are in extracting and obtaining samples from patients for bioassays and monitoring setups (Zhu, Zhou, Libanori, & Sun, 2020). Self-monitoring of blood glucose (SMBG) is a simple way to control blood glucose by the patients to prevent adverse ramifications of prolonged hyperglycemia. However, the extraction of blood with conventional needles is painful, which causes reluctance in patients to collect blood samples regularly. MNAs as a minimally invasive and painless method can facilitate the development of point-of-care (POC) blood collection (Farhan et al., 2017; Vincze et al., 2004).

A hollow MNA was developed along with a paper-based colorimetric detection method to detect glucose concentrations ranging from 4 to 7 mM L-1 by eye (Nicholas et al., 2018b). Using SLA 3D printing, an initial master mold was prepared to build a negative mold, which was used to fabricate 400 μm long hollow MNA. This device could absorb samples in 5 s for POC applications. MNs should be able to withstand 0.028 to 0.030 N during insertion-axial load applied by the user to penetrate into the skin (Olatunji et al., 2013). Therefore, the mechanical properties of MNs should be studied to avoid fracture. The strength of the MNA was evaluated using a 50 N load cell which pushed toward the MN at a rate of 0.01 mm s-1. The reported MN was stiff enough for application in POC diagnostics (Nicholas et al., 2018b).

Based on the DLP 3D printing technology, a new setup was built with high precision to print in micro-scale, being utilized for fabrication of MNs with a

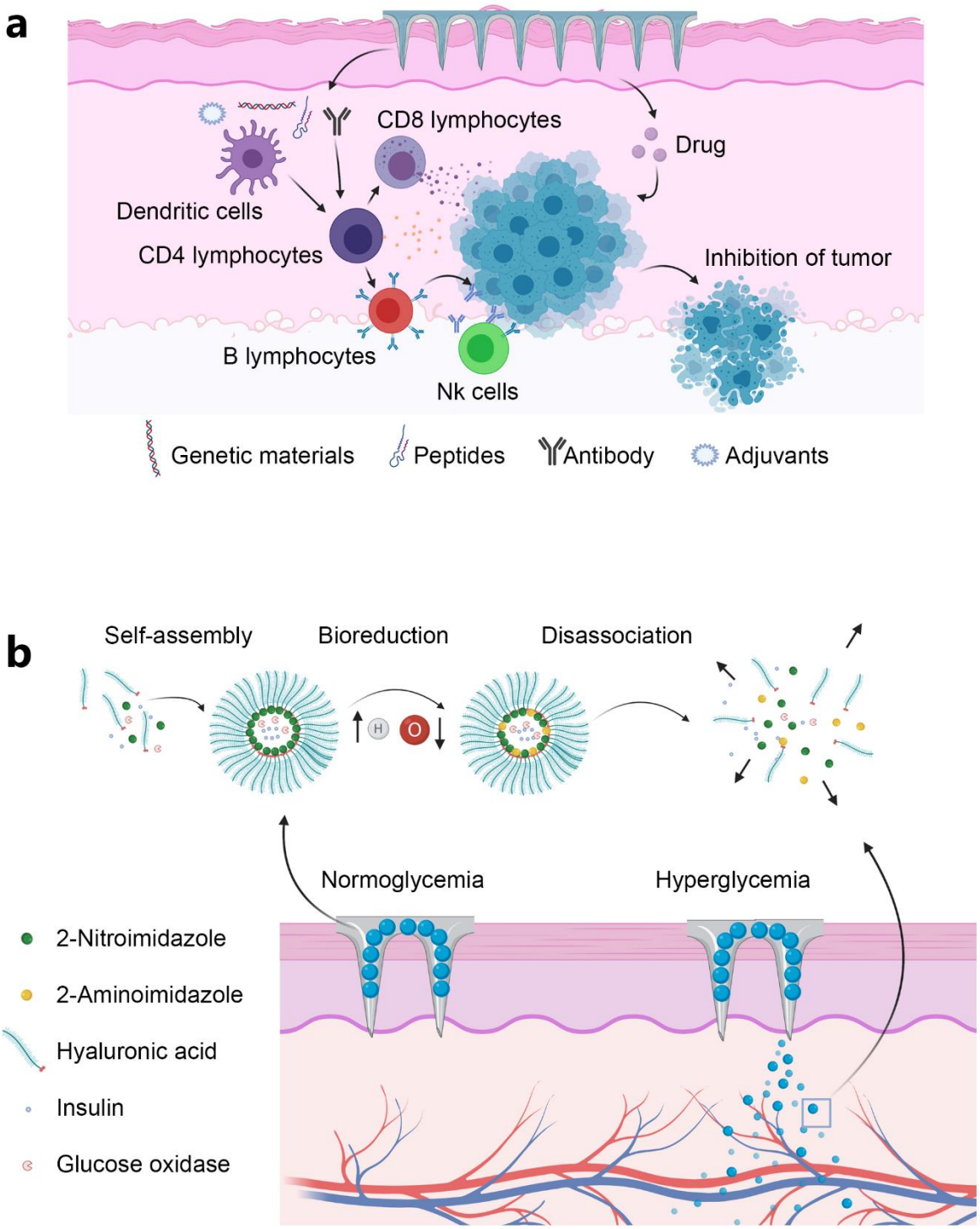

Fig 2.8. Application of the microneedle (MN) patches in cancer therapy. (a) The integration of antibodies, adjuvants, peptides, and genetic elements is done to stimulate immune cells and to increase tumoricidal outcome along with chemotherapy. (b) Intelligent needle structures are used to control the systemic levels of endocrine hormones upon the onset of metabolic diseases.

photosensitive hydrogel which was cured with different blue light (Yao et al., 2020). Alginate hydrogel (5 wt%), which is similar to human skin in terms of mechanical properties, was used as an artificial skin to study drug injection, extraction, and detection by the fabricated MNs. MNs were soaked in deionized

(DI) water for 1 day, while the artificial skin was soaked in a RhB solution for the same duration, subsequently, MNs were inserted inside the skin. The integrated density of RhB inside the MNs reached more than 20 mg L^{-1} in 25 min, enabling the successful detection of drugs in the skin.

Using a 3D printed master mold, porous polydimethylsiloxane (PDMS) MNs with 1000 μm height were fabricated to extract PBS from an agarose gel-based skin phantom (Takeuchi et al., 2019b). In another study, drawing lithography, an additive manufacturing method, was used to fabricate a hollow metallic MN for blood sample extraction (Li et al., 2013). Following an examination of various size features and resist thicknesses, an 1800 μm height MN with a bevel angle of 15 °, an inner diameter of 60 μm, and an outer diameter of 120 μm was the most efficient MN for blood extraction (Li et al., 2013).

To study the extraction of interstitial fluid from the skin, MN holders were prepared, using photopolymer jetting 3D printing technology, with flat, concave, convex, and bevel profile geometries in order to test the influence of MN holder on fluid extraction efficiency (Taylor et al., 2020b). Ultra-fine needles were attached to these holders to form the MNAs. Since the MNs are susceptible to fracture during the insertion process, owing to their microscale thickness, the first benefit of using MN holders is protecting the MN, and thus, decreasing the chance of cracking MN during the injection by untrained patients, eliminating the need for the direct supervision of medical clinicians for insertion. Also, the holder applies pressure on the surroundings of the insertion site, enhancing the extraction rate in some cases. The concave geometry showed the best efficiency among the designed profiles with an extraction rate of 0.85 ± 0.64 $\mu L.min^{-1}$ when it was inserted as deep as 1.5 mm. Also, the length of the needles showed no major differences in the amount of extraction (Taylor et al., 2020b). In another similar study, ultra-fine needles, lubricated with a silicone lubricant to lessen the pain while insertion, were attached to photopolymer jetting 3D-printed holder arrays to shape the MNAs (Miller et al., 2018). The fabricated MNs were used to extract dermal interstitial fluid from humans and rats. Fluid amounts of up to 20 μL and 60 μL were extracted from human subjects and rats, respectively (**Figure 2.9**). The MN with a length of 1.5 mm had the best extraction success percentage, with 31%, compared to 1 mm and 2 mm MNs, with 14% and 16%, respectively.

2.2.3 Signal Acquisition

MNs have applications in bio-signal detection such as providing continual point-of-care tests. Early detection of diseases not only can alleviate the number of deaths or disabilities caused by cardiac or metabolic disorders, but also reduces healthcare costs for treatments of patients. Electrocardiography (ECG), electromyography (EMG), and electroencephalography (EEG) are vital bio-signals that could be monitored continually. Results acquired from these tests can help cardiovascular, muscular dystrophy, and epilepsy patients, respectively (Ren et al., 2017).

Multiple methods have been proposed for recording bio-signals. Wet electrodes as a conventional method require a time-consuming process of skin preparation and gel usage. Using gel hinders the long-term use of wet electrodes in point-of-care applications. Dry electrodes, on the other hand, as a possible solution for the drawbacks of wet electrodes, suffer from being on rigid substrates, which confine electrodes' flexibility and compatibility with skin. Moreover, large

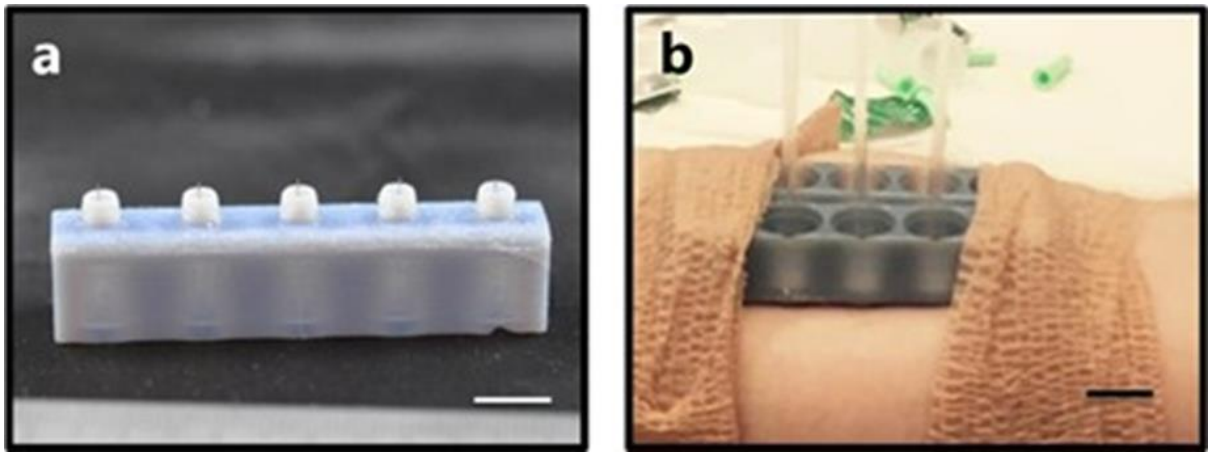

Fig 2.9. Microneedle arrays (MNAs) comprised of 3D-printed holder arrays and ultra-fine needles for dermal interstitial fluid extraction. (a) 3D printed MN holder with attached needles, coated with a silicone lubricant to lessen the insertion pain (Scale bar = 1 cm). MN holders not only do affect the extraction rate by applying pressure on the surroundings of the insertion site, but they also protect the fragile MN during the insertion process by an unskilled patient. (b) The fabricated MNA being used for dermal interstitial fluid extraction in a human subject. The extracted fluid was collected in the glass capillary tubes (Scale bar = 1 cm). Adapted with permission from (Miller et al., 2018). Copyright 2018, Springer Nature.

impedance values have been reported for dry flexible electrodes (Wang et al., 2017). The principle of conventional dry electrodes is based on capacitive detection, in which converter amplifiers inherently cause high impedances. This approach requires large equipment as well as auxiliary power sources that make this method a high-cost laboratory method. Understanding the principle of electrode-skin-electrode impedance (ESEI) can solve this limitation. Human skin is encompassed of two distinct layers, the outermost layer, stratum corneum that are dead cells, and stratum germinativum (SG) that are active cells. Conventional methods that use wet or dry electrodes on the skin are in touch with the outer layer of skin, SC. Therefore, this type of connection causes background noise and an imprecise signal to noise ratio. To surmount this problem, reducing SC thickness by shaving hair and removing the outmost layer of skin is suggested. These solutions will cause inconvenience for patients. Another possible solution is employing electrolytic gels to penetrate into the SC layer and reach SG to reduce the impedance. However, these gels may cause allergenic reactions and inconvenience to patients in long-term use. Using MNs, on the other hand, eliminates these predicaments (Yu et al., 2009). Since the thickness of the SC layer is 50-100 μm (Wang et al., 2017) and most of the contemporary MNs are longer than the thickness of SC, MNs can penetrate deep into the SG layer to measure signals directly, with minimum impedance. In addition, since MNs penetrate the SC layer, in which there are no blood vessels and nerve endings, patients feel no pain during the insertion process (Hegde et al., 2011). **Figure 2.10** depicts the signal measurement process and the electrical circuit simulation of conventional and MN-based methods (Ren et al., 2017; Yu et al., 2009).

The performance of these methods was compared under stable conditions. A flexible MNA electrode was fabricated to have 36 needles (36-FMAE) by MRDL method, on a flexible substrate as a wearable sensor. To ensure the conductivity

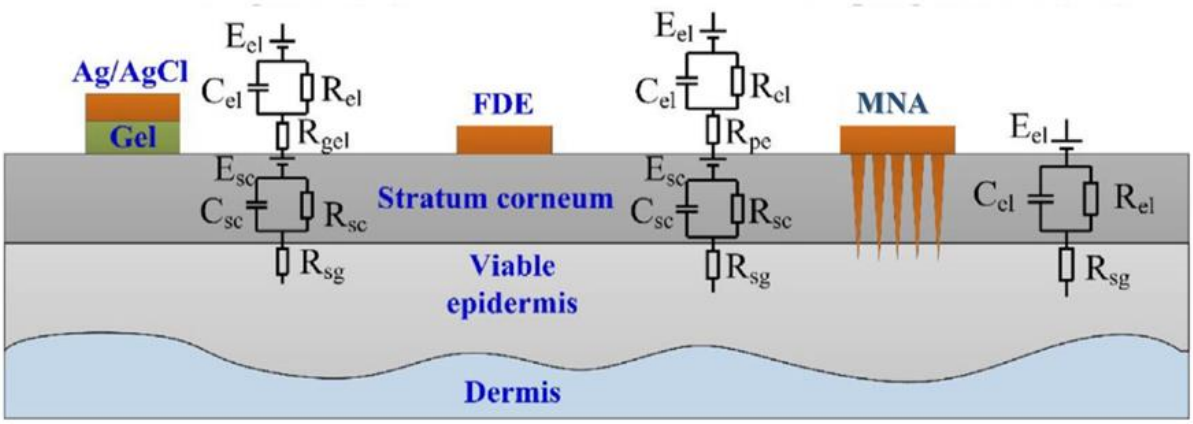

Fig 2.10. Different layers constituting the skin, and circuit model corresponding to different bio-signal recording techniques. While utilizing conventional wet electrodes (e.g., Ag/AgCl probes) require the use of gel, causing allergenic reactions in a number of patients, flexible dry electrode (FDE) probes require skin preparation step (e.g., shaving body hairs), prior to signal acquisition, bringing about unwillingness in patients for the test. However, microneedle arrays (MNA) not only do not need any gel usage or skin preparation, but MNs also do not suffer from background noise and high signal to noise rate owing to penetrating layers beneath the outermost layer of skin. Adapted with permission from (Ren et al., 2017). Copyright 2017, Elsevier.

and biocompatibility of MNAs, a Ti/Au film was coated on them. Three healthy volunteers recorded their bio-signals by 36-FMAE, flexible dry electrode (FDE), and wet electrode methods, under the same condition. The investigation consisted of four discrete tests (Ren et al., 2017). First, electrode skin interface impedance (EII) was measured with a two-electrode impedance analyzer. Increasing the number of MNs on the array considerably decreased the impedance. This could be attributed to the reduction of multi-parallel impedance as a result of more MNs. Overall, 36-FMAE had the best and lowest impedance compared to that of FDE and wet-electrodes. The second test was an ECG test. Increasing the number of MNs on the array could increase the amplitude of the signal, which is favorable. This effect could be due to the increase in the contact area of needles with the skin because of more MNs. In addition, different types of waves constituting the ECG signal were distinguishable in 36-FMAE since MNs pierce into the skin. Thus, recorded signals by 36-FMAE do not suffer from noise and artifacts caused by moving skin. However, these artifacts are present in FDE and wet electrode signals, which can adversely affect the accuracy of recorded signals. The third test was an EMG measurement, which was performed by using three electrodes on the biceps brachia and elbow. 36-FMAE had the largest signal amplitude. In the case of muscle activation, 36-FMAE traced signals with high fidelity. Finally, the unipolar connection method was used to record EEG signals during an eye-blinking test by an electrode on the earlobe. The shape of the recorded signal by 36-FMAE was analogous to that of the FDE and wet-electrode method. Similar to the other tests, the amplitude of the 36-FMAE signal was larger. Overall, 36-FMAE had an acceptable performance for bio-signal recording when compared to conventional methods. 36-FMAE not only could reduce the motion artifacts and impedance by penetrating the skin, but also it was a cost-effective device (Ren et al., 2017).

In another study, a two-step process, direct-metal-laser-sintering (DMLS) 3D printing and polishing, was used to print MNs from medical-grade stainless steel, with 657 μm height and 250 μm base diameter. MNs post-processed with electropolishing after fabrication, led to enhancing surface roughness as well as reducing tip radius from 51 μm to 19 μm. The results of this study corroborated the superiority of MN-based electrodes over conventional wet/dry electrodes for EMG signal acquisition. Furthermore, the advantageous effect of increasing the number of MNs, in an array, on reducing the electrode-skin impedance was emphasized (Krieger et al., 2020).

2.3. Outlook

Advantages of MNs have recently surged the number of scientific reports regarding diverse types of MNs, including hollow, solid, coated, and dissolvable, with a range of feature sizes for a variety of biomedical applications such as drug delivery, biosignal acquisition, and sample extraction. Moreover, a wide range of MN fabrication methods was proposed: subtractive and additive approaches. This review provides an overview of the working principles of 3D printing methods, highest attainable resolution, supported materials, and advantages as a guideline for the selection of proper fabrication method for future MN applications. Furthermore, the present review provides an overview of the benefits offered by the integration of 3D printing with MNs, applicable 3D printing techniques for MN fabrication, potential applications of MNs, and recent advances.

Regular and contentious monitoring of health and large-scale vaccination are required to control and curb the impact of life-threatening diseases on healthcare systems worldwide. Conventional methods can partially fulfill the demand for regular tests; however, they are associated with low patient compliance, high-cost, and limited accessibility. Substituting present methods with mass-producible, accurate, cost-efficient, point-of-need technologies will substantially reduce healthcare costs and increase life quality globally. MNs are devices with versatile shapes and types that offer numerous benefits such as being low-cost, portable, efficient, precise, and readily available for applications in drug delivery, liquid sample extraction from the body, bio signal acquisition, and point-of-care diagnostics. However, there are some challenges remaining in this area. For example, there is a need for new research on materials that are used to fabricate MNs to increase their ability in the absorption of liquids, either for enabling more drug load in drug delivery applications, or in sample extraction (Zhu, Zhou, Libanori, & Sun, 2020). Moreover, the majority of the reported cases have been studied within mimicking tissues and animals.

Despite the fact that current MN fabrication techniques could yield an acceptable resolution, cost-effectiveness, requiring manual steps, demanding high proficiency in the micromanufacturing for proper implementation, and being labor-intensive are existing limitations of conventional methods. 3D printing is a promising approach for MN fabrication since proposed MNs with desired size features can be designed, modified, and fabricated directly, truncating the design and prototyping process by eliminating the need for third-party manufacturing companies. However, slow printing, resolution confinements, limited material choice, and biocompatibility are serious challenges of 3D printing (Zhangwei Chen et al., 2019; Ligon et al., 2017). Although the terms “3D printing” and “rapid-

prototyping" have been used interchangeably, the actual 3D printing process is not as fast as conventional industrial approaches, such as inject molding (Ligon et al., 2017). Moreover, regardless of the substantial attention received by 3D printing, achieving higher resolution is an existing challenge. SLA, TPP, and DLW can produce MNs with acceptable resolutions (5 μm), nevertheless, limited biocompatible materials are supported with these methods, while mechanical properties are not of a satisfactory degree (Chia & Wu, 2015; Ligon et al., 2017; Ngo et al., 2018; Yao et al., 2020). Therefore, future studies can be focused on developing faster 3D printing methods without compromising the resolution. By enhancing features of the laser beam, in laser-based methods, and nuzzle features, in extrusion-based methods, the ultimate resolution of printed MNs can be realized.

Chapter 3: Finger-Actuated Microneedle Array for Sampling Body Fluids

Abstract: The application of microneedles (MNs) for minimally invasive biological fluid sampling is rapidly emerging, offering a user-friendly approach with decreased insertion pain and less harm to the tissues compared to conventional needles. Here, a finger-powered microneedle array (MNA) integrated with a microfluidic chip was conceptualized to extract body fluid samples. Actuated by finger pressure, the microfluidic device enables an efficient approach for the user to collect their own body fluids in a simple and fast manner without the requirement for a healthcare worker. The processes for extracting human blood and interstitial fluid (ISF) from the body and the flow across the device, estimating the amount of the extracted fluid were simulated. The design in this work can be utilized for the minimally invasive personalized medical equipment offering a simple usage procedure.

3.1. Introduction

Since their inception in 1976 as a drug delivery device (Gerstel & Place, 1976) until 2020 to be regarded as one of the top ten emerging technologies (*World Economic Forum Top 10 Emerging Technologies (www.weforum.org/reports/top-10-emerging-technologies-2020)*, 2020), microneedles (MNs) have presented many advantages in injection processes, including minimizing insertion pain and reducing tissue damage and controlled drug delivery as compared to the conventional needle technologies. With different geometries and designs (Chang et al., 2020; Kevin J Krieger et al., 2019) such as solid, hollow, coated or biodegradable (Yokoyama et al., 2020) needles types in the scale of micrometers and nanometers (Chiappini et al., 2015), microneedle arrays (MNAs) can be fabricated with numerous methods such as 3D printing (Cordeiro, Tekko, Jomaa, Vora, McAlister, Volpe-Zanutto, Nethery, Baine, Mitchell, et al., 2020; Dabbagh et al., 2021). MNAs can be inserted into a target area even within the depth of skin epidermis and thus they have emerging biomedical applications in drug delivery systems (Amer et al., 2020; Kang et al., 2020; Kusama et al., 2021; J. Yang et al., 2020) with the capability of programmed deliveries of drug doses for multiple-injection-therapies such as vaccination (Tran et al., 2020), sampling interstitial fluid (ISF) (Samant et al., 2020; Zheng et al., 2020) biomarker detection (Wang et al., 2021), enhanced wound healing (Frydman et al., 2020), fertility control (W. Li et al., 2019), point-of-care (POC) setups and diagnostic tests (Jiang & Lillehoj, 2020; Xie et al., 2020), DNA extraction (Paul et al., 2019; B. Yang et al., 2020), cancer therapy (Moreira et al., 2019), and force sensing (Ke & Chung, 2020).

Computational methods that allow simulating the experiment or setup conditions for prognosticating their behaviors with conceivable problems or using artificial intelligence techniques for post analysis of data (Rezapour Sarabi et al., 2021), have also emerged in MNs. COMSOL Multiphysics, a finite element analysis software, was used for simulating the transdermal drug delivery process of MNs into the skin, to study the effect of penetration depth and number of MNs on each patch, demonstrating increasing proportionality of delivered drugs with both factors (Castilla-Casadiego et al., 2021). To study the Von Mises stress, an

index of yield or fracture in materials, in a design of MNAs with triangular-shaped bases, the Structural Mechanics module of COMSOL Multiphysics was utilized, demonstrating that the MNs in the middle part of the array were under more stress and displacement (Loizidou et al., 2016). In addition, using COMSOL, in a microfluidic system with MNs including a drug reservoir, displacement of MNs was modeled and simulated (Rajeswari & Malliga, 2013). Structural analysis of MNs was also reported (Kanakaraj et al., 2015). In another study using finite element analysis (FEM) of COMSOL Multiphysics, the bending procedure and the distribution of the loaded stress on the MNs during their insertion into the skin were simulated (Faraji Rad et al., 2017). A circular flange was introduced to the base of each MN as the results of the simulation demonstrated that MNs were most likely to fail in the area between the needle body and the supporting array because of stress concentration in this spot. Furthermore, COMSOL was used to study modeling the surface concentration profiles of the delivered drug in a MN design with hemispherical convexities on the needle for the aim of increasing drug delivery flux (Zoudani & Soltani, 2020).

In this study, a microneedle array (MNA) integrated with a microfluidic channel chip was designed to extract and sample body fluids powered by finger press, featuring an easy procedure that can be applied by the user without need for the presence of healthcare workers. This design contains an array of 100 MNs with co-centric circular holes for fluid transport. The target fluid, for example blood or interstitial fluid (ISF), can be extracted by the power created by pressing with fingers followed by flowing in the microfluidics and finally being collected in a reservoir. The process of fluid flow and its transport across the device and its collection was modeled and simulated with COMSOL Multiphysics. The amount of the extracted fluid was studied with the simulation along with the generation of the curves for mass flow rate at the reservoir.

3.2. Methods

3.2.1. Design of the device

The microneedle array (MNA) with a microfluidic chip was designed to be powered by pressing with finger (**Figure 3.1a**). The device was designed with Dassault Systèmes (3DS) SolidWorks computer-aided design (CAD) and computer-aided engineering (CAE). The microfluidic chip was designed as a box with the dimensions of length (L=40 mm), width (W=20 mm), and height (H=9.3 mm) (the final height of the device with the MNA integrated is 10 mm). The design of the microfluidic system (**Figure 3.1b**) included a deformable dome-shaped chamber for mechanical pressure input by pressing with finger to provide a force to guide the fluid from the MNA inlet to the reservoir outlet. The MNA was connected to a duct that guided the extracted fluid to the reservoir via the channels with a diameter of 2 mm. The designed MNs and their geometry are shown in **Figure 3.1c**.

For designing the MNs, experimentally reported MNs with applications in sampling or extraction of body fluids such as ISF, blood, and glucose detection were reviewed and the geometrical properties of the MNs, which included the height of the needle, its base diameter, the needle tip diameter, and the distance between the MNs in case of MNAs, along with the efficiency of the reported investigation were shown in **Table 3.1**. To choose a convenient design for the MNs, the reported data were used to create chart boxes of the data (**Table 3.2**).

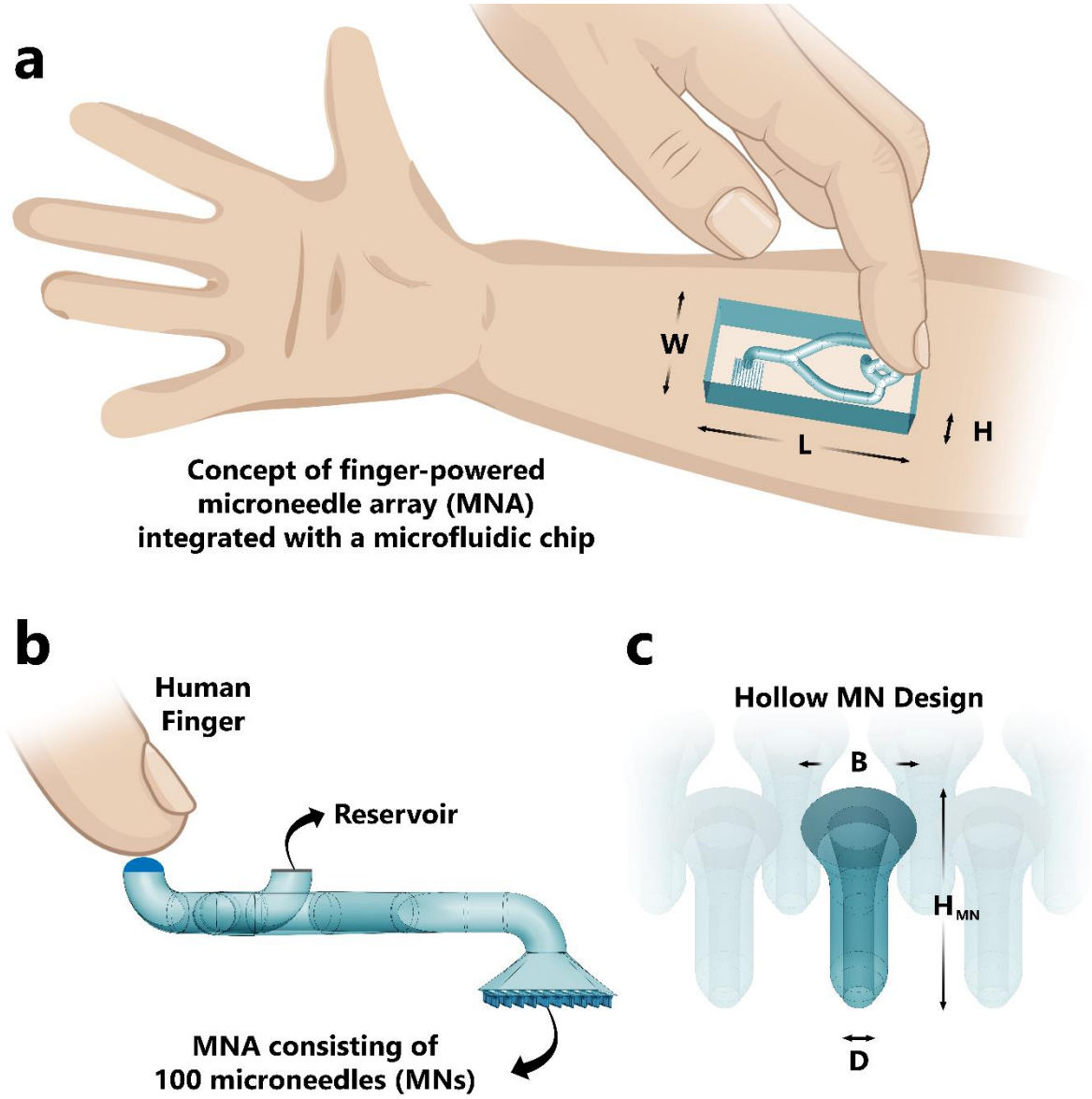

Fig 3.1. Concept of finger-powered microneedle array (MNA) integrated with a microfluidic chip for the aim of extracting body fluid samples. (a) The device is designed to be powered by pressing with finger, hence enabling a simple approach that the user can sample easily without need for healthcare workers, as shown schematically. The dimensions of the designed device are: length, L=40 mm, width, W=20 mm, and height, H=9.3 mm. (b) The design of the channels of the chip, in which the array of 100 microneedles (MNs) is connected to a duct that guides the extracted fluid to the reservoir via the channels, by the means of pressing with finger. (c) The geometry of each MN, consisting of a hollow design with these dimensions: height, H_{MN}=700 μm, diameter of the needle tip, D=80 μm, and the diameter of the needle base, B=300 μm.

The table shows the box chart for the reported MN height in μm with most of the reported heights of MN to be in the range of 400 μm to 800 μm. Commercial MN vaccine delivery systems, have mostly a height of 600 μm (Lee et al., 2020). As a result, it is appropriate to design a MN with a height in this domain. The MNs in this work has a needle height of H_{MN}=700 μm. According to the data of the base

diameter of the previously reported MNs (**Table 3.2**), the diameter of the needle base was designed as B=300 μm. The diameter of the needle tip was designed to be D=80 μm. The box charts for the number of the MNs in an array and the interspacing between the MNs are demonstrated in **Table 3.2**. MNA in the present work was designed in an area of 6 mm × 6 mm, consisting of 100 microneedles (MNs) with interspacing of 600 μm MNs' center-to-center distance.

On the other hand, the required force for penetration of the microneedles into the skin, can be easily provided by the user. Precise measurements of the required insertion force for MNs were previously reported, showing that an amount in the range of 0.03 to 0.4 N per MN is sufficient for piercing the stratum corneum (SC) and insertion into the skin (Davis et al., 2004; Olatunji et al., 2013; Wang et al., 2021), which is low enough to allow insertion by hand (Davis et al., 2004). In addition, according to the experimental literature presented in the **Table 3.1**, MNs with similar design to that of the present work adequately penetrated human skin, demonstrating potency of proposed MNs for penetration.

Table 3.1. Geometrical properties of experimentally reported microneedle arrays (MNAs) with applications in sampling or extraction of body fluids

#	Aim of the work	H_{MN} B D	MN number in array, MN interspacing	Extraction or sampling amount of each MN	Ref.
1	Glucose detection	400 μm - -	1 -	4 to 7 mM	(Nicholas et al., 2018a)
2	Skin penetration of MNs	600 μm 300 μm -	4, 9, 16 30 to 600 μm	-	(Olatunji et al., 2013)
3	Blood extraction	1,800 μm - 120 μm	1 -	20 μL	(Li et al., 2013)
4	Skin ISF extraction	600 μm 300 μm -	121 100 μm	~ 0.02 mg	(Zhu, Zhou, Kim, et al., 2020)
5	RhB absorption using hydrogel MNs	700 μm - -	6 -	~ 4.2 mg/L	(Yao et al., 2020)
6	ISF extraction	1,000 μm and 1,500 μm - -	16, 32 -	Flat profile geometry: 0.028± 0.021 μL/min Concave profile geometry:	(Taylor et al., 2020a)

				0.053 ± 0.040 µL/min Convex profile geometry: 0.020 ± 0.013 µL/min Bevel profile geometry: 0.028 ± 0.029 µL/min	
7	Collecting PBS, a liquid model for ISF	1,000 µm 1,000 µm -	21 3,000 µm	~ 7.15 mg	(Takeuchi et al., 2019a)
8	Skin ISF extraction	250 µm, 450 µm, and 650 µm 200 µm 10 µm	5 -	0.46 ± 0.52 µL	(Samant et al., 2020)
9	Dermal ISF extraction	1,000 µm, 1,500 µm, and 2,000 µm - -	5 -	4 µL (Humans) 12 µL (Rats)	(Miller et al., 2018)
10	Detection of drugs and glucose	600 µm 300 µm -	361 50 µm	Caffeine detection: ~ 0.25 µg/mL Glucose detection: ~ 0.022 nmol/L Glucose extraction: ~ 0.011 nmol/L	(Caffarel-Salvador et al., 2015)
11	PBS Absorption	550 µm 200 µm -	225 500 µm	~ 200% weight gain	(Fonseca et al., 2020)
12	ISF extraction	900 µm 280 µm -	100 -	Extraction from pig skin: ~ 0.079 µL Extraction from rat skin: ~ 0.0382 µL	(Zheng et al., 2020)
13	Detection of nucleic acid biomarkers from skin ISF	550 µm 250 µm -	49 340 and 400 µm	~ 0.133 µL	(Al Sulaiman et al., 2019)

14	ISF extraction	680 µm 380 µm -	144 -	0.0250 ± 0.0042 mg	(J. Chen et al., 2019)
15	Dermal ISF extraction	750 µm, and 650 µm 100 µm × 70 µm, and 50 µm × 150 µm <1 µm	5, 9 -	8 to 97 nL	(Kolluru et al., 2019)
16	Skin ISF extraction	520 µm - -	100 -	0.01 to 1 µL	(Samant & Prausnitz, 2018)
17	ISF extraction	1,500 µm - -	5 -	8 to 12 µL	(Taylor et al., 2018)
18	Skin ISF extraction	800 µm 250 µm -	100 450 µm	0.023 ± 0.004 µL	(Chang, Zheng, Yu, Than, Seeni, Kang, Tian, Khanh, Liu, & Chen, 2017)
19	Transdermal detection of methyl paraoxon (MPOx)	1,500 µm - -	9 1,000 µm	20 to 180 µM	(Mishra et al., 2017)
20	Detection of skin ISF biomarkers	800 µm 150 µm -	16 -	-	(X. Zhang et al., 2019)
21	Skin ISF extraction	1266 ± 91 µm 500 ± 31 µm -	100 -	0.0125 to 0.075 mg	(He et al., 2020)
22	Blood extraction	1,800 µm - 130 µm	1 -	31.3 µL	(Li et al., 2015; C. G. Li et al., 2012)

Table 3.2. Box charts of geometrical properties of MNAs reported in Table 3.1

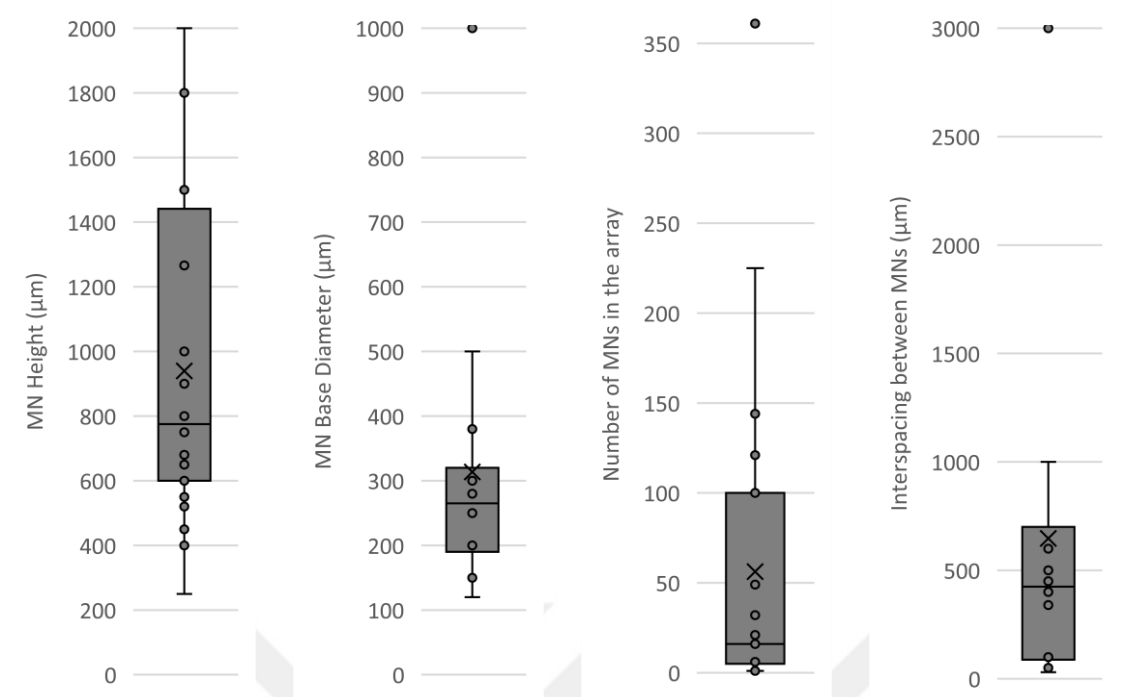

Legend: The dots (o) represent the reported data. The cross marks (×) represent the mean. The vertical lines inside the boxes represent the median.

3.2.2. Boundary Conditions (BCs) and Simulation

The design in this work consists of two inlets and one outlet, which are (i) the input for the mechanical pressure *via* finger, (ii) the inlet for the target fluid, and (iii) the outlet to the reservoir. For simulating the process of human finger pressing, experimental data of previously designed finger-powered microfluidics device was used (Iwai et al., 2014). The average pressure created by human finger pressing is ~4500 Pa. For pressing with a time interval of every 5 s, the following pressure-time function can be developed:

$$P(t) = 2250 * \cos\left(\frac{2\pi}{5} * t\right) + 2250 \qquad (3.1)$$

where "t" is time in seconds and "P" is pressure in Pascals. **Eq. 3.1** was the base function for the pressure boundary condition (BC) at the finger pressure input. To study the effect of the force input by pressing with fingers, the function of **Eq. 3.1** was modified into a version, where it defines pressing 5 times faster:

$$P(t) = 2250 * \cos(2\pi * t) + 2250 \qquad (3.2)$$

Eq. 3.2 means that the user is pressing the dome-shaped chamber every second. In this equation "t" is time in seconds and "P" is pressure in Pascals. Human blood was chosen as the first target fluid, aimed to be collected with the designed device. Blood is a non-Newtonian fluid, in which the viscosity has been reported to be modeled with several mathematical equations (Hund et al., 2017). The Power-law model (**Eq. 3.3**) was used for the viscosity equation in the simulation:

$$\mu = k\dot{\gamma}^{n-1} \qquad (3.3)$$

where "μ" is the viscosity of the blood and "$\dot{\gamma}$" is the shear rate. The coefficients of "k" and "n" for blood are 0.42 and 0.61, respectively (Hund et al., 2017; Sequeira & Janela, 2007). In addition, the blood density was defined as an amount equal to 1060 kg.m^{-3}. High-resolution blood flow velocity in the human finger was reported (Klarhöfer et al., 2001) with measurement of arterial blood flow velocities ranging from 0.049 to 0.19 m.s^{-1}, and venous blood flow velocity in the range of 0.015 to 0.071 m.s^{-1}. Also, the blood flow rate in the arm at rest was reported to be 0.21 ± 0.04 L.min^{-1} (Ahlborg & Jensen-Urstad, 1991). In addition, the amounts of blood pressure in the human arms in sitting and supine position were reported (Netea et al., 2003), with systolic blood pressure (SBP) 135.5 ± 24.0 mmHg and diastolic blood pressure (DBP) 79.2 ± 9.7 mmHg for sitting position and amounts of SBP = 145.0 ± 23.2 mmHg and DBP = 84.1 ± 9.0 mmHg for supine position. On the other hand, the normal human heart rate at rest is in the range of 60 to 100 beats per minute (Jose & Collison, 1970; Ostchega, 2011). Taking 80 beats per minute with SBP of 135.5 mmHg (≈ 18,000 Pa) and DBP of 79.2 mmHg (≈ 10,000 Pa) as the average amounts, an equation of blood pressure in the vessels like **Eq. 3.4** can be derived:

$$P(t) = 4000 * \cos\left(\frac{13\pi}{5} * t\right) + 14000 \qquad (3.4)$$

where "t" is time in seconds and "P" is pressure in Pascals. **Eq. 3.4** and alternatively a simplified constant pressure value were used as the BC for the blood input. A second series of simulations were performed for ISF collection. The viscosity of the ISF in the literature was reported to be in the range between 1.2-1.5 × 10^{-3} Pa.s (Ebah, 2012) to 3.5 × 10^{-3} Pa.s (Yao et al., 2012). In this work, an average amount of 2.5 × 10^{-3} Pa.s was used. In addition, the density of ISF was reported to be 1000 kg.m^{-3} (Yao et al., 2012). The input BC for ISF was defined with ISF pressure, which is in the range of -0.5 to -8.0 mmHg (Ebah, 2012), with the negative sign attributing to the action of lymphatics (Aukland & Reed, 1993). An average value of 4 mmHg was utilized in the simulation. Additionally, the BC for the reservoir for all the cases was set to be pressure of zero. The simulation of the fluid transport across the designed device was performed with COMSOL Multiphysics, generating the flow curves at the reservoir outlet along with pressure and velocity gradients across the device. The physical time of 5 s was used as the study time in all simulation cases, as the highest amount of period time among the utilized trigonometric equations was 5 s. In total, 6 different cases were studied with the simulation (**Table 3.3**).

Table 3.3. The simulated cases of the present study, for two different fluids and various boundary conditions (BCs)

Case	Target Fluid	BC 1 (Pressure Input by Finger)	BC 2 (Reservoir)	BC 3 (Fluid Inlet from MNs)
1	Human Blood	$P(t) = 2250 * \cos\left(\frac{2\pi}{5} * t\right) + 2250\ [Pa]$	$P = 0$	$P = 135\ mmHg$

2	Human Blood	$P(t) = 2250 * \cos(2\pi * t) + 2250\ [Pa]$	$P = 0$	$P = 135\ mmHg$
3	Human Blood	$P(t) = 2250 * \cos\left(\frac{2\pi}{5} * t\right) + 2250\ [Pa]$	$P = 0$	$P(t) = 4000 * \cos\left(\frac{13\pi}{5} * t\right) + 14000\ [Pa]$
4	Human Blood	$P(t) = 2250 * \cos(2\pi * t) + 2250\ [Pa]$	$P = 0$	$P(t) = 4000 * \cos\left(\frac{13\pi}{5} * t\right) + 14000\ [Pa]$
5	Interstitial Fluid (ISF)	$P(t) = 2250 * \cos\left(\frac{2\pi}{5} * t\right) + 2250\ [Pa]$	$P = 0$	$P = 4\ mmHg$
6	Interstitial Fluid (ISF)	$P(t) = 2250 * \cos(2\pi * t) + 2250\ [Pa]$	$P = 0$	$P = 4\ mmHg$

3.3. Results and discussion

The simulation was run for 6 different cases of **Table 3.3**, which included 4 cases for human blood with various BCs and 2 cases for ISF with various BCs. **Figure 3.2** shows the created mesh used for the studies. For Study Case 3 in **Table 3.3** (input function of the heartbeat imitation for the incoming human blood and pressing the mechanical pressure input button every 5 s), the field of the velocity in the direction perpendicular to the cross section of the reservoir channel was visualized in every second (**Figure 3.2a**), along with a magnified view for one of the MNs (**Figure 3.2b**). The velocity-time graph for the MNs is shown in **Figure 3.2c**. In the 5th second, the velocity reached its maximum amount of around 0.25 m.s^{-1}, or equivalently 2.436 µL.s^{-1} of human blood output at the reservoir per needle. An experimental setup of an MN devices for collecting mouse blood sample, reported an extraction rate of 0.8 µL.s^{-1} per needle (Li et al., 2013). Hence, the present device has the potential to collect samples 3 times faster.

Figure 3.3 illustrates the pressure distribution results of the simulation. For ISF and pressing the mechanical pressure input button every 5 seconds (Study Case 5 in **Table 3.3**), the pressure distribution in the 5th second is presented in **Figure 3.3a**. **Figure 3.3b** shows the magnified view of the MNA area. For human blood, the pressure distribution in the device, with input function of the heartbeat imitation and pressing the mechanical pressure input button every 5 seconds (Study Case 3 in **Table 3.3**) is demonstrated in **Figure 3.3c** for every second along with the magnified view of one MN in **Figure 3.3d**.

Figure 3.4a shows the schematics of the designed device with referrals to the BCs. For the Case Study 1 in **Table 3.3**, which utilized **Eq. 3.1** as the BC for the finger pressing dome and average blood pressure of 135 mmHg as the BC for the coming blood from the MNs, the simulation results in mass flow-time curve in the reservoir as shown with red color in **Figure 3.4b**. In the second running of the

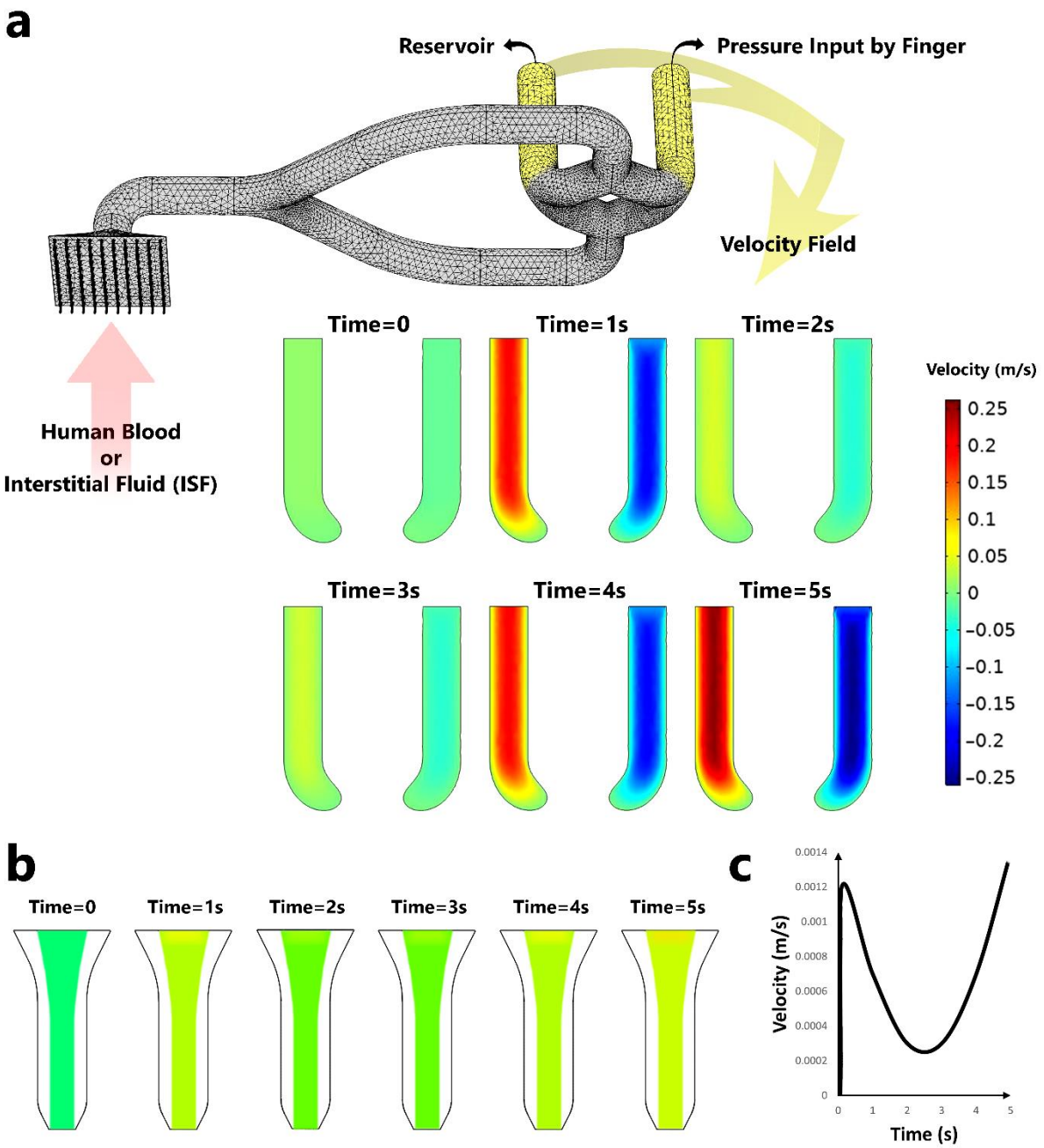

Fig 3.2. Representation of the created mesh and results of the velocity field. (a) The mesh that was created for the study is represented here. In the highlighted area in yellow, the velocity field results in the direction perpendicular to the cross section of the channels are shown, with the function of the heartbeat imitation for the incoming human blood and pressing the mechanical pressure input button every 5 seconds (study case 3 in Table 3). In the 5th second, the velocity reaches its maximum amount of around 0.25 m.s-1. (b) The velocity field for one of the MNs in the patch from time=0 to 5 seconds and (c) its corresponding velocity-time curve. The color bar shows velocity in m/s.

simulation, the BC for the finger pressure input was changed from **Eq. 3.1** to the function given at **Eq. 3.2**, resulting in the mass flow-time curve in the reservoir as shown with red color in **Figure 3.4c**. Since at least one of the BCs was

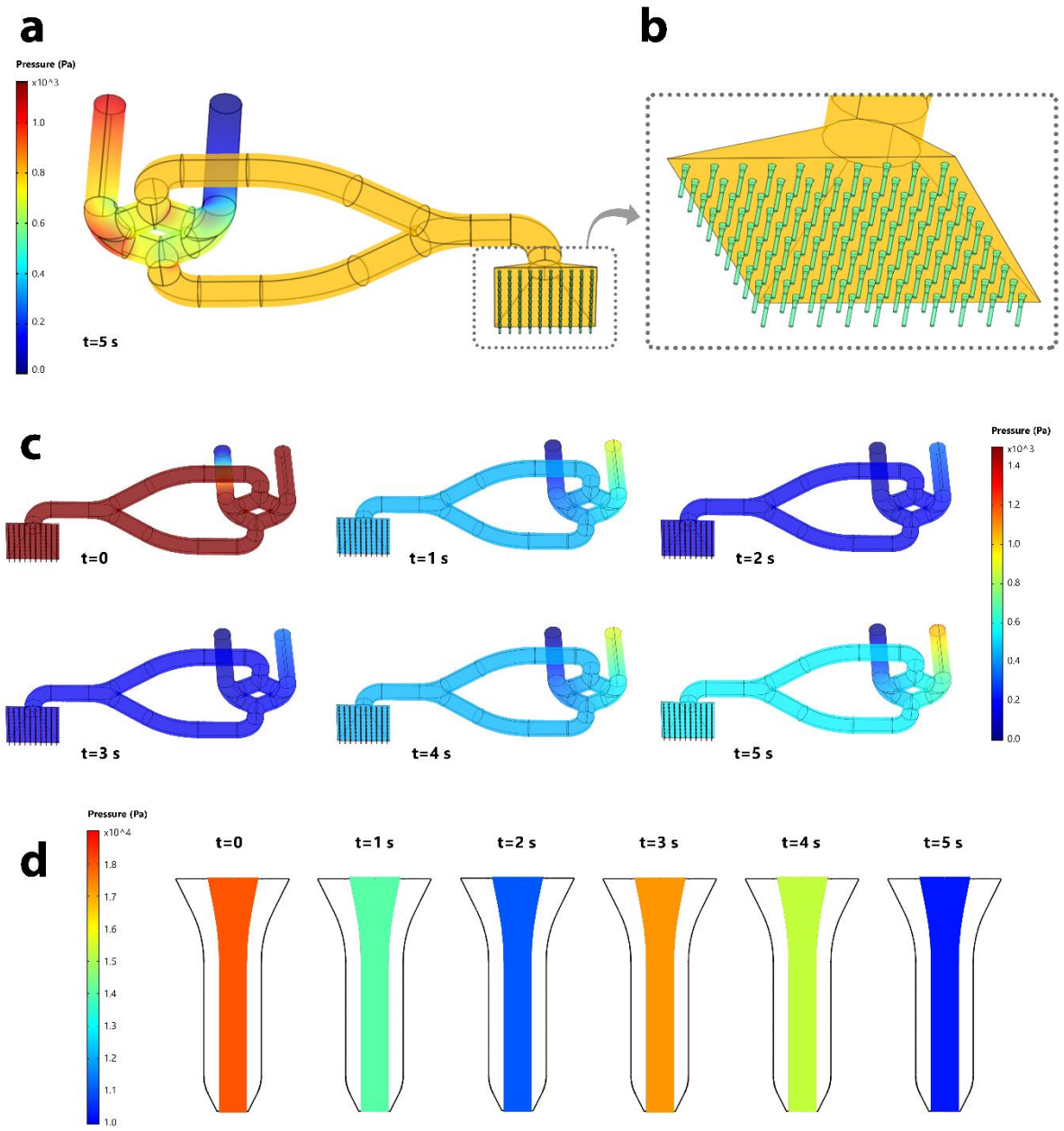

Fig 3.3. Pressure distribution results. (a) For interstitial fluid (ISF) and pressing the mechanical pressure input button every 5 seconds (study case 5 in Table 3), the pressure distribution in the 5th second is represented here along with (b) the magnified view of the microneedle array (MNA) area. (c) Pressure distribution in the device for human blood with input function of the heartbeat imitation and pressing the mechanical pressure input button every 5 seconds (study case 3 in Table 3), and (d) the magnified view of one microneedle (MN). All color bars show the amount of pressure in Pascals (Pa).

trigonometric, as expected, both curves that resulted from the simulation, were also trigonometric.

The function in **Eq. 3.4** was also simulated. Cases 3 and 4 in **Table 3.3**, use this equation for the incoming human blood along with slow finger pressure input (**Eq. 3.1**) and fast finger pressure input (**Eq. 3.2**), respectively. The mass flow-

time curves at the reservoir for these two cases are presented in **Supplementary Figure 3.S.1** and **3.S.2**, respectively. Among two states of using a constant pressure for the human blood inlet and heartbeat imitation function of **Eq. 3.4**, a small amount of difference in the mass flow rate was detected. While the pressure function imitated the heartbeat action and offered a more realistic study condition, the resulting mass flow rate, and hence the amount of the extracted blood, was smaller.

In another series of simulations, ISF was used as the target fluid. First **Eq. 3.1** was used as the BC for the finger pressing dome (Case 5 in **Table 3.3**) followed by a second run with **Eq. 3.2** (Case 6 in **Table 3.3**) to study the effect of the force input speed by pressing with fingers. The mass flow curve results at the reservoir are shown with the yellow color in **Figure 3.4b-c**, for the state of slow (Case 5, **Table 3.3**) and fast (Case 6, **Table 3.3**), respectively.

By integrating the area under the curves, the amount of the extracted fluid was calculated. **Figure 3.4d** in the left vertical axis shows the total amount of the extracted blood in grams in 5 s, with each line representing one of the four different criteria that was used for blood in the simulation (Cases 1 to 4 in **Table 3.3**). The heartbeat-representing function simulations resulted in a lower amount of blood extraction and pressing the button resulting in a subtle increase in the blood extraction amount. The device design included an MNA patch of 100 MNs, with each MN extracting the amounts in microliters (μL) in 5 s as shown in the right vertical axis of **Figure 3.4d**. Among experimental setups of the MN devices for collecting blood samples, a study reported extraction of 4 μL of mouse blood *in vivo* in 5 s per one needle (Li et al., 2013). Another study reported extraction of around 39 μL rabbit blood *in vivo* per one needle in 5 s with a pre-vacuum system (Li et al., 2015). The results in the present work with an average extraction of 12.24 μL human blood in 5 s per needle, fall in the range of the experimentally reported cases.

For ISF extraction in two states of slow (Case 5, **Table 3.3**) and fast (Case 6, **Table 3.3**), the extraction amounts slightly increased in fast mode (**Figure 3.4e**), with the left vertical axis for the total extracted ISF in grams in 5 s. The MN patch included 100 needles. The average amount that each needle extracted in microliters in both states of slow and fast, are represented in the right vertical axis of **Figure 3.4e**. The simulation results in an average extraction of 64.5 μL ISF in 5 s per needle.

The simulation results for the amounts of ISF extraction, which was higher than the previous reports, could be partially attributed to the mechanism of the extraction and the dissimilarities between the properties of the ISF of humans and animals. While the mechanism of ISF extraction in majority of reports is on the basis of swellable materials, our design offers a high volume for fluid extraction rather than a limited volume of swellable needles. On the other hand, diffusion plays the main role in swelling, which is a slow procedure, requiring long durations of administration time such as a full day (Donnelly et al., 2014) or in some cases three weeks (Chang, Zheng, Yu, Than, Seeni, Kang, Tian, Khanh, Liu, & Chen, 2017) to reach a meaningful result. In contrast, the device reported in this work is powered by finger pressure input, which not only offers a greater force for extraction in comparison with the natural-occurring diffusion, but also can be controlled very conveniently by pressing faster, enabling the extraction of ISF in

higher volumes. Furthermore, as higher extraction rates are projected for human ISF compared to animal ISF (Chang, Zheng, Yu, Than, Seeni, Kang, Tian, Khanh, Liu, & Chen, 2017), the dissimilarity between the properties of human and animal ISFs can be another reason for the extraction discrepancy. A previous research study on the extraction of ISF from mice, has also stated that they anticipate a greater result in humans (Chang, Zheng, Yu, Than, Seeni, Kang, Tian, Khanh, Liu, & Chen, 2017).

In addition, the extraction of ISF resulted in a higher efficiency when compared to the human blood (**Figure 3.4**). Since both the density and viscosity of ISF are lower than that of blood, the same finger pressure results in a greater extracted amount of ISF at the reservoir with less effort.

The simulation results for the presented cases in this work showed a successful extraction of the target fluid. One of the widely used components in microfluidic platforms is diode due to their capability of changing fluid direction on-demand. Microfluidic diodes are a category of membranes which deform to an open shape in contact with the forward pressure of the flow, allowing the fluid to pass through the channel. Conversely, the diode closes when there is a backward fluid pressure, hence offering a great way for rectifying the flow (Adams et al., 2005; Grover et al., 2003). Further studies on finger-powered microneedle research can benefit

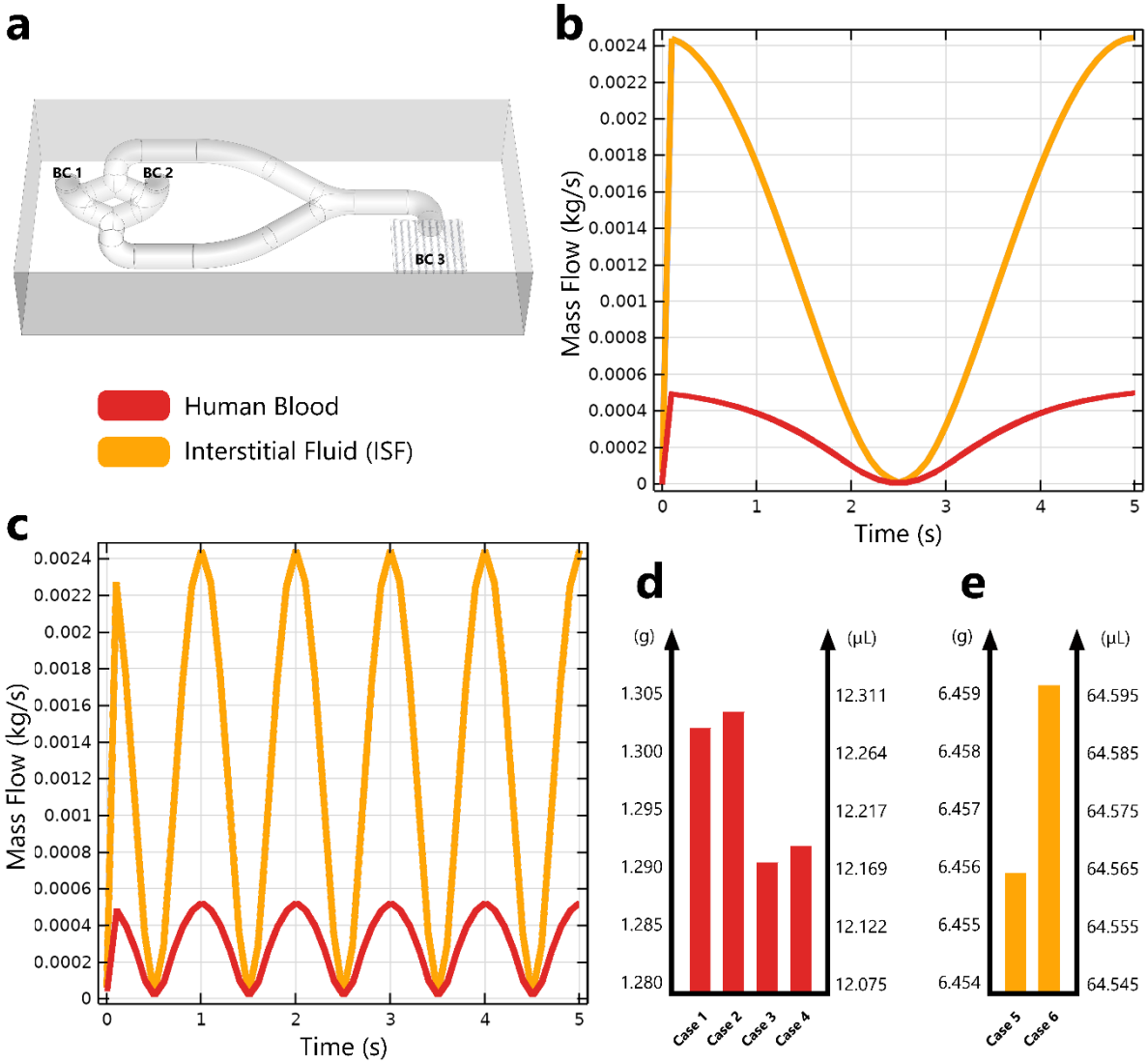

Fig 3.4. Mass flow-time curves at the reservoir and fluid extraction efficiency results. Two different fluids, human blood and interstitial fluid (ISF), with various boundary conditions (BCs) were used for simulation, which created a total of 6 different cases (organized in Table 3). (a) Representation of the device, and the referrals to the defined BCs. (b) The mass flow curve result at the reservoir for Case 1 and Case 5, presented in red and yellow, respectively. (c) The mass flow curve result at the reservoir for Case 2 and Case 6, presented in red and yellow, respectively. The curves at (b) and (c) show the mass flow rate in kg.s-1 for time in seconds for a duration of 5 seconds. (d) Amounts of human blood extraction (Cases 1 to 4), with the left vertical axis representing the total amount of the extracted human blood in grams, over a duration of 5 seconds, and the right vertical axis representing the average amount of human blood extraction for each needle in microliters (μL) over a duration of 5 seconds. (e) Amounts of ISF extraction (Cases 5 and 6), with the left vertical axis representing the total amount of the extracted ISF in grams, over a duration of 5 seconds, and the right vertical axis representing the average amount of ISF extraction for each needle in microliters (μL) over a duration of 5 seconds.

from the integration of diodes. For example, the utilization of microfluidic diodes was reported for a successful manipulation of the flow direction in a finger-powered microfluidic setup (Iwai et al., 2014).

3.4. Outlook

Administration of new proactive healthcare procedures and technologies in medicine not only requires effective adoption by the society, but also well-informed framework to address any potential insecurity or anxiety concerns in patients, preventing any negative psychological effects (Paré et al., 2006; Safi et al., 2018). Causing discomfort/pain or trypanophobia/needle phobia in patients, injection using traditional needles requires a trained healthcare worker, confining applicability of conventional needles in deprived regions or in-home treatments. One of the advantages that MNs and MNA-based devices offer in comparison to the conventional needle technologies, is their solution for the fear of needles. A statistical study reported that 7 out of 10 children and 5 out of 10 adults, are needle phobic (Kettwich et al., 2007), which demonstrates the need for a substituting devices offering painless injection procedures. On the other hand, MNs can be administrated by patients in the point-of-care settings (no need for healthcare workers) with minimal pain. An additional ability offered by MNs is the gradual release of substances for controlled drug delivery (Nagarkar et al., 2020), promoting the potential applications of MNs for longer term treatments. Furthermore, microneedles can be integrated with biosignal acquisition techniques (Dabbagh et al., 2021). Therefore, MNs not only enable a minimally-invasive injection experience, but they also can facilitate the development of wearable sensors (Teymourian et al., 2021) (with adherable MN patches) for continuous health monitoring, resulting in early diagnosis of disease, enhancing the success rate of therapies, decreasing healthcare costs, and ultimately promoting the wellbeing of the society. Hence, the acceptance and commercialization of MNs can be accelerated. In addition, in the last decade, many patents have been filed in MNs (Ali et al., 2019), indicating the high interest in this domain and their potential for a variety of drug delivery applications.

MNs, as an emerging technology, need to be translated from laboratory bench to commercial products. Fabrication methods that are used for manufacturing microfluidic devices and MNs are rapidly advancing to more cost-efficient procedures (Faustino et al., 2016; Johnson & Procopio, 2019), leading to techniques that no longer require high-cost cleanroom facilities (Nejad et al., 2018b). On the other hand, employment of mass producible manufacturing techniques (*e.g.*, replica molding (Park et al., 2016)) can reduce the overall production cost of MNs to have a competitive price with the conventional needles. In addition, in comparison to conventional needles that are usually made of stainless steel, MNs can be fabricated with low-cost materials such as polymers (Ali et al., 2019), lowering the final cost of the product, making MNs a more economical solution in biomedical applications (Ali et al., 2019). For example, a cost-effectiveness analysis compared the utilization of MNs to conventional needles, reporting an estimation of US$ 0.95 for MNs, and US$ 1.65 for conventional needles for the first dose of a vaccine delivery (Adhikari et al., 2016).

The process of sterilization of MNs prior to applying them into the skin requires high attention, especially in the presented setup which is aimed to be used by the user or patient rather than a healthcare worker. Sterilization allows for preventing the transmission of bloodborne pathogens such as Hepatitis B (HBV), Hepatitis C (HCV), Human Immunodeficiency Virus Infection and Acquired Immunodeficiency Syndrome (HIV/AIDS), malaria, and brucellosis. The materials for the fabrication of the MNs should be biocompatible to prevent any unwanted inflammations or allergies. Furthermore, for the case of blood collection, the extracted blood in the reservoir of the device is subject to undergo coagulation or erythrocyte aggregation if there is a long delay before analysis.

The concept of a finger-actuated device with integration of microneedle array (MNA) and a microfluidic chip was designed for extracting body fluid samples such as blood and ISF in a simple and fast manner. By utilization of COMSOL Multiphysics, the process of extracting human blood from the body was simulated in different conditions. The simulation results demonstrated that our device was capable of extracting around 15.5 g of human blood in 1 min. In addition, a second series of simulations demonstrated extraction of 77.4×10^3 μL of ISF in 1 min. 3D printing technologies which are well-known for printing both MNs and microfluidics chips, can also be utilized for fabrication of our device in a cost-efficient way. The ability to use a biocompatible material in 3D printing is another potential advantage for the fabrication of the device. With integration of personalized analysis tests and data processing, this device can be utilized in minimally invasive personalized medical equipment offering a simple usage procedure.

Chapter 4: Machine Learning-Enabled Prediction of 3D-Printed Microneedle Features

Abstract: Microneedles (MNs) introduced a novel injection alternative to conventional needles, offering a decreased administration pain and phobia along with more efficient transdermal and intradermal drug delivery/sample collecting. 3D printing methods have emerged in the field of MNs for their time- and cost-efficient manufacturing. Tuning 3D printing parameters with artificial intelligence (AI), including machine learning (ML) and deep learning (DL), is an emerging multidisciplinary field for optimization of manufacturing biomedical devices. Herein, we presented an AI framework to assess and predict 3D-printed MN features. Biodegradable MNs were fabricated using fused deposition modeling (FDM) 3D printing technology followed by chemical etching to enhance their geometrical precision. DL was used for quality control and anomaly detection in the fabricated MNAs. Ten different MN designs and various etching exposure doses were used create a data library to train ML models for extraction of similarity metrics in order to predict new fabrication outcomes when the mentioned parameters were adjusted. The integration of AI-enabled prediction with 3D printed MNs will facilitate the development of new healthcare systems and advancement of MNs' biomedical applications.

4.1. Introduction

Microneedles (MNs), which are basically needles in the scale of micrometers at most, are robustly growing (Ingrole et al., 2021) pioneers of the minimally invasive injection procedures, enabling more advanced delivery/collecting systems (Cai et al., 2021; Sarabi, Ahmadpour, et al., 2021). In comparison with conventional needle technologies, MNs are verified to be more advantageous by decreasing the administration pain (Haq et al., 2009) and curtailment of anxiety and needle phobia (Gill et al., 2008), along with being more cost-efficient for drug delivery (Adhikari et al., 2016). Furthermore, transdermal and intradermal injections using MNs are more efficient since they can directly access the skin dermis by penetration through the stratum corneum (Chi et al., 2022). Among the various techniques developed for microneedle arrays (MNAs) fabrication, 3D printing is an emerging accessible method for their time- and cost-efficient manufacturing (Dabbagh et al., 2021; Sarabi, Bediz, et al., 2021). Available in different technologies such as fused deposition modeling (FDM), stereolithography (SLA), digital light processing (DLP), and two/multi-photon polymerization (TPP/MPP), 3D printing can be used for the direct fabrication of MNAs using a variety of printable materials (Lee et al., 2017; Rahmani Dabbagh et al., 2022; Shahrubudin et al., 2019; Yigci et al., 2022) such as hydrogels, acrylates, epoxides, polyamides, polyurethane (PU), polylactic acid (PLA), acrylonitrile butadiene styrene (ABS), and also bioinks with the ability to encapsulate cells.

Artificial intelligence (AI), in which the machines are taught to simulate human intelligence and propose solutions to an issue or predict the outcome of a process by analyzing a series of input data, is gradually influencing healthcare systems and biomedical applications (Alsuliman et al., 2020; Esteva et al., 2019; Rezapour Sarabi et al., 2021; Misagh Rezapour Sarabi et al., 2022; Yu et al., 2018),

such as disease prediction (Chen et al., 2017; Tasoglu, 2022), diagnosing cancer (Liao et al., 2018; Osareh & Shadgar, 2010), and medical imaging using AI (Ranschaert et al., 2019). Machine learning (ML) is a branch of AI which is utilized to detect patterns and relations in data using algorithms intended to make accurate predictions (Mohri et al., 2018). Deep learning (DL) is also part of the ML family based on artificial neural networks with representation learning. ML techniques are available in four major categories: supervised, semi-supervised, unsupervised, and reinforced (Bonaccorso, 2017). ML is a prominent tool to understand the effect of different 3D printing parameters on the final product (Goh et al., 2021). For example, ML was used for 3D-printability analysis in order to detect possible errors in the design (Shi et al., 2018), tuning microstructure to obtain desired mechanical properties (Gan et al., 2019), optimizing the energy expenditure in the 3D printing process (Garg et al., 2016), designing 3D printed surrogates that imitate the implementation of a target setup (Sarlo & Tarazaga, 2016), maximizing adhesion of 3D printed biomimetic microfibrillar adhesives by optimizing their designs (Son et al., 2021), and prediction of drug-releasing process from 3D printed medicines (Muñiz Castro et al., 2021). In this regard, AI techniques can also be trained with the geometrical details of MNs and their 3D printing process parameters for predicting and tuning the desired product; a realm not explored by the research teams so far.

In this study, we fabricated biodegradable PLA MNs utilizing FDM 3D printing (**Figure 4.1A-B**). The 3D-printed MNAs were then etched using potassium hydroxide (KOH) solution to enhance their geometrical features (**Figure 4.1C-D**). By causing variations in geometrical features (base diameter, height and drafting angle of MNs) and etching dose (etching solution concentration and etching duration), the studied cases included 240 arrays with 2400 MNs. To the best of authors knowledge, this is the first study presenting implementation of ML into the optimization of MN fabrication. In this regard, the dataset of the 2400

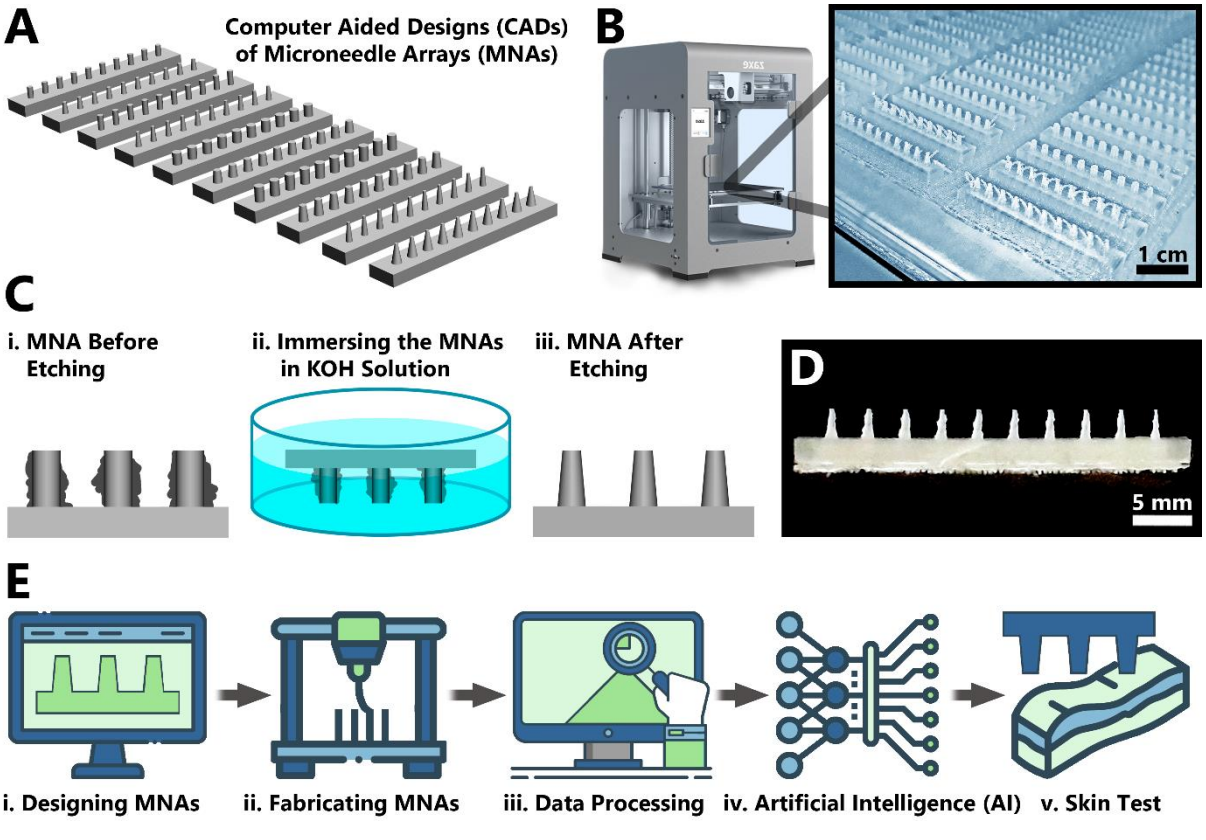

Fig 4.1. Fabrication of MNAs using 3D printing and features enhancement using chemical etching. (A) Ten different geometries of MNs were drawn using CAD, featuring various needle base diameters, needle heights, and draft angle (Table 1). (B) The MNAs were fabricated with FDM 3D printing technology using biodegradable PLA. (C) Since the printed needles had some imperfections (i), they were etched using KOH solution (ii), in order to remove the extra parts and thinner the needle bodies (iii). (D) An example final MNA featuring a designed based diameter and height of 1000 μm and 2500 μm, respectively, and draft angle of 5°, etched in a 5 M KOH solution for 18 h (case 4 in Table 1). The measured average base diameter and height of the needles for this case were ~952 μm and ~2494 μm, respectively. (E) The general workflow of the present study: After (i) designing the MNAs, and (ii) fabricating them using 3D printing followed by etching, (iii) their geometrical specifications and etching parameters processed using AI methods (iv) in order to predict the outcome of new prints, followed by (v) testing the fabricated MNAs for their skin perforation capability.

MNs was utilized for optimization and prediction of 3D-printed MNAs using AI methods. DL was trained with this dataset for quality control and anomaly detection in the fabricated MNAs. Next, using ML, the data was processed to extract similarity metrics between the designed MNAs and fabricated MNAs. The roles of geometrical specifications, and etching parameters were investigated using ML to predict the outcome of new prints when the mentioned criteria were altered (**Figure 4.1E**). Finally, the capability of the fabricated PLA MNAs' insertion into the skin along with drug delivery capability were investigated. Integration of the two emerging sciences of MNs with AI will pave the way for easier development of advanced healthcare setups.

4.2. Methods

4.2.1. Designing and 3D Printing of the MNAs

The MNAs were designed with Dassault Systèmes (3DS) SolidWorks computer-aided design (CAD) and computer-aided engineering (CAE) software. The shape of the MNAs included ten different designs, by varying the parameters of: the needle base diameter, the needle height, and the angle of the draft (**Table 4.1**). The arrays were designed with one row comprised of 10 MNs. The MNAs were fabricated with FDM technology by Zaxe Z1 3D Printer (Zaxe 3D Printing Technologies, Istanbul, Türkiye) using biodegradable PLA filament purchased from the same company. The layer height of the 3D printer was set to 0.06 mm. The filling density parameter of the 3D printer was not applicable in the prints as the MNAs are smaller than to be filled (e.g., they are composed of only layer walls).

4.2.2. Preparing KOH Solution and Performing Etching Experiment

KOH in the form of flakes with 90% purity (Sabunsu, Antalya, Türkiye) was added to distilled water to result the KOH solution. Four solutions with various concentrations (3, 4, 5, and 6 M) were prepared. The 3D printed MNs (made from PLA) were completely immersed in the prepared KOH solutions for six various durations (4, 7, 14, 18, 21, and 24 h) followed by several washes with water to remove the KOH solution.

4.2.3. Image-Based Classification and Defect Detection Using DL

Photo of the each MNA was captured with a digital camera, resulting in 240 images of the fabricated MNAs (**Figure 4.2A**) to be fed to the DL. Python programming language was used in the DL technique. Each MNA, which was composed of ten needles, was divided into single MN photos with size of 150 × 150

Table 4.1. Geometrical parameters (needle base diameter, needle height, and draft angle) used to design various shapes of MNs, manufactured by 3D printing, followed by etching experiment with the presented criteria.

#	Schematics	Designed Needle Base Diameter (μm)	Designed Needle Height (μm)	Designed Draft Angle (deg)	Etching Solution Concentrations (M)	Etching Durations (h)
1		1000	2000	0	3; 4; 5; 6	4; 7; 14; 18; 21; 24
2	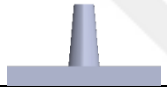	1000	2000	5	3; 4; 5; 6	4; 7; 14; 18; 21; 24
3	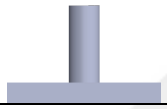	1000	2500	0	3; 4; 5; 6	4; 7; 14; 18; 21; 24
4		1000	2500	5	3; 4; 5; 6	4; 7; 14; 18; 21; 24
5	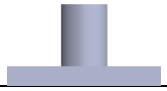	1500	2000	0	3; 4; 5; 6	4; 7; 14; 18; 21; 24
6	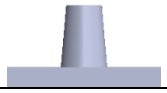	1500	2000	5	3; 4; 5; 6	4; 7; 14; 18; 21; 24
7	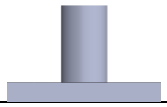	1500	2500	0	3; 4; 5; 6	4; 7; 14; 18; 21; 24
8	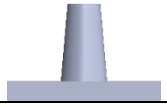	1500	2500	5	3; 4; 5; 6	4; 7; 14; 18; 21; 24
9	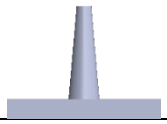	1000	3000	5	3; 4; 5; 6	4; 7; 14; 18; 21; 24
10	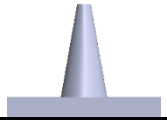	1500	3000	10	3; 4; 5; 6	4; 7; 14; 18; 21; 24

pixel, using an image-processing pipeline, creating a dataset with 2400 instances. Each instance of this dataset was labeled as "non-defective" or "defective" by expert review, resulting in 1004 non-defective and 1396 defective images, which were all then binarized and split for training (75%), validation (10%) and testing (15%). Three different methods, classical ML, DL, and, unsupervised anomaly detection, were implemented for classification. For classical ML, stochastic gradient descent (SGD), decision trees, naïve Bayes, multi-layer perceptron (MLP), and support vector machines (SVM) (**Table 4.2**) were used upon flattening 150 × 150 binarized image dataset to 1 × 22,500 feature vector followed by a principal component analysis (PCA) method for reducing the feature dimensions from 22,500 to 10 to avoid the curse of dimensionality. Each algorithm was run several times by randomly splitting the dataset and averaging the output scores.

Utilizing Python, three different image classification networks based on Convolutional Neural Networks (CNNs), Resnet34 (He et al., 2016) as the baseline, MobilnetV2 (Sandler et al., 2018) as the light network, and ConvNeXt_Base (Liu et al., 2022) as state-of-the-art network were used in this work (**Table 4.3**). These networks were implemented through PyTorch (Paszke et al., 2019) with transfer learning method by using pre-trained networks on ImageNet (Deng et al., 2009). Since ImageNet has 1000 classes, those networks' last layer contains 1000 dimensions. Therefore, we replaced every model's last fully connected layer to our sequential model, which composed of a 1024x128 linear layer, a dropout layer with 0.4 probability, followed by a 128 × 2 linear layer. SGD optimizer and binary cross entropy loss was used with 24 batch size and 0.001 learning rate to fine-tune the network on 20 batches. For the task of anomaly detection, Patch Distribution Modeling (PaDiM) algorithm (Defard et al., 2021) was applied (**Figure 4.2B**). PaDiM utilizes the pretrained CNN for patch embedding, and of multivariate Gaussian distributions to get a probabilistic rendering of the normal class. PaDiM uses only non-defective samples for testing in order to learn the distribution of normal images, followed by assigning anomaly scores to the images in the testing period. Only 450 non-defective MN images were used in training and the rest were used for testing.

Table 4.2. Performance of ML algorithms for image classification task.

#	Model	Precision	Recall	F-1 Score	Accuracy
1	SGD	0.75	0.75	0.75	0.75
2	Decision Trees	0.76	0.76	0.76	0.76
3	Naïve Bayes	0.83	0.82	0.82	0.82
4	MLP	0.84	0.84	0.84	0.84
5	SVM	0.87	0.86	0.86	0.86

Table 4.3. Performance of DL algorithms for image classification task.

#	Model	Precision	Recall	F-1 Score	Accuracy
1	Resnet34	0.93	0.92	0.92	0.92
2	MobilnetV2	0.94	0.93	0.93	0.93
3	ConvNeXt_Base	0.96	0.96	0.96	0.96

4.2.4. Extracting Similarity Indices Using Image Processing

For image processing, a total of 240 instances were used, represented by the different criteria of **Table 4.1**. Images of the fabricated MNAs were named as "3DP images". Additionally, to compare the original designs with the fabricated MNAs, side shot of each CAD was taken, resulting in 240 "CAD images". Each 3DP image was manually aligned to its corresponding CAD image using Adobe Photoshop, resulting in 240 3DP-CAD pairs. MathWorks MATLAB was utilized for processing each pair in the next step (**Figure 4.2C**). A MATLAB code was developed to convert the images into binary and compare their pixels, giving a set of true positives (TPs), true negatives (TNs), false positives (FPs) and false negatives (FNs). A pixel was considered to be "positive" if it belonged to a needle, otherwise it was considered to be "negative". On the other hand, pixels were considered as "true" if they had the same binary values in both images, otherwise they were considered as "false".

According to the confusion matrix of each image pair, five sets of metrics were calculated (**Table 4.4**). The first metric (Similarity Index) measured the similarity

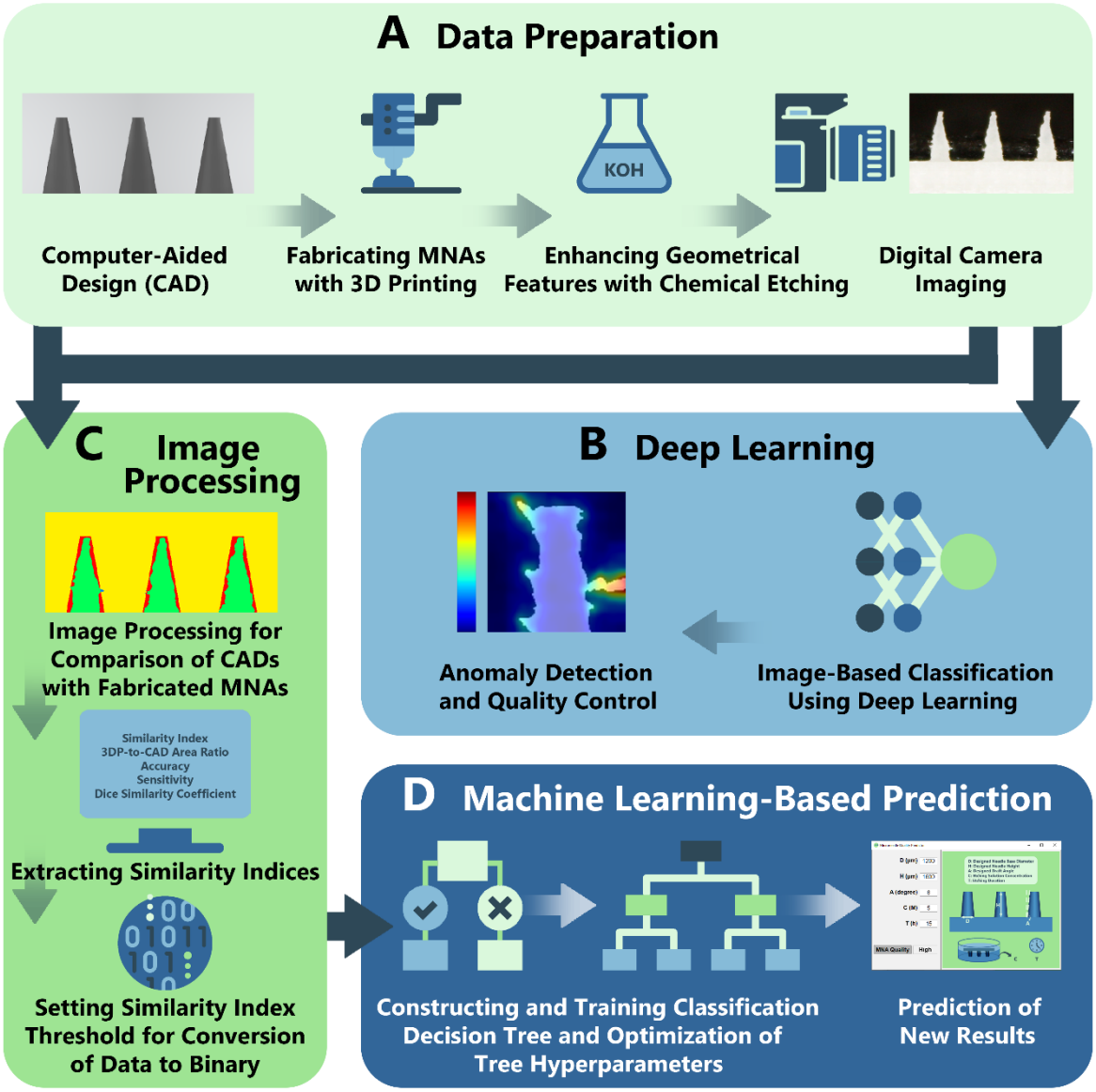

Fig 4.2. Workflow of preparing and processing data for AI models. (A) Based on design and fabrication criteria, a total of 240 MNA instances were possible. Each instance was imaged with a digital camera. (B) The captured MNA photos were automatically separated and binarized to a dataset of 2400 MN photos, which were analyzed for their quality and anomaly detection using DL. (C) For comparison of original designs and the fabricated MNAs, instances were processed for extraction of five different similarity metrics. ML models were developed by receiving five input parameters (three design features: base diameter, height and drafting angle of MNs; and two etching features: etching solution concentration and etching duration). (D) A classification tree was constructed to optimize the hyperparameters (maximum number of splits and split criterion), and then it was trained for classification. Finally, the trained model was used to predict the quality of the resulting MNA for the criteria defined by user.

error, calculated by dividing the sum of false pixels (FP and FN) by the area of the MN pixels in the CAD image, then subtracting that error from one. The second metric (3DP-to-CAD Area Ratio) calculated the ratio between the areas of MN pixels of the CAD image and 3DP image. Accuracy as the third metric measured the ratio between true pixels (both positive and negative) and all of the pixels in one image. The fourth metric (Sensitivity) calculated the ratio between the pixels that only represented MNs in both images (i.e., TP) and the area of the MN pixels in the CAD image. Finally, the Dice Similarity Coefficient was utilized to measure the ratio between intersection and union of the two images. i.e., the true positives over the MN pixels in both images.

Table 4.4. Performance of ML algorithms for the extracted similarity metrics.

#	Metric	Formula	Best Performing ML Model	R^2
1	Similarity Index	$\frac{TP - FP}{TP + FN}$	SVM (Cubic Kernel)	0.63
2	3DP-to-CAD Area Ratio	$\frac{TP + FP}{TP + FN}$	Gaussian Processes (Squared Exponential)	0.90
3	Accuracy	$\frac{TP + TN}{TP + TN + FP + FN}$	SVM (Cubic Kernel)	0.60
4	Sensitivity	$\frac{TP}{TP + FN}$	Gaussian Processes (Squared Exponential)	0.75
5	Dice Similarity Coefficient	$\frac{TP}{TP + FP + FN}$	Gaussian Processes (Squared Exponential)	0.55

4.2.5. Creating Training Library and Applying ML

MATLAB's Regression Learner and Regression Learner toolboxes were used for choosing and training the ML models. For the regression task, five folds were used for cross validation, where the data set was divided into five subsets, and the ML algorithm was trained five times. At each training round, one of the five subsets was considered as the validation set, while the rest data was used for training, resulting in five R^2 values, of which the mean was calculated as the reported R^2 value. All five features were used without any dimensionality reduction, which included three geometric features (height, base diameter and drafting angle of MN) and two etching features (solution concentration and etching duration).

A separate training session was applied for each single similarity metric by applying all available models in the toolbox including linear regression, neural networks, regression trees, support vectors machines, and Gaussian process regression, and choosing the one that resulted in the highest R^2 value. For classification, the sensitivity metric which ranges between 0 and 1 was chosen as the similarity index, and a threshold of 0.8 was set to convert the data into binary, where similarity indices below 0.8 were considered to be low (Class 0), otherwise they were considered as accepted similarities (Class 1). All available models in the MATLAB's Classification Learner toolbox were used, and five folds were used for cross validation. Since classification trees were found to yield the highest accuracies, a classification tree was constructed to optimize its hyperparameters, which are the maximum number of splits and split criterion, and then it was trained for classification (**Figure 4.2D**).

4.2.6. Skin Perforation Experiment on Porcine Skin Ex Vivo

Fresh porcine flank skin pieces were supplied from a local butcher's shop and were transferred with ice to the laboratory and were kept frozen in −20 °C refrigerator. On the experiment day, the skin was thawed at room temperature. Upon after, the skin was cut into pieces with appropriate sizes to be put on the device. The insertion of MNAs into the skin was performed using Instron ElectroPuls Model E10000 Axial Torsion Test System (Illinois Tool Works Inc., Glenview, IL, USA) in compression mode with precise measurement of the required force for the skin perforation. Custom holders were fabricated using 3D printing for placing the skin samples onto the shafts of the device. Data was collected every 20 ms. Furthermore, in order to keep the skin fresh and prevent its dehydration during experiment, skin samples were kept on paper tissues soaked with liquid Dulbecco's phosphate-buffered saline w/o calcium w/o magnesium (Biowest, Lakewood Ranch, FL, USA).

4.2.7. Preparing Rhodamine B (RhB) Solution and Its Delivery as a Drug Model

Food wheat starch (Tibet İthalat İhracat ve Kozmetik, Istanbul, Türkiye) in two values of 30 g and 15 g were added to two beakers with 75 mL distilled water. Both mixtures were put on a magnetic hot plate stirrer (Hangzhou Miu Instruments, Hangzhou, China) at 100 °C and 400 rpm stirring, for 24 min. The solution with 15 g starch was chosen as the model drug carrier. 0.075 g RhB (REF 1.07599.0025, Sigma Aldrich, St. Louis, MO, USA) as the model drug was added to the starch solution and was completely stirred to result a uniform solution. Tips of an example MNA (case 6 in **Table 4.1**, featuring a designed based diameter and height of 1500 μm and 2000 μm, respectively, and draft angle of 5°, etched in a 5 M KOH solution for 14 h) were coated with the prepared solution and were inserted into the porcine skin with hand. In order to keep the skin fresh and

prevent its dehydration during experiment, skin sample was kept on paper tissues soaked with liquid Dulbecco's phosphate-buffered saline w/o calcium w/o magnesium (Biowest, Lakewood Ranch, FL, USA). After removing the MNA from the skin, the perforation site was imaged under visible light, and under ultraviolet (UV) light (OmniCure S2000, Excelitas Technologies, Waltham, MA, USA).

4.3. Results and Discussion

4.3.1. Role of Design Parameters and Etching Doses

The MNAs were designed in ten different shapes with altering the needle base diameter, the needle height, and the angle of the draft (**Table 4.1**, **Figure 4.1A**). MNAs were 3D-printed with PLA, a biodegradable thermoplastic polyester. The utilized 3D printer for the fabrication process, was a desktop FDM model (**Figure 4.1B**). While being cost-efficient, accessible, and easy-to-use, the 3D printer has some resolution limitations in printing tiny features such as MNs. The device showed better capability in printing cylindrical shaped MNs (with a draft angle of zero) in comparison with conical shaped MNs (with the designed draft angle of 5° or 10°). However, in all cases, the nozzle of the printer left material traces between the needles which created some imperfections in the arrays (**Figure 4.1(C,i)**). In order to eliminate these imperfections, KOH solutions with various concentrations (3, 4, 5, and 6 M) and various exposure durations (4, 7, 14, 18, 21, and 24 h) were used for etching the 3D-printed PLA MNs (**Figure 4.1(C,ii)**). The etching process resulted in elimination of the mentioned imperfections and enhanced the geometrical features (**Figure 4.1(C,iii)**), in accordance with previous reports of fabrication of MNs using 3D printing followed by etching to reach ideal size/shape (Camović et al., 2019; Luzuriaga et al., 2018).

In addition, as the concentration of the KOH solution was increased, the etching process demonstrated better enhancement of the MNA features. Also, exposure duration exhibited a similar result, in which longer duration resulted in more removal of the flaws. However, the strongest KOH exposure (e.g., 6 M concentration for 24 h duration) resulted in making the high-aspect ratio MNAs (e.g., cases 9 and 10 in **Table 4.1**) more brittle, as the process removed some of the needle bodies as well. In general, mild conditions of etching exposure were helpful to achieve more perfect products similar to the initial CAD design. For example, the MNA featuring a designed based diameter and height of 1000 μm and 2500 μm, respectively, and draft angle of 5° (case 4 in **Table 4.1**), etched in a 5 M KOH solution for 18 h, resulted in the measured average base diameter and height of ~952 μm and ~2494 μm, respectively (**Figure 4.1D**). In total, by variation in geometrical features and etching dose, the studied cases included 240 arrays with 2400 MNs, in which they were analyzed using DL for detection of fabrication defects followed by training with ML in order to create a model to predict the outcome of new prints (**Figure 4.1E**).

4.3.2. Anomaly Detection Using DL

Defect detection plays an important role in autonomous production systems. DL models were utilized here to identify defective MNAs among 2400 fabricated MNs. The main task of anomaly detection algorithms is to identify abnormal images and localize abnormal areas. Most industries prefer unsupervised anomaly detection methods over supervised ones since not only collecting and labelling anomaly data is very expensive and time-consuming, but also supervised methods lack

generalization capabilities. First, classical ML was used with methods including SGD, Decision Trees, Naïve Bayes, MLP, and SVM (**Table 4.2**). After running the algorithms using python programming and open-source libraries such as Scikit-learn (Pedregosa et al., 2011), PyTorch (Paszke et al., 2019), and NumPy (Van Der Walt et al., 2011), the results were evaluated based on metrics such as precision, recall, F-1 score, and accuracy. The results indicated that the best performed algorithm was SVM with 0.86 accuracy followed by MLP and Naïve Bayes.

Upon fine-tuning pre-trained CNNs at approximately 15–20 epochs, the test set was classified by trained candidate CNNs (e.g., Resnet34, MobilnetV2, and ConvNeXt_Base), and the same performance metrics as ML methods were evaluated (**Table 4.3**). By comparison of results at **Tables 4.2** and **4.3**, it can be demonstrated that the CNNs outperformed ML methods. In addition, it can be observed that the best performance was for the state-of-the-art ConvNeXt_Base model with 0.96 accuracy, since it contains a complex deep network. Resnet34, considered as the core standard backbone classification network, also performed close to ConvNeXt_Base with 0.92 accuracy. On the other hand, MobilnetV2, which is a tiny network suitable for mobile devices, got slightly higher scores than Resnet34 with ten times less feature size. Despite the deep CNNs considered as black boxes, activations on layers are presented in **Figure 4.3A-B**, with activation maps visualized with the overall defect detection pipeline.

For anomaly detection, only 450 random images selected from non-defective images were used in training, while the others were reserved for testing. PaDiM used a pre-trained ResNet backbone to extract the features from images and learnt the distribution of non-defective images with a multivariate gaussian type of algorithm. Therefore, there was no training loop for this method, meaning that non-defective images were fed into the algorithm and the algorithm calculated the parameters at once. The Receiver Operating Characteristics-Area Under The Curve (ROC-AUC) score is a performance measurement for the classification problems. ROC-AUC score was used to evaluate the anomaly detection task, as it represents the PaDiM algorithm's classification capability better than other metrics. Upon testing, 0.919 image level ROC-AUC score have achieved by PaDiM algorithm. As PaDiM generates an anomaly score for each pixel, the anomaly maps pointing out abnormal areas defined by the algorithm were visualized (**Figure 4.3C**).

4.3.3. Image Processing and ML

For image processing, a total of 240 instances were used, represented by the different fabrication criteria mentioned before. Five similarity metrics (similarity index, 3DP-to-CAD area ratio, accuracy, sensitivity, and Dice similarity coefficient) were calculated from the results of image processing (**Table 4.4**). Among these metrics, 3DP-to-CAD area ratio yielded the highest R^2 value. This can be a result of representing only the increase or decrease of the 3D-printed MN in comparison with CAD due to overprinting or etching, respectively. Also, this metric does not have a specific upper bound and can exceed 1 in many cases. On the other hand, the other four metrics yielded R^2 values of no more than 0.75 with a minimum of 0.55, which do not indicate a good fitting of the models to the available data. The reason for having poor R^2 values can be explained by the fact that the dataset is relatively small. In addition, a considerable amount of noise seems to affect the data, initiating from different causes, such as the bridging

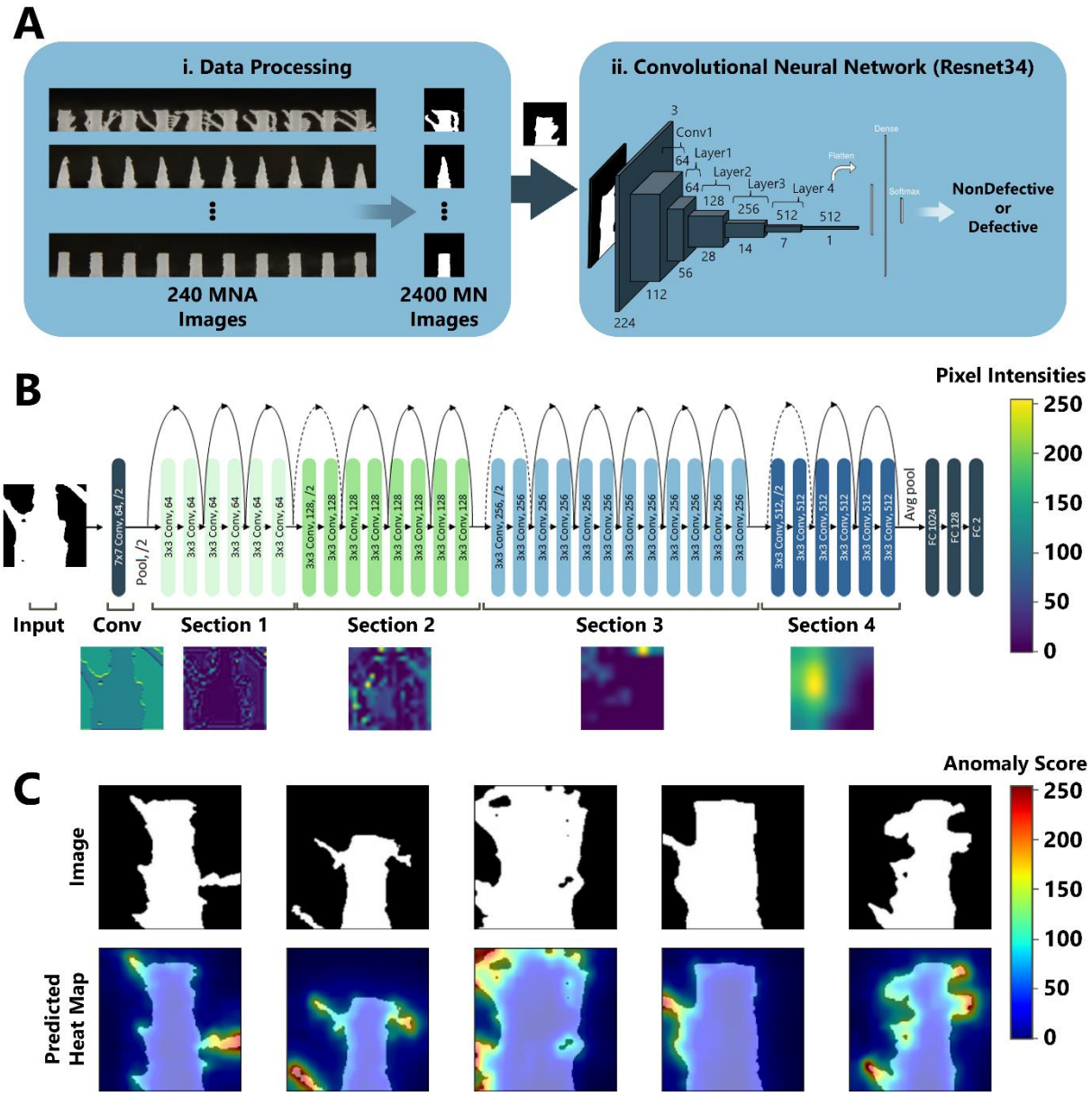

Fig 4.3. Image-based classification and anomaly detection using DL. (A) To use the MNA image dataset for the defect detection task, a data processing pipeline was implemented in which (i) each MNA image was automatically cut and binarized to separate individual MN images. Upon labeling all MNs as "Non-Defective" or "Defective" by expert review, the dataset was used for training CNN models. (ii) The resulting individual MN images were fed into Resnet34 CNN to be classified as "Non-Defective" or "Defective". (B) Visualization of Resnet34 layer activation, where four ResNet sections are utilized in the CNN. The defective areas get higher pixel intensities throughout the network. (C) DL-based anomaly detection using PaDiM. Individual MNs were first binarized (top row) and then were used as an input for the PaDiM algorithm to generate heat maps of the anomaly scores of the MNs (bottom row). Anomaly scores are represented by pixel intensities between 0 (e.g., no anomaly) and 255 (e.g., extreme anomaly).

between MNs during 3D printing, the heterogeneity of etched regions, and the damage caused to some MNs randomly during etching.

Sensitivity metric was therefore selected as the similarity index since it yielded the second best R^2. However, its R^2 of 0.75 was not high enough for an acceptable regression, and hence the data was converted to binary by setting a threshold of 0.8 to split the data into two classes. Optimizing the hyperparameters of a classification tree with the existing binary data resulted in a maximum number of splits of 20, while Gini's diversity index was found to be the optimal split criterion. The confusion matrix generated after applying classification (**Table 4.5**), indicated that 128 out of the 135 images with high quality and 98 out of the 105 images with low quality were classified correctly, leaving 14 misclassified images out of the whole images (seven false negatives and seven false positives). The confusion matrix also showed that classification improved the prediction of the ML model, with an accuracy of 94.17%, sensitivity of 94.81%, and specificity of 93.33%. However, the drawback of using classification is that the exact similarity between the designed and fabricated MN is not reported, but only the quality of fabrication is reported as high or low.

Table 4.5. Confusion matrix generated after binary classification.

		Predicted Class		
		0	1	
True Class	0	TN = 98	FP = 7	105
	1	FN = 7	TP = 128	135
		105	135	240

Figure 4.4 represents the results of processing the images. The colors illustrate the difference between true positives, true negatives, false positives, and false negatives (**Figure 4.4A**). Example results of image processing for one of the studied designs (Case 8 from **Table 4.1**) is shown in **Figure 4.4B–E**. It can be demonstrated that increasing the etching solution concentration or increasing the etching duration have similar effects of decreasing the false positives (i.e., excess printed material) and increasing the false negatives (i.e., missing printed material). To allow the final trained classification ML model to be efficiently used by users to predict 3D-printed MNAs quality, a graphical user interface (GUI) was designed using MATLAB's App Designer tool (**Figure 4.5A**). GUI aimed to enable users with no programming experience to utilize the ML model easily without having to write codes. The GUI included an illustration of an example MNA to explain the meaning of each of the five input parameters to the user. A text box with the name of each of these parameters was introduced, where users can enter the values at will. The trained and optimized classification tree model was integrated with the GUI to perform the prediction. After receiving the five input parameters, and upon the user clicking on the button "MNA Quality", the parameters are processed with the classification tree, calculating the predicted MNA quality and finally showing the predicted result next to the button as "High" or "Low". In addition, upper and lower ranges for each of the input parameters were introduced to the GUI. For example, etching solution concentration was limited to the range of 3 M to 21.6 M, as concentrations lower than 3M are not so efficient in etching, and 21.6 M is the maximum concentration of KOH in water

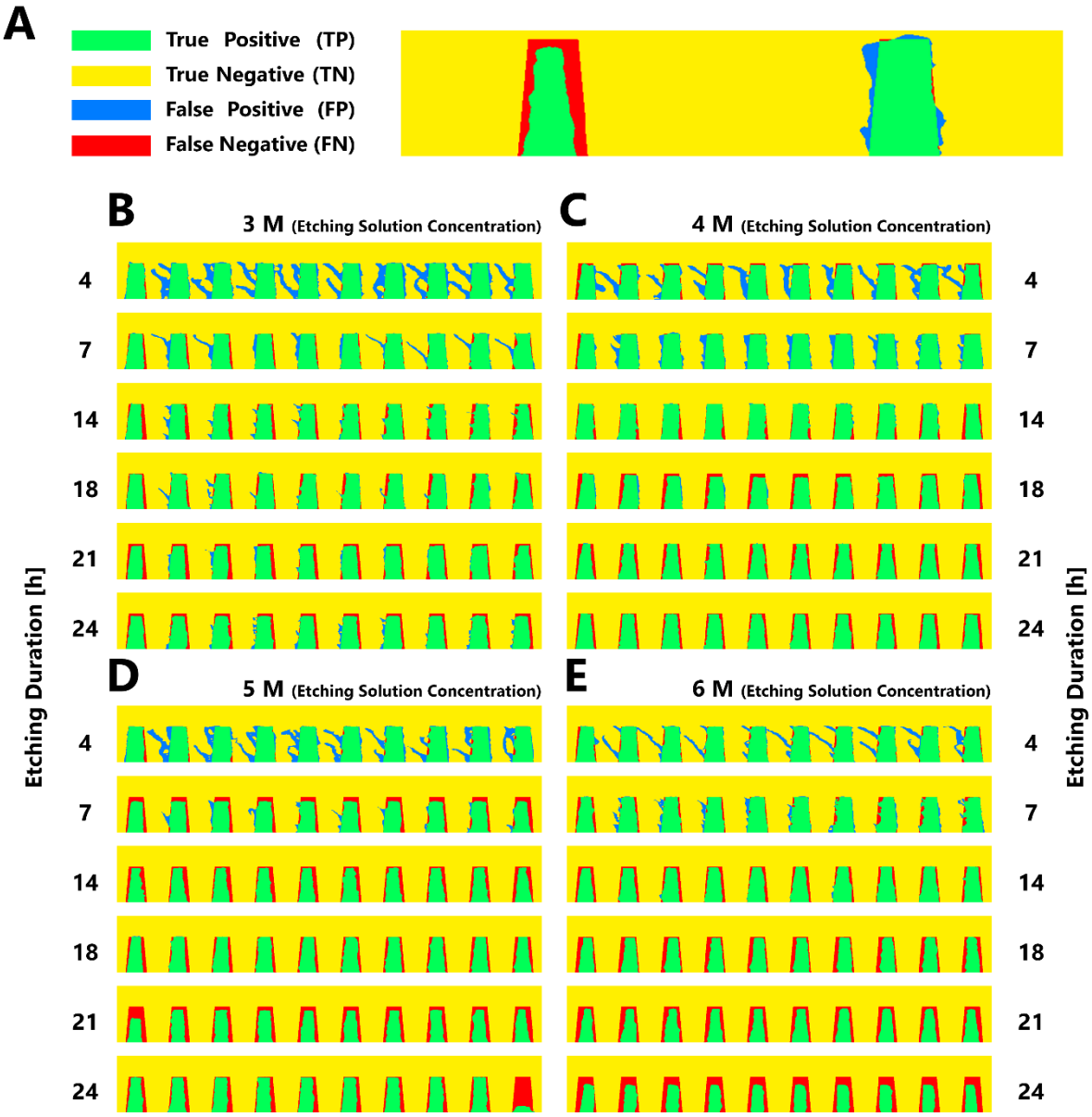

Fig 4.4. Image analysis procedure using MNA photos aligned with their corresponding CAD for purpose of extracting similarity indices. (A) Upon alignment of each experimental image to its corresponding CAD, a code was developed for extraction of several similarity metrics. The total instances which included 240 cases, were converted into binary and their pixels were compared, giving a set of TPs, TNs, FPs, and FNs. A pixel was considered to be "positive" if it belonged to a MN, otherwise it was considered to be "negative". Also, pixels were considered as "true" if they had the same binary values in both images, otherwise they were considered as "false". Example image analysis results for one of the studied designs (Case 8 from Table 1), exposed to KOH etching in four concentrations of (B) 3 M, (C) 4 M, (D) 5 M, and (E) 6 M, for six durations (4, 7, 14, 18, 21, and 24 h).

that can be prepared in 25 °C. Therefore, GUI would reject out-of-range values for the parameters.

4.3.4. Capability of MNAs for Perforation of Porcine Skin Ex Vivo

Human skin is composed of three layers. The outermost layer which is called the epidermis, a waterproof barrier and representative of the skin tone. The dermis, the second layer located under the epidermis, contains sweat glands, arrector pili muscles, hair follicles, and sebaceous glands (Dabbagh et al., 2021). The third layer which is called the hypodermis is the deeper subcutaneous tissue consisting of fat and connective tissues (Dabbagh et al., 2021). Since using human skin in experiments faces ethical issues and requires laboratory approval, polymeric films, paraffin wax, agarose gel, rat skin, and porcine skin have been reported in literature to be widely utilized instead for experiments simulating the human skin (Makvandi et al., 2021). Porcine skin is histologically similar to the human skin, and the thickness of porcine flank skin epidermis, 68 ± 26 μm, is also similar to the human skin epidermis thicknesses, 68 ± 26 μm in face, 65 ± 24 μm in neck, and 68 ± 21 μm in arms (Eggleston et al., 2000). Hence, it can be used as an alternative for human skin with an appropriate resemblance. In this regard, porcine flank skin was used in this study, and the capability of the fabricated PLA MNAs' insertion into the skin was investigated.

All ten alternative designs of **Table 4.1**, etched in 6 M KOH solution for 14 h, were tested for their skin penetration capability. Custom 3D-printed holders were fabricated for placing the skin samples and the MNAs on the device (**Figure 4.5B**). The MNA was bonded to the upper holder, and the porcine skin sample was positioned under the MNA on the lower holder (**Figure 4.5C**). The device moved these holders towards each other gently until the MNs were completely inside the skin. The required amount of force for perforation of the skin was measured precisely (**Figure 4.5D**). Among the designs with difference only in their drafting angle (e.g., cases 1 and 2, and cases 5 and 6), the results indicated that less force was required for insertion into the skin as the drafting angle increased. On the other hand, cases 3 and 7, which had zero drafting angle, were not able to perforate the skin sample and broke under the increasing force. The results can be interpreted from the point view of ratio of the needle height to the needle base diameter as well, an index similar to aspect ratio. As this ratio increased, less amount of force was required for penetration. For example, cases 1, 2, and 10 (with a ratio equal to 2) needed more effort for skin perforation in comparison with cases 4 and 9 (with ratios of 2.5 and 3, respectively). Furthermore, maximal static pushing force for humans was reported to be in the 583–1285 N range with both hands, and 262–520 N with their preferred hand (NASA, 1995). Hence, all of the MNAs discussed here, can be easily inserted by human hand as well.

4.3.5. Capability of MNAs for Model Drug Delivery into Porcine Skin Ex Vivo

In order to investigate the capability of the fabricated MNAs for delivery of a drug candidate into skin, tips of an example MNA (case 6 in **Table 4.1**, featuring a designed based diameter and height of 1500 μm and 2000 μm, respectively, and draft angle of 5°, etched in a 5 M KOH solution for 14 h) were coated with an aqueous solution of starch and RhB (**Figure 4.5E**). Previous reports have stated using thickener agents to facilitate deposition of the model drug onto the surface of the needle tips (Chen et al., 2015; Wu et al., 2021). Starch was chosen for this purpose in the current study, as it is highly available, cost-efficient, and a biodegradable option well-known in MN studies (Damiri et al., 2022). Starch solution was prepared with two amounts of 30 g and 15 g. The solution containing higher value of starch, behaved as a viscoelastic solid (e.g., highly viscous). Hence,

lower concentration of starch solution was chosen as it showed an appropriate viscosity for deposition on MNAs. The coated MNA was inserted into porcine skin ex vivo, with hand. Upon removing the MNA from the skin, the MNA perforation site was imaged under visible light (**Figure 4.5F**), and under UV light (**Figure 4.5G**). It can be observed that the RhB as a model drug was successfully delivered into the skin.

4.4. Outlook

DL and ML techniques with the capability of identifying patterns in the input information, administering multi-dimensional and multi-variety data, and predicting new outcomes coupled with incessant improvement are shaping the future of data analysis approaches. In order to enable users with no programming background to practically benefit from the developed codes using ML and DL techniques, translation of these codes into proper computer/mobile applications is the next step. This can empower the trained models to be more applicable for future research purposes. For example, developed DL-based quantification of clay minerals was integrated into an application for a better user experience

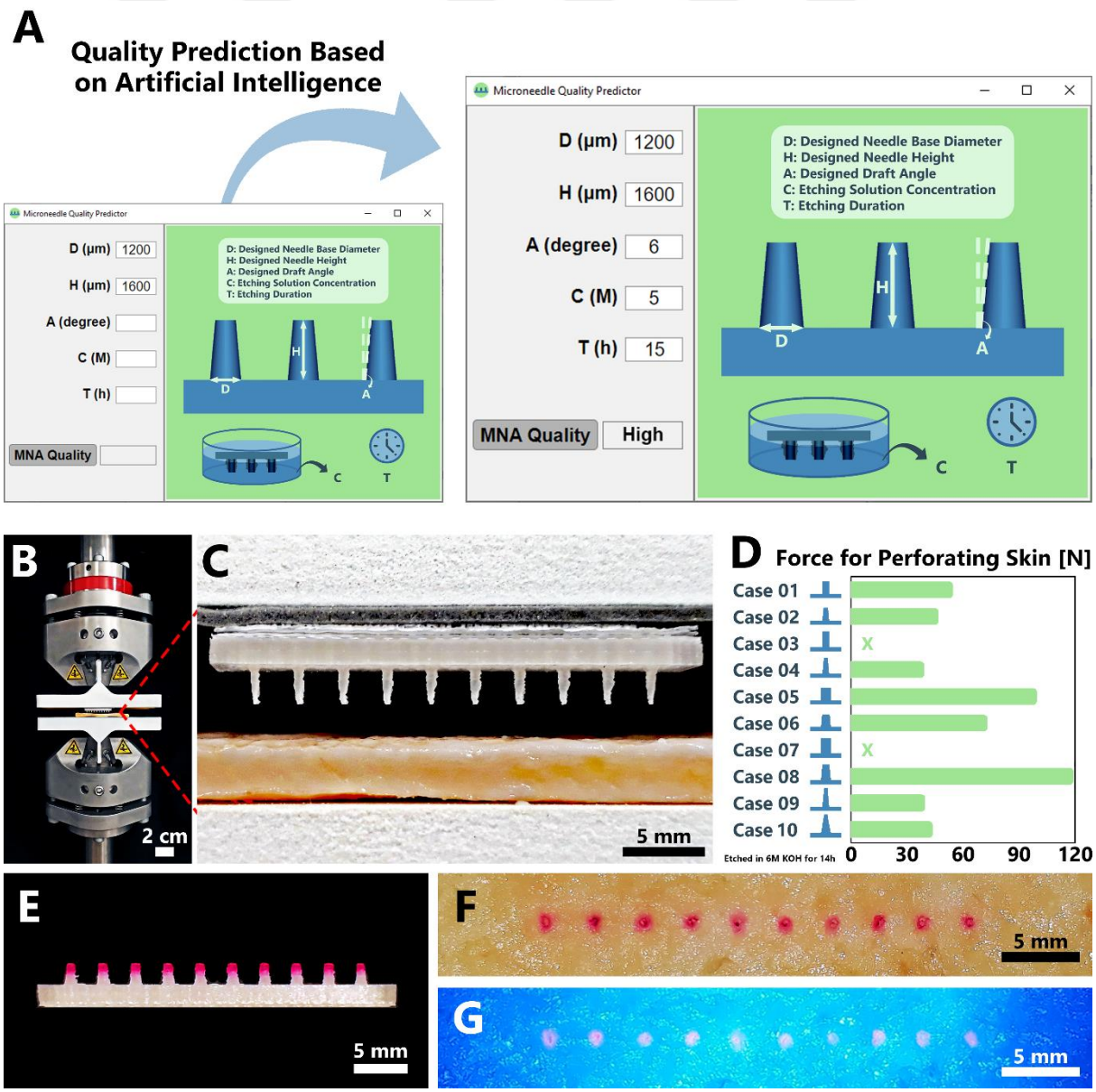

Fig 4.5. Developed GUI for MNA quality prediction, and capability of MNAs for perforation of porcine skin *ex vivo.* (A) A GUI was developed to predict the quality of the fabricated MNs based on the geometric and etching features input. The core of the GUI was based on the developed ML model, with addition of upper and lower limits for the input parameters (i.e., GUI rejects any input parameter that is out of its determined logical range). The user can enter the five parameters they intend to utilize for fabrications of MNAs, and upon clicking the button "MNA Quality", the predicted quality of the MNA will be displayed next to the button as "High" or "Low". (B) Using custom 3D-printed holders, (C) the skin sample was placed on the lower holder and the MNA was bonded to the upper holder. The device moved these holders towards each other until the MNs were inside the skin while (D) the required force [N] value for perforation of the skin was measured precisely for all of the geometrical specifications offered in Table 4.1. The MNAs used in this experiment were etched in 6 M KOH solution for 14 h. X: The MNA was not able to perforate the skin sample and broke under the increasing force. (E) In order to show the capability of the prepared MNAs for delivery of RhB as a model drug, tips of an example MNA (case 6 in Table 4.1, featuring a designed based diameter and height of 1500 μm and 2000 μm, respectively, and draft angle of 5°, etched in a 5 M KOH solution for 14 h) were coated with aqueous solution of starch and RhB mixture and were inserted into the porcine skin. The insertion and perforation sites are presented (F) under visible light, and (G) under UV light.

(Golsanami et al., 2022). For the case of MNAs, ML models can predict the quality of the needles even before designing, resulting in cost- and time- efficient procedures with observant usage of materials and resources. In this study, after we fabricated PLA MNs with FDM 3D printing, followed by chemical etching, we were able to achieve predictability in the design and fabrication procedure using ML models. It can be easily concluded that by using ML models, producing perfect MNAs can be planned in a faster way, which will eventually result in faster adaption with medical applications. We achieved the predictability code using five set of parameters here (base diameter, height and drafting angle of MNs, and etching solution concentration and etching duration), which was the base for the GUI for user-friendly implementation of the code. The investigated required force for penetration of MNAs into skin can be modeled using ML algorithms as well in order to predict the MNAs' capability for insertion into the skin, as a guide for future studies. In a nutshell, this study can come to an end stating that integration of AI science with MNs will pave the way for easier development of advanced healthcare systems.

Chapter 5: Long-Lasting Simultaneous Epidermal and Dermal Microneedle-Enabled Drug Delivery

Abstract: Different skin diseases, such as cancers, inflammatory conditions, and bacterial infections, manifest at distinct skin depths. Microneedle arrays, recognized for their painless and minimally invasive drug administration, can be customized to penetrate these layers simultaneously. Here, we engineer the design of the microneedles (MNs) in nonlinear ways with diverse needle heights on the array enabling concurrent drug delivery to various skin layers. Additionally, varying the base diameter of the needles in the array facilitates prolonged or intermittent drug release, depending on the biodegradation kinetics of these needles. MNs, microfabricated with a biocompatible and biodegradable polymer, are validated by skin administration. The nonlinear design of the MNs on the array introduces a novel perspective on addressing skin diseases at varying depths of the skin.

5.1. Introduction

Skin diseases including (i) skin cancers, such as Melanoma, Basal cell carcinoma, and Squamous cell carcinoma, (ii) skin inflammatory diseases, such as psoriasis, and (iii) bacterial infections, such as ecthyma, impetigo, erysipelas, and cellulitis, can involve different layers of skin, e.g., epidermis, dermis, and hypodermis, and hence manifest at varying depths of the skin (Crisan et al., 2023; Sukhov et al., 2016; Wen et al., 2022; Xie et al., 2021; Yosipovitch et al., 2014). The integumentary system, comprising the skin, represents the largest organ in the human body. This expansive anatomical domain offers a considerable expanse for the manifestation and progression of skin disorders. Persistent skin diseases and chronic conditions, such as psoriasis and eczema, contribute significantly to morbidity, causing physical discomfort and diminishing the overall quality of life for affected individuals. On the other hand, malignant diseases, such as Melanoma, are highlighted by the mortality that they cause. Advancements achieved in the field over recent decades have enabled the potential cure and treatment of the majority of skin diseases, provided that patients receive suitable therapeutic treatments. Effective treatment options encompass the prescription of pertinent pharmacological agents, adherence to precise dosage regimens, adherence to optimal therapy durations, and the accurate targeting of treatment efforts to the specific disease site. By targeting the skin layers simultaneously, treatment procedure can be enhanced. Additionally, intermittent drug delivery, which can enable facilitation of multi-burst releases of the drug (Chen et al., 2023; Tran et al., 2023), can be engineered as well to further improve treatment of skin diseases.

Microneedle arrays (MNAs) have garnered significant attention in the field of drug delivery due to their remarkable attributes, notably painless and minimally invasive administration (DeMuth et al., 2013; W. Li et al., 2019; Sullivan et al., 2010). Additionally, while traditional needles are typically constructed from stainless steel, MNAs present the flexibility of being manufactured from diverse materials, including polymers and inorganic materials, featuring a range of geometries, diverse heights, diameters, and needle configurations (Ahmadpour et

al., 2023). Furthermore, depending on the intended use of MNAs, they can be designed in solid, coated, hollow, or biodegradable/dissolvable variations. All these characteristics together, have established MNAs as leaders of novel drug delivery approaches. An example of this engineering in MNAs, was a geometry that included a microneedle (MN) shell, a MN cap, and a drug core, which enabled single-administration delivery with delayed burst release that simulated multiple bolus injections over a long period of time (Tran et al., 2021). Another research reported a biodegradable millirobot with a multi-legged MNA which could be programmed for the adaptive release of two different drugs, one loaded in the multi-legged array and the other drug loaded in nanofiber-constructed membrane body, by responding to variations in acidic physiological concentrations (Tan et al., 2022). With all these advancements, however, simultaneous, and multi-burst drug delivery to different skin layers is a realm that has not yet been explored so far.

In our work here, we propose novel MN designs, which involves deliberate nonlinearity in the arrangement of these microstructures, coupled with a range of meticulously customized needle heights or needle base diameters. These designs are introduced as the "Mountain Design" with varying heights on the array and the "Wave Design" with varying diameters of the needle bases on the array. The tailored Mountain Design affords the capability to target multiple layers of the skin during a single administration—an achievement hitherto unattainable with conventional methodologies. Whether the objective is to transport therapeutic agents to the epidermal layer or to access the deeper dermal layers for the treatment of complex skin conditions, the nonlinear MNAs offer unparalleled versatility. By customizing the needle diameters in the Wave Design on the other hand, control can be exerted over whether the drug is dispensed gradually over an extended period or administered intermittently. Also, exhibiting biocompatibility and biodegradability, the proposed MNAs ensure their suitability and sustainability in healthcare applications. It is anticipated that nonlinear MNAs can shape the new future where personalized and precisely controlled drug delivery redefines the landscape of skincare and dermatology, offering promising solutions tailored to the individual needs of patients.

5.2. Methods

5.2.1. Design

The master molds of the MNAs were designed with Dassault Systèmes (3DS) SolidWorks computer-aided design (CAD) and computer-aided engineering (CAE). The designs included two variations for nonlinear MNAs named as the (i) mountain design, and the (ii) wave design. The mountain design included a 9×9 organization of the needles on the array with the heights designed to gradually increase from sides to the center, and with the needle base diameter of 300 μm. The heights of the needles were designed to be 400 μm (for the first, second, eighth, and ninth rows of the needles), 800 μm (for the third and seventh rows of the needles), 1000 μm (for the fourth and sixth rows of the needles), and 1200 μm (for the fifth row of the needles, e.g., the central needle). The wave design included a 10×10 organization of the needles on the array with the height of 800 μm, and needle diameters of 150 μm and 300 μm, designed as one in between, e.g., the needles of the first, third, fifth, seventh, and ninth rows had a diameter of 300 μm,

and the needles of the second, fourth, sixth, eighth, and tenth rows had diameter of 150 μm.

5.2.2. Simulation

Both the mountain design and the wave design were examined through Finite Element Analysis (Explicit Dynamics Tool, ANSYS Workbench 2021 R1). Human skin was modeled with the density of 1.2 g/cm^3, Young's modulus of 7.33 MPa, Poisson's ratio of 0.49, with the assumption of linear elastic behavior, based on the information derived from the literature that reported mechanical properties of human skin *in vivo* (Agache et al., 1980; C. Li et al., 2012). Polyvinyl alcohol (PVA) was used as MN material with Young's modulus of 707.9 MPa, 0.44 Poisson's ratio, and the density of 1.19 g/cm^3, as stated in the information sheet of Sigma-Aldrich PVA 363170; the grade which later was planned to be used in the fabrication process. Meshing was performed in linear element order with the element size of 0.6 mm for both mountain and wave designs of the nonlinear MNs. Separate body sizing was applied to obtain finer mesh in the skin with the element sizes of with 0.1 mm for the skin for both models. There were 1886461 elements in mountain design, and 1497769 elements in wave design. Velocities for the MNs were given 1.2×10^8 $\mu m/s$ as the initial condition, optimized based on information from literature (S.B.V.J & Mannayee, 2022). Analysis end time was set as 10^{-5} s in order to obtain the displacement and proper penetration. Analysis was carried out to obtain stress, deformation, and strain results on both MNAs and the skin due to the penetration process and the interactions between the needles and the skin models.

5.2.3. 3D Printing of Master Molds

Master molds were 3D-printed using stereolithography (SLA) technology. Pr 110-385 3D printer (CADworks3D, Toronto, Ontario, Canada) and Master Mold Resin (Product Number: CW3D-R-MMG, CADworks3D, Toronto, Ontario, Canada) were used for this purpose. Layer thickness was set to be 30 μm, with curing exposure time of 3.5 sec. After the completion of the 3D printing process, the 3D printed master mold was removed from the tank and was rinsed and then submerged within isopropyl alcohol. Then the master mold was put in the sonication device for 10 min to remove any additional resin. Upon after, the master mold was cured with ultraviolet (UV) light for 40 min with top exposure followed by 20 min exposure from bottom.

5.2.4. Fabrication of PDMS Molds

Polydimethylsiloxane (PDMS) fabrication molds were prepared by pouring PDMS (SYLGARD 184 Silicone Elastomer Kit, Dow, Midland, Michigan, USA) and its curing agent 10:1 w/w onto the 3D-printed master molds. After curing the PDMS on a hotplate for 40 min, they were separated from the master molds.

5.2.5. PVA Solution Preparation

3 g PVA (Product Number: 363170, 87-89% hydrolyzed, average MW 13,000-23,000, Sigma-Aldrich, St. Louis, Missouri, USA) and 10 mL distilled water were added to a beaker and the beaker was placed on a hotplate magnetic stirrer. With the temperature set to 90°C, the solution was constantly mixed at 500 rpm for 3 h until it was homogenized. For visualization purposes, two different dyes (Rhodamine B; RhB, 1.07599.0025, Sigma-Aldrich, St. Louis, Missouri, USA and

Blue Dye, Epredia Mark-It Tissue Marking Dyes Kit, Thermo Fisher Scientific, Waltham, Massachusetts, USA) were separately introduced to the solution. Preparation was in similar manner with only difference that in the first step, the dye was added to the PVA solution.

5.2.6. Fabricating the MNAs

50±1 mg of the homogenized PVA solution was added to the PDMS mold. The mold was centrifuged at 3500 rpm for 30 min. Excess solution was removed via spatula. The mold was again centrifuged at 3500 rpm for an additional 30 min. Finally, it was left in room temperature to dry overnight. Upon after, the MNAs were removed from the mold. For preparation of the dual drug loaded mountain design MNA, all steps were the same except for using less intensity for centrifugation (3000 rpm for 14 min), and manual loading of dyed PVA solution to sides and center with different dye colors.

5.2.7. Fabricating Artificial Skin

In order to prepare a solution resembling human skin, 12 g wheat starch (Tibet Import, Export and Cosmetics Co., Kurtköy, Istanbul, Türkiye) was mixed with a 40 mL buffer solution of Potassium Hydrogen Phthalate and Sodium Hydroxide (Sigma-Aldrich, St. Louis, Missouri, USA). The mixture was placed on a magnetic heater and stirrer with a magnetic fish stirrer inside. A temperature of 100 °C and stirring at speed of 400 rpm was applied for 15 mins. Then the temperature was increased to 140 °C and stirring speed was increased to 600 rpm for another 15 mins, until the solution was in a gel shape. The mixture was left to cool down overnight with a half cover over the lid to avoid sudden dehydration. The result offered a gel environment similar to human skin with a pH similar to human skin (~pH=5) as well.

5.2.8. Implementation of the MNA on the Artificial Skin

The MNAs were inserted into the developed artificial human skin by hand, and then within several time intervals, they were removed and rinsed with ethanol to wash any artificial skin residue on the needles. Optical microscopic photos of the MNAs after insertion were taken. In these photos, size reduction of the needles for each geometry of the MNAs was inspected in Adobe Photoshop using Ruler Tool.

5.2.9. Preparation of Gel Environment & Visual Characterization of MNAs

Bovine-derived gelatin (Dr. Oetker, Bielefeld, Germany) was used to prepare an optically transparent environment for insertion of MNAs prepared with RhB. Within several time intervals, optical microscopic photos of the MNAs were taken. The insertion site on the prepared gelatin was colored with different colors of dyes (Epredia Mark-It Tissue Marking Dyes Kit, Thermo Fisher Scientific, Waltham, Massachusetts, USA) for visualization purposes. Then, optical microscopic photos of the insertion sites were taken. A custom holder for the gel in the shape of semicircle was fabricated using FDM 3D printing (Zaxe Z3, Z Eksen Baskı Sistemleri ve Bilgi Teknolojileri San. ve Tic. A.Ş., Istanbul, Turkey) followed by attaching a glass side to its side for visualization capability. The setup was used for observation of MNA degradation using optical microscope.

5.2.10. MNA Implementation on Skin and Skin Histology

Human arm skin was obtained from surgery section of Koç University Hospital and stored at −80 ℃ until experiment day. After thawing and warming up to room temperature and removing subcutaneous fat, skin was stretched onto a board using pins to mimic the tension of human skin in vivo. During the whole process, phosphate-buffered saline (PBS; Sigma-Aldrich, St. Louis, Missouri, USA) was constantly used on the skin samples in order to keep them dehydrated. MNAs were inserted into the skin manually. The skin samples were preserved in 10% formaldehyde prior to histology. For histology microscopy, the samples were immersed in a paraffin block and then sectioned into thin slices using a cryostat. Histological sections were surface-stained with hematoxylin and eosin (H&E) and examined by bright-field microscopy.

5.3. Results and Discussion

5.3.1. Nonlinear Design of the MNAs

Nonlinear arrangement of MNs on the array with customized needle heights or needle base diameters resulted in two alternatives entitled as (i) mountain design and (ii) wave design. As shown in **Figure 5.1**, mountain design facilitates simultaneous drug delivery to different layers of the skin, e.g., epidermis, derms, and, hypodermis, due to the diverse heights of the needles. Additionally, the array's needles with varying base diameters in wave design support prolonged or multi-burst drug delivery, exploiting differences in the biodegradation kinetics of these needles, since needles with smaller diameter and consequently less volume would degrade in a shorter time in comparison with needles with higher volume due to their larger base diameter. As a result, nonlinear design of MNs on the array propound a new insight into the treatment of skin diseases at different depths of skin.

5.3.2. Simulation of Interaction of MNAs with Human Skin Model

Finite Element Analysis was carried out to obtain the interaction behavior results on both MNAs and the human skin model due to the insertion process (**Figure 5.2A-D**). Equivalent (Von Mises) stress, strain, and the total deformation were examined through simulations for both mountain and wave design of the MNAs inserted into the skin. As first result of the analysis, nevertheless the analysis termination times were set the same, penetration of the wave MNA was completed in a shorter time and converged in the 14th step, while mountain MNA simulation completed in the 21st step, by the Program Controlled analysis settings. The mountain MNA caused a maximum skin deformation of 1.202 *mm* (**Figure 5.2E**), concentrated at the middle part, while the wave MNA induced a maximum deformation of 0.65 *mm* (**Figure 5.2F**). The simulation results revealed that the mountain MNA leads to higher skin deformation compared to the wave MNA, a logical outcome considering the taller needles in the former. More importantly, the deformation rates exhibited a smooth, consistent trend without sudden peaks, indicating that nonlinearity in needle designs are feasible, applicable, and practical without implying material or skin failure. In addition, equivalent elastic strain is useful in terms of combining shear and normal strains in complex stress states and provides a simplified measure of the total deformation energy stored in the material. Analysis results demonstrated that the interaction of mountain design caused a higher value of strain on the needles when compared to the wave

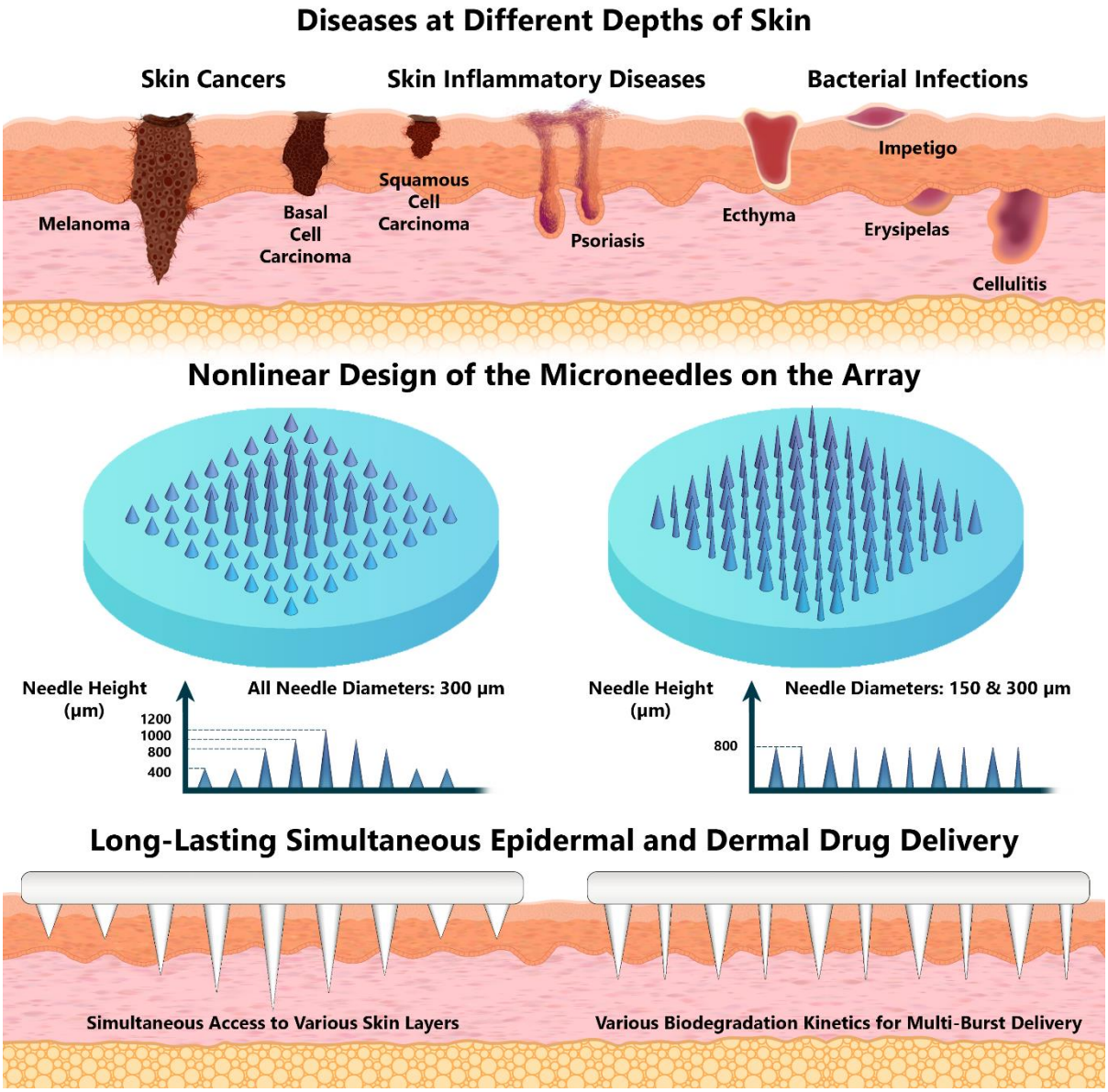

Fig 5.1. Various types of skin diseases, including cancers, inflammatory diseases, and bacterial infections, happen at different layers of skin. Microneedle arrays (MNAs), well-known for painless minimally invasive drug delivery, can be engineered to access these layers at the same time. Various heights of needles on the array enables simultaneous drug delivery to different skin layers, along with various base diameter of needles on the array that enables long-lasting or multi-burst drug delivery based on differentiation on biodegradation kinetics of these needles. Nonlinear design of MNs on the array hence enables a new insight into the treatment of skin diseases at different depths of skin.

design (**Figure 5.2G-H**). Also, maximum equivalent stress on the skin was found to be 8.78 *MPa* for the mountain MNA (**Figure 5.2I**) and 8.68 *MPa* for the wave MNA (**Figure 5.2J**) which implies slightly higher effort was required to administrate the mountain design into skin. The simulation results in a nutshell elucidated feasibility of the designs for fabrication and application.

5.3.3. Fabrication and Characterization of the MNAs

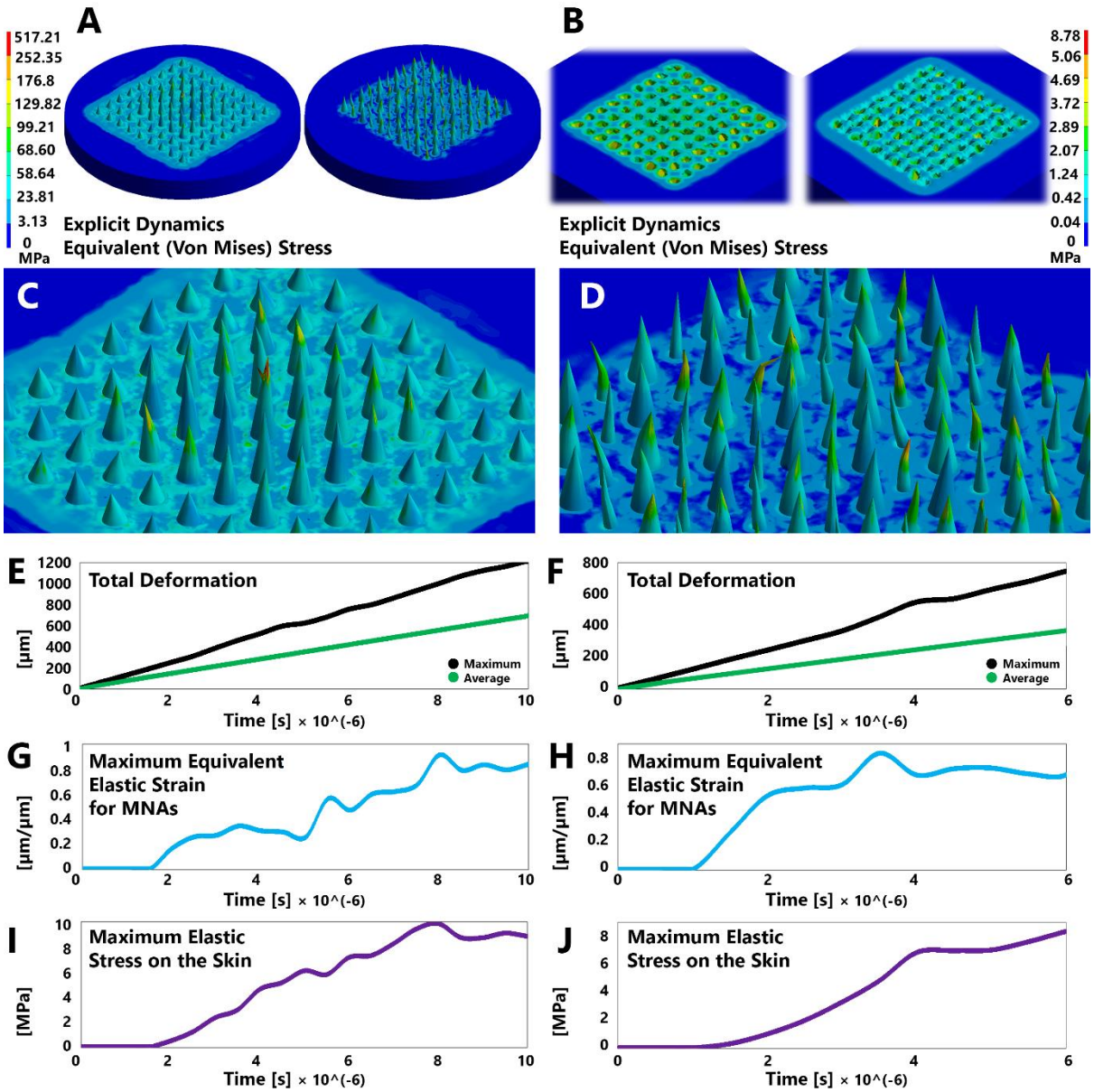

Fig 5.2. Simulation results for the MN penetration into the skin. (A) Experienced stress maps for the MNAs, with the mountain design on the left and the wave design on the right; both in time scale of 1e-5 s with the deformation scale of X2. Color bar unit: MPa. (B) Experienced stress maps for the skin, with administrated mountain design on the left and administrated wave design on the right; both in time scale of 1e-5 s with the deformation scale of X2. Color bar unit: MPa. (C, D) Closeup views of the deformation of the needles on the arrays in the stress map. (E, F) Maximum and average total deformations on the skin caused by the MNA insertion. (G, H) Maximum equivalent elastic strain for MNAs. (J, K) Maximum elastic stresses on the skin caused by the MNA insertion. C, E, G, I correspond to mountain design MNA, and D, F, H, J correspond to wave design MNA.

In order to fabricate the proposed MNAs, a combination of 3D printing and micro molding was carried out based on previously reported protocols (Ghanbariamin et al., 2023; Nejad et al., 2018b; Ziesmer et al., 2021). The procedure in which includes 3D printing of the master molds (**Figure 5.3A-B**), and production of

PDMS fabrication molds (**Figure 5.3C**), and then micro molding of the MNAs (**Figure 5.3D-F**), results in a highly repeatable, cleanroom-free, low-cost simple method for the fabrication of MNAs with high precision (**Figure 5.3G-H** and **Supplementary Figure 5.S.1**). PVA, a water-soluble synthetic polymer, was used as the material for MNAs. Offering biocompatibility and biodegradability, drug (or dye) can be easily encapsulated in the MN tips by direct addition to the PVA solution (Ziesmer et al., 2021). PVA also offers optical transparency and is

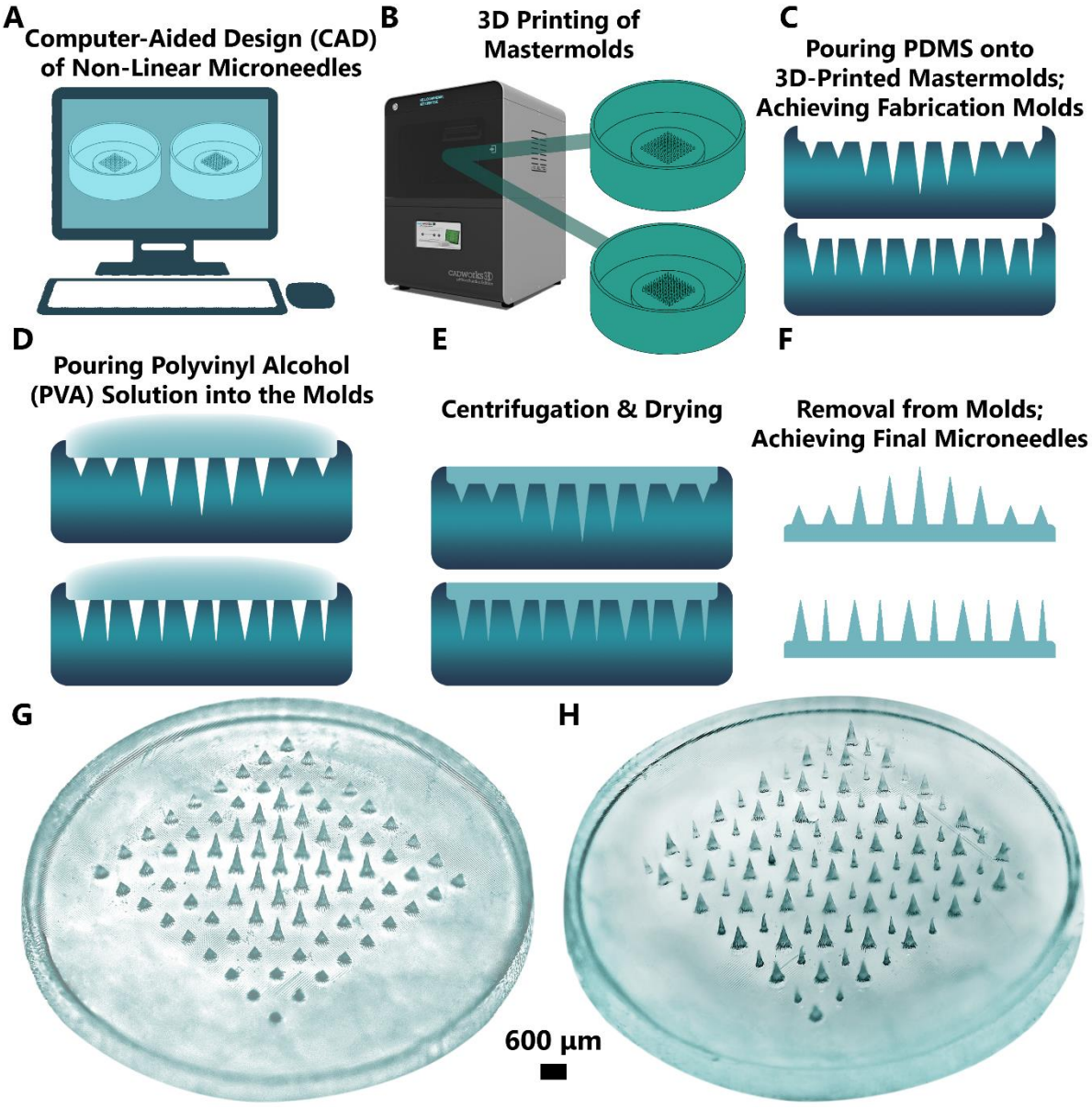

Fig 5.3. The fabrication procedure and microscopy photos of the nonlinear MNAs. (A) The arrays were modeled using computer-aided design (CAD) and computer-aided engineering (CAE). (B) Master molds were 3D-printed using stereolithography (SLA) technology. (C) Fabrication molds were prepared by pouring and drying PDMS onto the master molds. (D) PVA was poured into the fabrication molds, and (E) they were centrifuged. After drying overnight, (F) the final MNAs were achieved by removal from the molds. (G) The mountain design MNA under optical microscope. (H) The wave design MNA under optical microscope (scale bar for G&H = 600 µm).

advantageous for microscopic and dye-tracing applications. The release of the drug or dye from the MNs can be achieved and controlled through degradation of the PVA polymer. Additionally, geometry of the needle which determines the volume of each MN, in another important metric for drug delivery (Ghanbariamin et al., 2023). By governing these factors, nonlinear MNAs can benefit from the mentioned advantages. The mountain design with varying aspect ratio (diameter/height) of 0.25 to 0.75 was successfully fabricated which allows the targeting of multiple layers of the skin in a single administration. On the other hand, the wave design with various diameters of needles which allows volume capacity of four times higher in the larger needles in comparison with the needles with the smaller diameter on the array, was also successfully fabricated. The microscopy analysis of the fabrication products (**Figure 5.3G-H** and **Supplementary Figure 5.S.1**), demonstrate a smooth surface with precise outcome expected from the designed needles without material failure in line with the simulation results for both mountain and wave designs.

5.3.4. Characterization of MNAs' Drug Delivery Efficiency

The investigation into the drug delivery efficiency of MNAs was conducted by assessing the degradation of MNs through the characterization of size reduction. Experimental evaluations of drug delivery efficiency were performed utilizing buffer solutions designed to mimic the pH of human skin (Luzuriaga et al., 2018). Specifically, a buffer solution composed of potassium hydrogen phthalate and sodium hydroxide, with a pH of approximately 5 (analogous to human skin pH), was employed for these experiments. Starch was incorporated into the solution as a thickening agent (M. R. Sarabi et al., 2022), yielding a gel environment that closely resembled human skin conditions (**Supplementary Figure 5.S.2-A**). Subsequently, the MNAs were manually inserted into the artificially created human skin (**Supplementary Figure 5.S.2-B**), and at various time intervals thereafter, the reduction in needle size was scrutinized (**Supplementary Figure 5.S.2-C-D**). The analysis involved a comparative assessment of the height or diameter of the needles, as evidenced by optical microscopic images captured at each designated time interval for both mountain design (**Figure 5.4A**) and wave design (**Supplementary Figure 5.S.2-E**). Degradation of the needles on the array facilitated a comprehensive exhibitor of drug delivery kinetics, thereby contributing valuable insights into the drug delivery efficacy of the MNAs. The consistent findings with prior reports on the degradation/recovery of PVA MNAs (Ma et al., 2024; Oh et al., 2022; Xu et al., 2022) underscore the reliability and coherence of the presented results. In the context of the mountain design, the entirety of the MNs experienced degradation within a time frame of less than ~20 mins, with 50% degradation achieved within the initial ~7 mins (**Figure 5.4B**). The observed expedited degradation of shorter needles, owing to their smaller volume, aligns with anticipated outcomes. Additionally, in the case of the wave design, the complete degradation of all needles occurred within a period of less than ~35 mins, and 50% degradation was attained within ~8 mins (**Figure 5.4C**). Notably, the figure illustrates a discernible trend indicating the accelerated degradation of needles with a diameter of 150 μm, signifying a correspondingly swifter drug delivery process when compared to needles with a diameter of 300 μm. This pattern suggests a manifestation of multi-burst release characteristics.

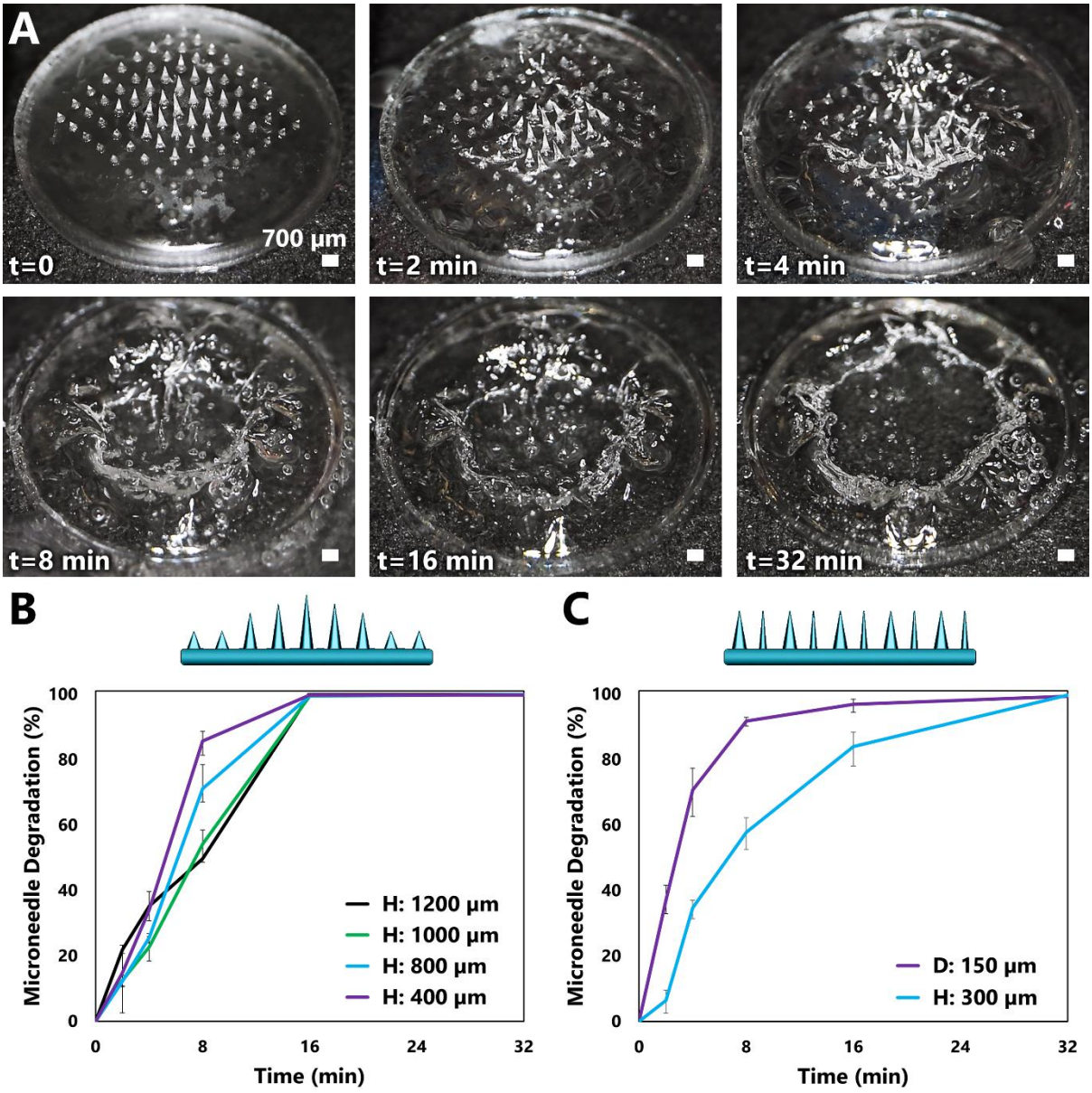

Fig 5.4. Characterization of MNAs drug delivery efficiency based on MN degradation. (A) Within several time intervals, optical microscopic photos of the mountain MNAs after insertion into artificial human skin, a gel environment similar to human skin with a resembling skin pH, were taken. Scale bars for all: 700 µm. Degradation of the needles on the array as an exhibitor of drug delivery kinetics was analyzed based on size reduction of the needles (n=3), for each geometry of the needles on the array for (B) the MNA with mountain design, and (C) for MNA with wave design.

In order to further characterize efficiency of MNAs for model drug delivery, a custom holder for the bovine gel, designed in the shape of a semicircle, was fabricated using 3D printing (**Figure 5.5A**). A glass slide was subsequently attached to its side to enable visualization (**Figure 5.5B**). This setup was utilized to observe the degradation of MNAs with wave design and the delivery of blue dye as a model drug. Time-lapse photography documenting the degradation of the MNAs and the delivery of the model drug into the gelatin (**Figure 5.5C**) indicates a successful application. Degradation photos of needles inside the bovine gel was then processed to calculate the percentage of the MNA degradation over time

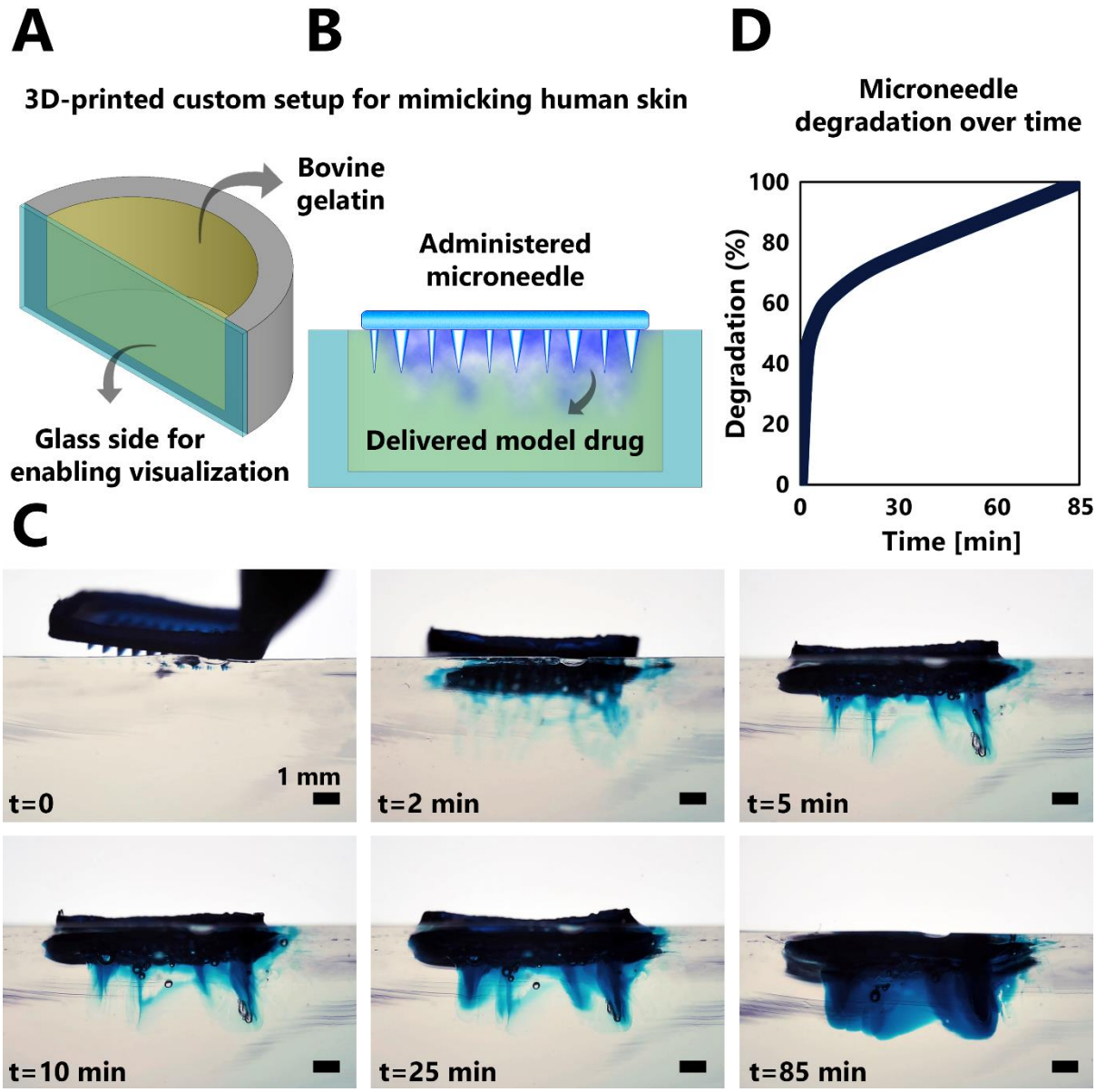

Fig 5.5. Characterization of MNA efficiency for model drug delivery. (A) Custom 3D-printed setup developed for visualization of MNA degradation in gel environment mimicking human skin. (B) The setup was filled with bovine gelatin and the MNA with wave design carrying Blue Dye as a model drug was inserted into the top. (C) Time-lapse photos of MNA degradation and model drug delivery in the gelatin. Scale bars: 1000 µm. (D) Degradation percentage of the MNA over time inside bovine gelatin.

(**Supplementary Figure 5.S.3**), and the results were shown as a curve (**Figure 5.5D**), showcasing 60% degradation achieved within the initial ~10 mins.

Characterization of MNA efficiency was further investigated for model drug delivery. The assessment of drug release matrices commonly employs a model drug to investigate effectiveness. RhB stands out prominently as one of the most renowned model drugs in the literature pertaining to MN research with widespread use. RhB also possesses fluorescent properties, rendering it as a dye for tracking and analysis purposes. Concurrently, the application of gelatin hydrogel, derived from bovine skin and acknowledged for its optical transparency

and physiological resemblance to human skin tissue, has been utilized as a pertinent model for conducting drug release studies involving MNs containing dyes (Gao et al., 2019; Ghanbariamin et al., 2023; Nejad et al., 2018b). In this context, MNAs with mountain design incorporating RhB were systematically observed over temporal intervals to assess their delivery capabilities into gelatin (**Figure 5.6A**). Top view of the gelatin right after removal of the inserted MNA (**Supplementary Figure 5.S.4**) demonstrates successful administration of the MNA and complete piercing of gelatin. Also, it can be observed that degradation of the needles and RhB delivery occurred within a time frame of ~40 mins, consistent with previous reports of MNAs encapsulating dyes (Gao et al., 2019; Nejad et al., 2018b; Xu et al., 2022). Finally in order to demonstrate the insertion site on gelatin, dyes with different colors were used on the administration site for better visualization (**Figure 5.6B**), with green color representing the mountain design and blue color representing the wave design. Close-up views of the needle insertion site for the mountain design (**Figure 5.6C**) and the wave design (**Figure 5.6D**) demonstrate successful administration of the MNAs on gelatin environment.

The dual encapsulation of two distinct dyes as model drugs within MNA featuring the mountain design (**Figure 5.6E**), which was fabricated by manual loading of PVA solutions encapsulating various colors of dyes, can demonstrate a significant advancement in drug delivery systems. This innovative approach highlights the MNA's capacity to simultaneously carry and deliver two different medications, potentially improving treatment efficacy for complex medical conditions. By utilizing the unique mountain design, the MNA ensures a controlled and targeted release of each drug at different skin depths, showcasing its potential for versatile therapeutic applications. This method underscores the MNA's capability in addressing multifaceted skin diseases, paving the way for more sophisticated and effective medical treatments.

Finally, the capability of MNAs for application on human skin was rigorously validated through a series of *ex vivo* and *in vivo* experiments. For this investigation, excised human skin samples were utilized, providing a realistic and clinically relevant substrate for testing. The MNAs were carefully inserted into the skin samples using a spring applicator (**Figure 5.7A**), in order to standardize the experiments regarding insertion force along with ensuring parallel position of the array to skin. This procedure demonstrated successful penetration of the needles into the epidermal and dermal layers of the skin. To further corroborate these findings, the skin samples were subjected to histological analysis. Cross-sectional cuts of the skin, stained with hematoxylin and eosin (H&E), were examined under bright-field microscopy (**Figure 5.7B**). The histological images revealed the precise administration sites of the MNAs, providing detailed close-up views of the micro wounds (**Figure 5.7B ii, iii**) and micro punctures (**Figure 5.7B iv, v**) created by the needles. Additionally, the MNA was also administered in a similar manner onto the arm skin, *in vivo*, of a human subject, male, 27 years old, (**Figure 5.7C**). The MNA was dyed with methylene blue for visualization purposes. Histological views of the site demonstrated successful penetration of the needles into the epidermal and dermal layers of the skin, with visible micro wounds (**Figure 5.7B ii, iii, iv**) and micro punctures (**Figure 5.7B iii, v, vi**) created by needles, along with traces of the dye as delivered model drug (**Figure 5.7B ii, iii, vi**). This microscopic examination of the histology photos confirmed the mechanical efficacy of the MNAs in breaching the stratum corneum and creating

localized microchannels in the skin tissue, which are critical for their intended biomedical applications.

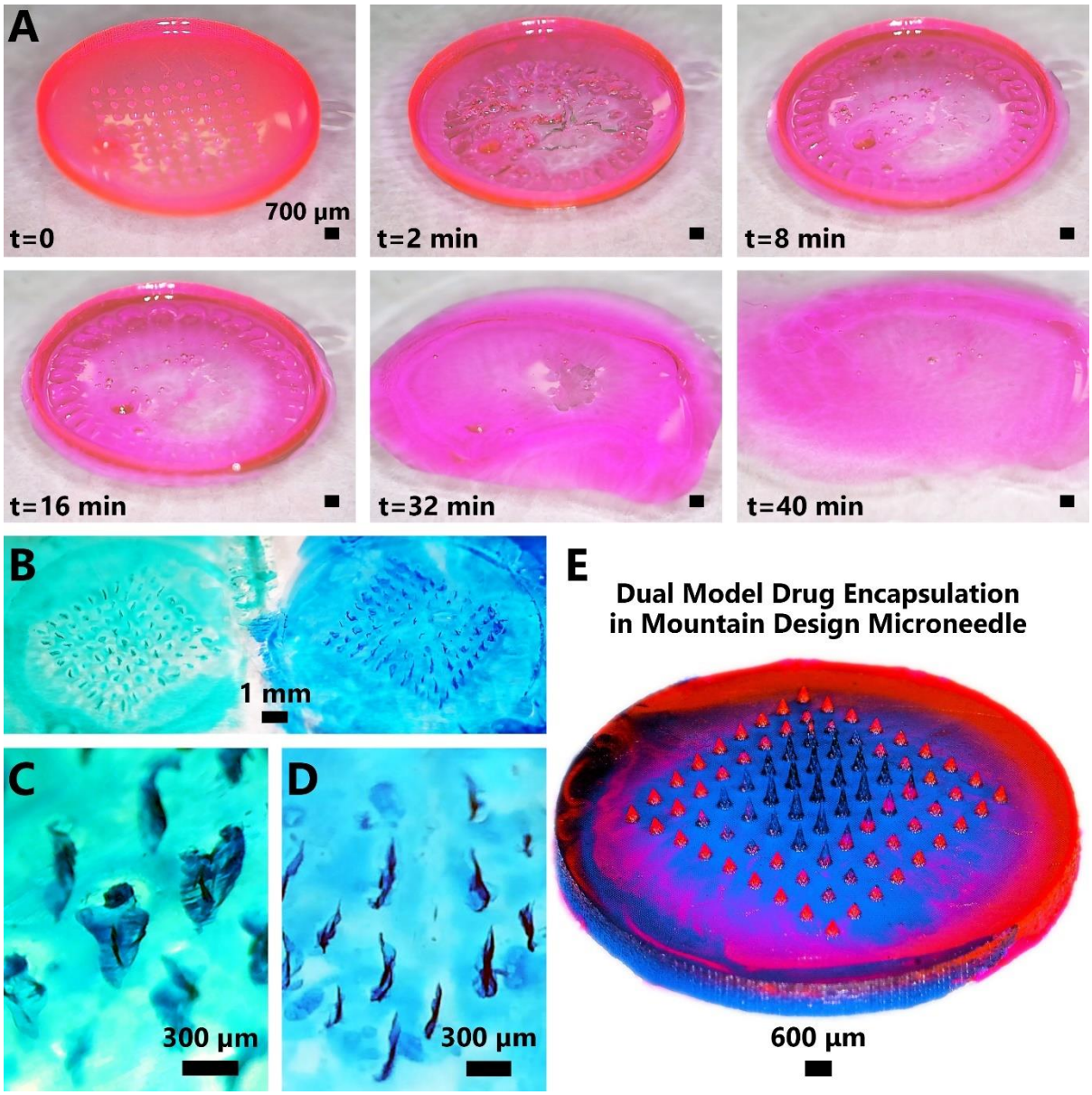

Fig 5.6. Characterization of MNA efficiency for model drug delivery. (A) Time-lapse photos of MNA with mountain design inserted into gelatin. Delivery of RhB as a model drug which was loaded on the MNAs can be observed over time. Scale bars: 700 µm. (B) The insertion site after removal of the MNAs were colored with dyes for better visualization, with green color representing the mountain design and blue color representing the wave design. Scale bar: 1 mm. Close-up views of the needle insertion sites for (C) mountain design and (D) wave design. Scale bar for D-E: 300 µm. (E) Dual encapsulation of two different dyes as model drugs in the MNA with mountain design showcasing capability of simultaneous carrying of two different therapeutic agents.

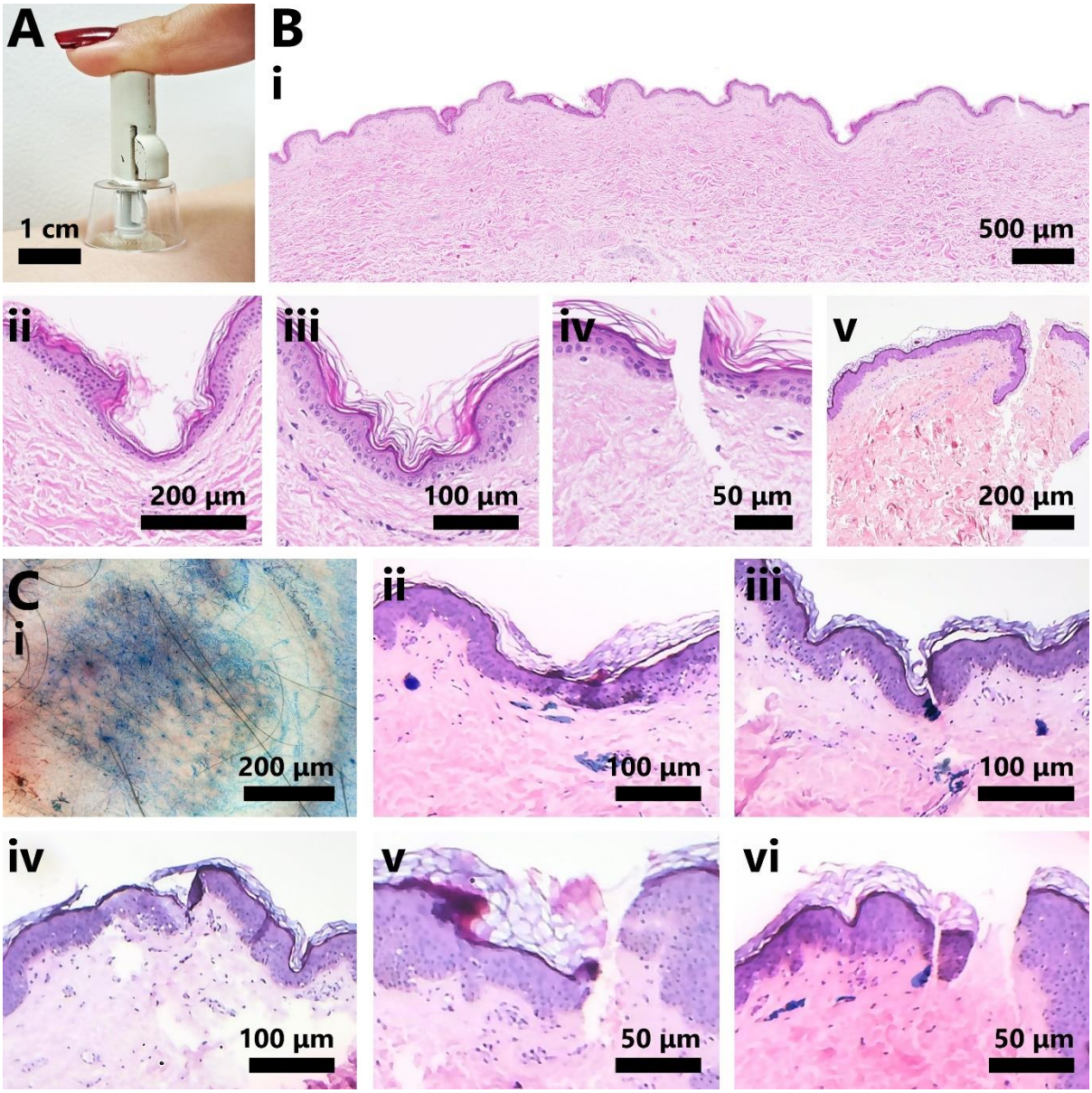

Fig 5.7. Administration of MNAs on human skin *ex vivo* and *in vivo* along with histology characterization. (A) MNAs were inserted into human skin using a spring applicator. Scale bar: 1 cm. (B) Cross sectional histological views of the site where MNA was administrated on skin *ex vivo*, stained with hematoxylin and eosin (H&E), representing the (i) needle administration site, and (ii-v) closeup views of the micro wounds and micro punctures created by needles. Scale bars [µm]: 500, 200, 100, 50, and 200 for i-v, respectively. (C) Administration site of MNA dyed with methylene blue on (i) skin in vivo, and (ii-vi) cross sectional histological views of the site stained with H&E, demonstrating micro wounds and micro punctures created by needles, along with traces of the dye as delivered model drug. Scale bars [µm]: 200, 100, 100, 100, 50, and 50 for i-vi, respectively.

5.4. Outlook

MNAs have garnered considerable attention within the realm of drug delivery, owing to their noteworthy characteristics, particularly the ability to administer

substances in a painless and minimally invasive manner. In this study, we have systematically engineered the MNs in a nonlinear fashion, incorporating diverse needle heights within the array to enable simultaneous drug delivery to different layers of the skin. Furthermore, the manipulation of the base diameter of the needles in the array facilitates the option for sustained or intermittent drug release, contingent upon the biodegradation kinetics of these needles. Employing the emerging technology of 3D printing, coupled with the micro-molding technique, we successfully fabricated our MNAs. Their drug delivery capabilities were systematically evaluated using phantoms that closely mimic skin along with ex vivo human skin. The innovative nonlinear design of the MNs on the array introduces a novel perspective for addressing skin diseases at varying depths. Subsequent research endeavors may explore the influence of geometrical properties to achieve multi-burst delivery within predefined timeframes. Additionally, the synergistic integration of mountain and wave designs can further propel advancements in drug delivery methodologies utilizing MNAs.

Chapter 6: Conclusion

In conclusion, this thesis demonstrates the transformative potential of microneedle arrays in the biomedical field through the application of advanced 3D printing and microfabrication techniques. By addressing the limitations of conventional needle technologies, these innovative microneedles offer a paradigm shift in drug delivery and body fluid sampling, providing precise, minimally invasive channels that reduce penetration pain and tissue damage. The integration of artificial intelligence in the manufacturing processes further enhances the precision and quality control of biodegradable microneedles, ensuring optimized fabrication outcomes. The promising results in treating Basal Cell Carcinoma with microneedles loaded with Marshmallow root extract and Imiquimod highlight the potential for targeted, controlled release therapies with minimal side effects. The research also underscores the versatility of microneedle arrays in treating skin diseases by engineering nonlinear designs with varying needle heights and base diameters, enabling concurrent and sustained drug delivery to different skin layers. Ultimately, this thesis establishes that microneedle arrays hold immense promise for advancing personalized healthcare solutions, offering painless, efficient, and highly effective methods for drug administration and body fluid collection.

Bibliography

Adams, M., Johnston, M., Scherer, A., & Quake, S. (2005). Polydimethylsiloxane based microfluidic diode. *Journal of Micromechanics and Microengineering*, *15*(8), 1517.

Adhikari, B. B., Goodson, J. L., Chu, S. Y., Rota, P. A., & Meltzer, M. I. (2016). Assessing the Potential Cost-Effectiveness of Microneedle Patches in Childhood Measles Vaccination Programs: The Case for Further Research and Development. *Drugs in R&D*, *16*(4), 327-338. https://doi.org/10.1007/s40268-016-0144-x

Agache, P. G., Monneur, C., Leveque, J. L., & De Rigal, J. (1980). Mechanical properties and Young's modulus of human skin in vivo. *Archives of Dermatological Research*, *269*(3), 221-232. https://doi.org/10.1007/BF00406415

Ahlborg, G., & Jensen-Urstad, M. (1991). Arm blood flow at rest and during arm exercise. *Journal of applied physiology*, *70*(2), 928-933.

Ahmadpour, A., Isgor, P. K., Ural, B., Eren, B. N., Sarabi, M. R., Muradoglu, M., & Tasoglu, S. (2023). Microneedle arrays integrated with microfluidic systems: Emerging applications and fluid flow modeling. *Biomicrofluidics*, *17*(2). https://doi.org/Artn 021501

10.1063/5.0121578

Aimar, A., Palermo, A., & Innocenti, B. (2019). The role of 3D printing in medical applications: a state of the art. *Journal of Healthcare Engineering*, *2019*.

Aksit, A., Arteaga, D. N., Arriaga, M., Wang, X., Watanabe, H., Kasza, K. E., Lalwani, A. K., & Kysar, J. W. (2018). In-vitro perforation of the round window membrane via direct 3-D printed microneedles. *Biomedical Microdevices*, *20*(2), 47. https://doi.org/10.1007/s10544-018-0287-3

Al Sulaiman, D., Chang, J. Y., Bennett, N. R., Topouzi, H., Higgins, C. A., Irvine, D. J., & Ladame, S. (2019). Hydrogel-coated microneedle arrays for minimally invasive sampling and sensing of specific circulating nucleic acids from skin interstitial fluid. *ACS Nano*, *13*(8), 9620-9628.

Ali, R., Mehta, P., Arshad, M., Kucuk, I., Chang, M., & Ahmad, Z. (2020). Transdermal microneedles—a materials perspective. *AAPS PharmSciTech*, *21*(1), 12.

Ali, R., Mehta, P., Arshad, M. S., Kucuk, I., Chang, M. W., & Ahmad, Z. (2019). Transdermal Microneedles—A Materials Perspective. *AAPS PharmSciTech*, *21*(1), 12. https://doi.org/10.1208/s12249-019-1560-3

Alsuliman, T., Humaidan, D., & Sliman, L. (2020). Machine learning and artificial intelligence in the service of medicine: Necessity or potentiality? *Current Research in Translational Medicine*, *68*(4), 245-251. https://doi.org/https://doi.org/10.1016/j.retram.2020.01.002

Amer, R. I., El-Osaily, G. H., Bakr, R. O., El Dine, R. S., & Fayez, A. M. (2020). Characterization and Pharmacological Evaluation of Anti-Cellulite Herbal Product(s) Encapsulated in 3D-Fabricated Polymeric Microneedles. *Scientific reports*, *10*(1), 6316. https://doi.org/10.1038/s41598-020-63271-6

Amin, R., Knowlton, S., Hart, A., Yenilmez, B., Ghaderinezhad, F., Katebifar, S., Messina, M., Khademhosseini, A., & Tasoglu, S. (2016). 3D-printed microfluidic devices. *Biofabrication*, *8*(2), 022001. https://doi.org/10.1088/1758-5090/8/2/022001

Amin, R., Knowlton, S., Yenilmez, B., Hart, A., Joshi, A., & Tasoglu, S. (2016). Smartphone attachable, flow-assisted magnetic focusing device. *RSC advances*, *6*(96), 93922-93931.

Aukland, K., & Reed, R. K. (1993). Interstitial-lymphatic mechanisms in the control of extracellular fluid volume. *Physiological reviews*, *73*(1), 1-78.

Baek, S.-H., Shin, J.-H., & Kim, Y.-C. (2017). Drug-coated microneedles for rapid and painless local anesthesia. *Biomedical Microdevices*, *19*(1), 2.

Bakhshinejad, A., & D'souza, R. M. (2015). A brief comparison between available bioprinting methods. 2015 IEEE Great Lakes biomedical conference (GLBC),

Balmert, S. C., Carey, C. D., Falo, G. D., Sethi, S. K., Erdos, G., Korkmaz, E., & Falo, L. D. (2020). Dissolving undercut microneedle arrays for multicomponent cutaneous vaccination. *Journal of Controlled Release*, *317*, 336-346. https://doi.org/https://doi.org/10.1016/j.jconrel.2019.11.023

Bevers, T. B. (2001). Breast cancer chemoprevention: current clinical practice and future direction. *Biomedicine & Pharmacotherapy*, *55*(9-10), 559-564.

Bhatnagar, S., Dave, K., & Venuganti, V. V. K. (2017). Microneedles in the clinic. *Journal of Controlled Release*, *260*, 164-182.

Bhatnagar, S., Gadeela, P. R., Thathireddy, P., & Venuganti, V. V. K. (2019). Microneedle-based drug delivery: materials of construction. *Journal of Chemical Sciences (Bangalore, India)*, *131*(9), 90.

Bonaccorso, G. (2017). *Machine learning algorithms*. Packt Publishing Ltd.

Caffarel-Salvador, E., Brady, A. J., Eltayib, E., Meng, T., Alonso-Vicente, A., Gonzalez-Vazquez, P., Torrisi, B. M., Vicente-Perez, E. M., Mooney, K., & Jones, D. S. (2015). Hydrogel-forming microneedle arrays allow detection of drugs and glucose in vivo: potential for use in diagnosis and therapeutic drug monitoring. *PLoS One*, *10*(12), e0145644.

Cai, B., Gong, Y., Wang, Z., Wang, L., & Chen, W. (2021). Microneedle arrays integrated with living organisms for smart biomedical applications. *Theranostics*, *11*(20), 10012-10029. https://doi.org/10.7150/thno.66478

Camović, M., Biščević, A., Brčić, I., Borčak, K., Bušatlić, S., Ćenanović, N., Dedović, A., Mulalić, A., Osmanlić, M., & Sirbubalo, M. (2019). Coated 3d printed PLA microneedles as transdermal drug delivery systems. International Conference on Medical and Biological Engineering,

Castilla-Casadiego, D. A., Carlton, H., Gonzalez-Nino, D., Miranda-Muñoz, K. A., Daneshpour, R., Huitink, D., Prinz, G., Powell, J., Greenlee, L., & Almodovar, J. (2021). Design, characterization, and modeling of a chitosan microneedle patch for transdermal delivery of meloxicam as a pain management strategy for use in cattle. *Materials Science and Engineering: C*, *118*, 111544. https://doi.org/https://doi.org/10.1016/j.msec.2020.111544

Caudill, C. L., Perry, J. L., Tian, S., Luft, J. C., & DeSimone, J. M. (2018). Spatially controlled coating of continuous liquid interface production microneedles for transdermal protein delivery. *Journal of Controlled Release*, *284*, 122-132. https://doi.org/https://doi.org/10.1016/j.jconrel.2018.05.042

Chambers, R. (1921). Microdissection studies, III. Some problems in the maturation and fertilization of the echinoderm egg. *The Biological Bulletin*, *41*(6), 318-350.

Chang, H., Zheng, M., Yu, X., Than, A., Seeni, R. Z., Kang, R., Tian, J., Khanh, D. P., Liu, L., & Chen, P. (2017). A swellable microneedle patch to rapidly extract skin interstitial fluid for timely metabolic analysis. *Advanced materials*, *29*(37), 1702243.

Chang, H., Zheng, M., Yu, X., Than, A., Seeni, R. Z., Kang, R., Tian, J., Khanh, D. P., Liu, L., Chen, P., & Xu, C. (2017). A Swellable Microneedle Patch to Rapidly

Extract Skin Interstitial Fluid for Timely Metabolic Analysis. *Advanced Materials*, *29*(37), 1702243. https://doi.org/10.1002/adma.201702243

Chang, K.-T., Shen, Y.-K., Fan, F.-Y., Lin, Y., & Kang, S.-C. (2020). Optimal design and fabrication of a microneedle arrays patch. *Journal of Manufacturing Processes*, *54*, 274-285. https://doi.org/https://doi.org/10.1016/j.jmapro.2020.02.024

Chen, B. Z., He, Y. T., Zhao, Z. Q., Feng, Y. H., Liang, L., Peng, J., Yang, C. Y., Uyama, H., Shahbazi, M.-A., & Guo, X. D. (2023). Strategies to develop polymeric microneedles for controlled drug release. *Advanced Drug Delivery Reviews*, *203*, 115109.

Chen, H., Wu, B., Zhang, M., Yang, P., Yang, B., Qin, W., Wang, Q., Wen, X., Chen, M., Quan, G., Pan, X., & Wu, C. (2019). A novel scalable fabrication process for the production of dissolving microneedle arrays. *Drug Delivery and Translational Research*, *9*(1), 240-248. https://doi.org/10.1007/s13346-018-00593-z

Chen, J., Liu, C.-Y., Wang, X., Sweet, E., Liu, N., Gong, X., Lin, L. J. B., & Bioelectronics. (2020). 3D printed microfluidic devices for circulating tumor cells (CTCs) isolation. *150*, 111900.

Chen, J., Qiu, Y., Zhang, S., Yang, G., & Gao, Y. (2015). Controllable coating of microneedles for transdermal drug delivery. *Drug development and industrial pharmacy*, *41*(3), 415-422.

Chen, J., Wang, M., Ye, Y., Yang, Z., Ruan, Z., & Jin, N. (2019). Fabrication of sponge-forming microneedle patch for rapidly sampling interstitial fluid for analysis. *Biomedical microdevices*, *21*(3), 1-10.

Chen, M., Hao, Y., Hwang, K., Wang, L., & Wang, L. (2017). Disease Prediction by Machine Learning Over Big Data From Healthcare Communities. *IEEE Access*, *5*, 8869-8879. https://doi.org/10.1109/ACCESS.2017.2694446

Chen, Z., Li, Z., Li, J., Liu, C., Lao, C., Fu, Y., Liu, C., Li, Y., Wang, P., & He, Y. (2019). 3D printing of ceramics: A review. *Journal of the European Ceramic Society*, *39*(4), 661-687. https://doi.org/https://doi.org/10.1016/j.jeurceramsoc.2018.11.013

Chen, Z., Ren, L., Li, J., Yao, L., Chen, Y., Liu, B., & Jiang, L. (2018). Rapid fabrication of microneedles using magnetorheological drawing lithography. *Acta Biomaterialia*, *65*, 283-291. https://doi.org/https://doi.org/10.1016/j.actbio.2017.10.030

Chen, Z., Ye, R., Yang, J., Lin, Y., Lee, W., Li, J., Ren, L., Liu, B., & Jiang, L. (2019). Rapidly Fabricated Microneedle Arrays Using Magnetorheological Drawing Lithography for Transdermal Drug Delivery. *ACS Biomaterials Science & Engineering*, *5*(10), 5506-5513.

Chi, Y., Huang, Y., Kang, Y., Dai, G., Liu, Z., Xu, K., & Zhong, W. (2022). The effects of molecular weight of hyaluronic acid on transdermal delivery efficiencies of dissolving microneedles. *European Journal of Pharmaceutical Sciences*, *168*, 106075. https://doi.org/https://doi.org/10.1016/j.ejps.2021.106075

Chia, H. N., & Wu, B. M. (2015). Recent advances in 3D printing of biomaterials. *Journal of Biological Engineering*, *9*(1), 4. https://doi.org/10.1186/s13036-015-0001-4

Chiang, H., Yu, M., Aksit, A., Wang, W., Stern-Shavit, S., Kysar, J. W., & Lalwani, A. K. (2020). 3D-printed microneedles create precise perforations in human round window membrane in situ. *Otology & Neurotology*, *41*(2), 277-284.

Chiappini, C., De Rosa, E., Martinez, J. O., Liu, X., Steele, J., Stevens, M. M., & Tasciotti, E. (2015). Biodegradable silicon nanoneedles delivering nucleic acids intracellularly induce localized in vivo neovascularization. *Nature Materials*, *14*(5), 532-539. https://doi.org/10.1038/nmat4249

Cordeiro, A. S., Tekko, I. A., Jomaa, M. H., Vora, L., McAlister, E., Volpe-Zanutto, F., Nethery, M., Baine, P. T., Mitchell, N., & McNeill, D. W. (2020). Two-Photon Polymerisation 3D Printing of Microneedle Array Templates with Versatile Designs: Application in the Development of Polymeric Drug Delivery Systems. *Pharmaceutical Research*, *37*(9), 1-15.

Cordeiro, A. S., Tekko, I. A., Jomaa, M. H., Vora, L., McAlister, E., Volpe-Zanutto, F., Nethery, M., Baine, P. T., Mitchell, N., McNeill, D. W., & Donnelly, R. F. (2020). Two-Photon Polymerisation 3D Printing of Microneedle Array Templates with Versatile Designs: Application in the Development of Polymeric Drug Delivery Systems. *Pharmaceutical Research*, *37*(9), 174. https://doi.org/10.1007/s11095-020-02887-9

Crisan, D., Kastler, S., Scharffetter-Kochanek, K., Crisan, M., & Schneider, L. A. (2023). Ultrasonographic assessment of depth infiltration in melanoma and non-melanoma skin cancer. *Journal of Ultrasound in Medicine*, *42*(7), 1609-1616.

Dabbagh, S. R., Sarabi, M. R., Rahbarghazi, R., Sokullu, E., Yetisen, A. K., & Tasoglu, S. (2021). 3D-printed microneedles in biomedical applications. *iScience*, *24*(1), 102012. https://doi.org/https://doi.org/10.1016/j.isci.2020.102012

Damiri, F., Kommineni, N., Ebhodaghe, S. O., Bulusu, R., Jyothi, V. G. S. S., Sayed, A. A., Awaji, A. A., Germoush, M. O., Al-malky, H. S., Nasrullah, M. Z., Rahman, M. H., Abdel-Daim, M. M., & Berrada, M. (2022). Microneedle-Based Natural Polysaccharide for Drug Delivery Systems (DDS): Progress and Challenges. *Pharmaceuticals*, *15*(2), 190. https://www.mdpi.com/1424-8247/15/2/190

Davis, S. P., Landis, B. J., Adams, Z. H., Allen, M. G., & Prausnitz, M. R. (2004). Insertion of microneedles into skin: measurement and prediction of insertion force and needle fracture force. *Journal of Biomechanics*, *37*(8), 1155-1163. https://doi.org/https://doi.org/10.1016/j.jbiomech.2003.12.010

Defard, T., Setkov, A., Loesch, A., & Audigier, R. (2021). Padim: a patch distribution modeling framework for anomaly detection and localization. International Conference on Pattern Recognition,

DeMuth, P. C., Li, A. V., Abbink, P., Liu, J., Li, H., Stanley, K. A., Smith, K. M., Lavine, C. L., Seaman, M. S., & Kramer, J. A. (2013). Vaccine delivery with microneedle skin patches in nonhuman primates. *Nature biotechnology*, *31*(12), 1082-1085.

Deng, J., Dong, W., Socher, R., Li, L.-J., Li, K., & Fei-Fei, L. (2009). Imagenet: A large-scale hierarchical image database. 2009 IEEE conference on computer vision and pattern recognition,

Dhinakaran, V., Kumar, K. M., Ram, P. B., Ravichandran, M., & Vinayagamoorthy, M. (2020). A review on recent advancements in fused deposition modeling. *Materials Today: Proceedings*.

Donnelly, R. F., Majithiya, R., Singh, T. R. R., Morrow, D. I. J., Garland, M. J., Demir, Y. K., Migalska, K., Ryan, E., Gillen, D., Scott, C. J., & Woolfson, A. D. (2011). Design, Optimization and Characterisation of Polymeric Microneedle Arrays Prepared by a Novel Laser-Based Micromoulding Technique. *Pharmaceutical Research*, *28*(1), 41-57. https://doi.org/10.1007/s11095-010-0169-8

Donnelly, R. F., McCrudden, M. T., Alkilani, A. Z., Larrañeta, E., McAlister, E., Courtenay, A. J., Kearney, M.-C., Singh, T. R. R., McCarthy, H. O., & Kett, V. L. (2014). Hydrogel-forming microneedles prepared from "super swelling" polymers combined with lyophilised wafers for transdermal drug delivery. *PLoS One*, *9*(10), e111547.

Douroumis, D. (2019). 3D printing of pharmaceutical and medical applications: a new era. In: Springer.

Ebah, L. (2012). Extraction and analysis of interstitial fluid, and characterisation of the interstitial compartment in kidney disease.

Economidou, S. N., Pere, C. P. P., Reid, A., Uddin, M. J., Windmill, J. F. C., Lamprou, D. A., & Douroumis, D. (2019). 3D printed microneedle patches using stereolithography (SLA) for intradermal insulin delivery. *Materials Science and Engineering: C*, *102*, 743-755. https://doi.org/https://doi.org/10.1016/j.msec.2019.04.063

Eggleston, T. A., Roach, W., Mitchell, M. A., Smith, K., Oler, D., & Johnson, T. E. (2000). Comparison of two porcine (Sus scrofa domestica) skin models for in vivo near-infrared laser exposure. *Comparative medicine*, *50*(4), 391-397.

Esteva, A., Robicquet, A., Ramsundar, B., Kuleshov, V., DePristo, M., Chou, K., Cui, C., Corrado, G., Thrun, S., & Dean, J. (2019). A guide to deep learning in healthcare. *Nature Medicine*, *25*(1), 24-29. https://doi.org/10.1038/s41591-018-0316-z

Faraji Rad, Z., Nordon, R. E., Anthony, C. J., Bilston, L., Prewett, P. D., Arns, J.-Y., Arns, C. H., Zhang, L., & Davies, G. J. (2017). High-fidelity replication of thermoplastic microneedles with open microfluidic channels. *Microsystems & nanoengineering*, *3*(1), 17034. https://doi.org/10.1038/micronano.2017.34

Farhan, S. A., Shaikh, A. T., Zia, M., Kahara, B. R., Muneer, R., Rehman, M., Mubashir, A., Sadiq, H., Siddiqui, D.-E. A., Haseeb, S. M., Tanveer, H., Siddiq, K., Mujtaba, S. B., Mirza, S. A., Feroz, H., & Fatima, K. (2017). Prevalence and Predictors of Home Use of Glucometers in Diabetic Patients. *Cureus*, *9*(6), e1330-e1330. https://doi.org/10.7759/cureus.1330

Faustino, V., Catarino, S. O., Lima, R., & Minas, G. (2016). Biomedical microfluidic devices by using low-cost fabrication techniques: A review. *Journal of Biomechanics*, *49*(11), 2280-2292. https://doi.org/https://doi.org/10.1016/j.jbiomech.2015.11.031

Fernandes, D. (2005). Minimally invasive percutaneous collagen induction. *Oral and Maxillofacial Surgery Clinics*, *17*(1), 51-63.

Fonseca, D. F., Costa, P. C., Almeida, I. F., Dias-Pereira, P., Correia-Sá, I., Bastos, V., Oliveira, H., Vilela, C., Silvestre, A. J., & Freire, C. S. (2020). Swellable Gelatin Methacryloyl Microneedles for Extraction of Interstitial Skin Fluid toward Minimally Invasive Monitoring of Urea. *Macromolecular Bioscience*, *20*(10), 2000195.

Frydman, G. H., Olaleye, D., Annamalai, D., Layne, K., Yang, I., Kaafarani, H. M. A., & Fox, J. G. (2020). Manuka honey microneedles for enhanced wound healing and the prevention and/or treatment of Methicillin-resistant Staphylococcus aureus (MRSA) surgical site infection. *Scientific reports*, *10*(1), 13229. https://doi.org/10.1038/s41598-020-70186-9

Gallo, R. L. (2017). Human skin is the largest epithelial surface for interaction with microbes. *Journal of Investigative Dermatology*, *137*(6), 1213-1214.

Gan, Z., Li, H., Wolff, S. J., Bennett, J. L., Hyatt, G., Wagner, G. J., Cao, J., & Liu, W. K. (2019). Data-Driven Microstructure and Microhardness Design in Additive Manufacturing Using a Self-Organizing Map. *Engineering*, *5*(4), 730-735. https://doi.org/https://doi.org/10.1016/j.eng.2019.03.014

Gao, Y., Hou, M., Yang, R., Zhang, L., Xu, Z., Kang, Y., & Xue, P. (2019). Highly Porous Silk Fibroin Scaffold Packed in PEGDA/Sucrose Microneedles for Controllable Transdermal Drug Delivery. *Biomacromolecules*, *20*(3), 1334-1345. https://doi.org/10.1021/acs.biomac.8b01715

García-López, E., Siller, H. R., & Rodríguez, C. A. (2018). Study of the fabrication of AISI 316L microneedle arrays. *Procedia Manufacturing*, *26*, 117-124. https://doi.org/https://doi.org/10.1016/j.promfg.2018.07.014

Garg, A., Lam, J. S. L., & Savalani, M. (2016). A new variant of genetic programming in formulation of laser energy consumption model of 3D printing process. In *Handbook of sustainability in additive manufacturing* (pp. 31-50). Springer.

Geng, Q., Wang, D., Chen, P., & Chen, S.-C. (2019). Ultrafast multi-focus 3-D nano-fabrication based on two-photon polymerization. *Nature Communications*, *10*(1), 1-7.

Gerstel, M. S., & Place, V. A. (1976). Drug delivery device. In: Google Patents.

Ghaderinezhad, F., Koydemir, H. C., Tseng, D., Karinca, D., Liang, K., Ozcan, A., & Tasoglu, S. (2020). Sensing of electrolytes in urine using a miniaturized paper-based device. *Scientific Reports*, *10*(1), 1-9.

Ghanbariamin, D., Samandari, M., Ghelich, P., Shahbazmohamadi, S., Schmidt, T. A., Chen, Y., & Tamayol, A. (2023). Cleanroom-Free Fabrication of Microneedles for Multimodal Drug Delivery. *Small*, *19*(29), 2207131. https://doi.org/https://doi.org/10.1002/smll.202207131

Gholami, S., Mohebi, M.-M., Hajizadeh-Saffar, E., Ghanian, M.-H., Zarkesh, I., & Baharvand, H. (2019). Fabrication of microporous inorganic microneedles by centrifugal casting method for transdermal extraction and delivery. *International Journal of Pharmaceutics*, *558*, 299-310.

Gill, H. S., Denson, D. D., Burris, B. A., & Prausnitz, M. R. (2008). Effect of microneedle design on pain in human volunteers. *The Clinical journal of pain*, *24*(7), 585-594. https://doi.org/10.1097/AJP.0b013e31816778f9

Gissibl, T., Thiele, S., Herkommer, A., & Giessen, H. (2016). Two-photon direct laser writing of ultracompact multi-lens objectives. *Nature Photonics*, *10*(8), 554-560.

Goh, G. D., Sing, S. L., & Yeong, W. Y. (2021). A review on machine learning in 3D printing: applications, potential, and challenges. *Artificial Intelligence Review*, *54*(1), 63-94. https://doi.org/10.1007/s10462-020-09876-9

Golsanami, N., Jayasuriya, M. N., Yan, W., Fernando, S. G., Liu, X., Cui, L., Zhang, X., Yasin, Q., Dong, H., & Dong, X. (2022). Characterizing clay textures and their impact on the reservoir using deep learning and Lattice-Boltzmann simulation applied to SEM images. *Energy*, *240*, 122599. https://doi.org/https://doi.org/10.1016/j.energy.2021.122599

Gong, J., Schuurmans, C. C., van Genderen, A. M., Cao, X., Li, W., Cheng, F., He, J. J., López, A., Huerta, V., & Manríquez, J. (2020). Complexation-induced resolution enhancement of 3D-printed hydrogel constructs. *Nature Communications*, *11*(1), 1-14.

Grover, W. H., Skelley, A. M., Liu, C. N., Lagally, E. T., & Mathies, R. A. (2003). Monolithic membrane valves and diaphragm pumps for practical large-scale integration into glass microfluidic devices. *Sensors and Actuators B: Chemical*, *89*(3), 315-323.

Han, D., Morde, R. S., Mariani, S., La Mattina, A. A., Vignali, E., Yang, C., Barillaro, G., & Lee, H. (2020). 4D Printing of a Bioinspired Microneedle Array with Backward-Facing Barbs for Enhanced Tissue Adhesion. *Advanced Functional Materials*, *30*(11), 1909197. https://doi.org/10.1002/adfm.201909197

Haq, M. I., Smith, E., John, D. N., Kalavala, M., Edwards, C., Anstey, A., Morrissey, A., & Birchall, J. C. (2009). Clinical administration of microneedles: skin puncture, pain and sensation. *Biomedical microdevices*, *11*(1), 35-47. https://doi.org/10.1007/s10544-008-9208-1

He, K., Zhang, X., Ren, S., & Sun, J. (2016). Deep residual learning for image recognition. Proceedings of the IEEE conference on computer vision and pattern recognition,

He, R., Niu, Y., Li, Z., Li, A., Yang, H., Xu, F., & Li, F. (2020). A Hydrogel Microneedle Patch for Point-of-Care Testing Based on Skin Interstitial Fluid. *Advanced healthcare materials*, *9*(4), 1901201. https://doi.org/https://doi.org/10.1002/adhm.201901201

Hegde, N. R., Kaveri, S. V., & Bayry, J. (2011). Recent advances in the administration of vaccines for infectious diseases: microneedles as painless delivery devices for mass vaccination. *Drug Discovery Today*, *16*(23), 1061-1068. https://doi.org/https://doi.org/10.1016/j.drudis.2011.07.004

Henry, S., McAllister, D. V., Allen, M. G., & Prausnitz, M. R. (1998). Microfabricated microneedles: a novel approach to transdermal drug delivery. *Journal of Pharmaceutical Sciences*, *87*(8), 922-925.

Hund, S. J., Kameneva, M. V., & Antaki, J. F. (2017). A Quasi-Mechanistic Mathematical Representation for Blood Viscosity. *Fluids*, *2*(1), 10. https://www.mdpi.com/2311-5521/2/1/10

Indermun, S., Luttge, R., Choonara, Y. E., Kumar, P., Du Toit, L. C., Modi, G., & Pillay, V. (2014). Current advances in the fabrication of microneedles for transdermal delivery. *Journal of Controlled Release*, *185*, 130-138.

Ingrole, R. S. J., Azizoglu, E., Dul, M., Birchall, J. C., Gill, H. S., & Prausnitz, M. R. (2021). Trends of microneedle technology in the scientific literature, patents, clinical trials and internet activity. *Biomaterials*, *267*, 120491. https://doi.org/https://doi.org/10.1016/j.biomaterials.2020.120491

Iwai, K., Shih, K. C., Lin, X., Brubaker, T. A., Sochol, R. D., & Lin, L. (2014). Finger-powered microfluidic systems using multilayer soft lithography and injection molding processes. *Lab on a Chip*, *14*(19), 3790-3799.

Jacinto, T. A., Rodrigues, C. F., Moreira, A. F., Miguel, S. P., Costa, E. C., Ferreira, P., & Correia, I. J. (2020). Hyaluronic acid and Vitamin E polyethylene glycol succinate functionalized gold-core silica shell nanorods for cancer targeted photothermal therapy. *Colloids and Surfaces B: Biointerfaces*, 110778.

Jain, A., Mathur, T., Pandian, N. K., & Selahi, A. (2020). Organ-on-a-chip and 3D printing as preclinical models for medical research and practice. In *Precision Medicine for Investigators, Practitioners and Providers* (pp. 83-95). Elsevier.

Javaid, M., & Haleem, A. (2020). 3D printing applications towards the required challenge of stem cells printing. *Clinical Epidemiology and Global Health*.

Jiang, X., & Lillehoj, P. B. (2020). Microneedle-based skin patch for blood-free rapid diagnostic testing. *Microsystems & nanoengineering*, *6*(1), 96. https://doi.org/10.1038/s41378-020-00206-1

Johnson, A. R., Caudill, C. L., Tumbleston, J. R., Bloomquist, C. J., Moga, K. A., Ermoshkin, A., Shirvanyants, D., Mecham, S. J., Luft, J. C., & DeSimone, J. M. (2016). Single-step fabrication of computationally designed microneedles by continuous liquid interface production. *PloS One*, *11*(9).

Johnson, A. R., & Procopio, A. T. (2019). Low cost additive manufacturing of microneedle masters. *3D Printing in Medicine*, *5*(1), 2. https://doi.org/10.1186/s41205-019-0039-x

Jose, A. D., & Collison, D. (1970). The normal range and determinants of the intrinsic heart rate in man. *Cardiovascular research*, *4*(2), 160-167.

Joseph, J., Deshmukh, K., Tung, T., Chidambaram, K., & Pasha, S. K. (2019). 3D Printing Technology of Polymer Composites and Hydrogels for Artificial Skin

Tissue Implementations. In *Polymer Nanocomposites in Biomedical Engineering* (pp. 205-233). Springer.

Kabashima, K., Honda, T., Ginhoux, F., & Egawa, G. (2019). The immunological anatomy of the skin. *Nature Reviews Immunology*, *19*(1), 19-30. https://doi.org/10.1038/s41577-018-0084-5

Kanakaraj, U., Lhaden, T., & Raj, V., Karthik (2015, 19-20 March 2015). Analysis of structural mechanics of solid microneedle using COMSOL software. 2015 International Conference on Innovations in Information, Embedded and Communication Systems (ICIIECS),

Kanakasabapathy, M. K., Thirumalaraju, P., Bormann, C. L., Kandula, H., Dimitriadis, I., Souter, I., Yogesh, V., Pavan, S. K. S., Yarravarapu, D., Gupta, R., Pooniwala, R., & Shafiee, H. (2019). Development and evaluation of inexpensive automated deep learning-based imaging systems for embryology. https://doi.org/10.1039/C9LC00721K

Kang, N.-W., Kim, S., Lee, J.-Y., Kim, K.-T., Choi, Y., Oh, Y., Kim, J., Kim, D.-D., & Park, J.-H. (2020). Microneedles for drug delivery: recent advances in materials and geometry for preclinical and clinical studies. *Expert Opinion on Drug Delivery*. https://doi.org/10.1080/17425247.2021.1828860

Kathuria, H., Kang, K., Cai, J., & Kang, L. (2020). Rapid microneedle fabrication by heating and photolithography. *International Journal of Pharmaceutics*, *575*, 118992. https://doi.org/https://doi.org/10.1016/j.ijpharm.2019.118992

Kavaldzhiev, M., Perez, J. E., Ivanov, Y., Bertoncini, A., Liberale, C., & Kosel, J. (2017). Biocompatible 3D printed magnetic micro needles. *Biomedical Physics & Engineering Express*, *3*(2), 025005.

Ke, K.-H., & Chung, C.-K. (2020). High-Performance Al/PDMS TENG with Novel Complex Morphology of Two-Height Microneedles Array for High-Sensitivity Force-Sensor and Self-Powered Application. *Small*, *16*(35), 2001209. https://doi.org/https://doi.org/10.1002/smll.202001209

Kettwich, S. C., Sibbitt Jr, W. L., Brandt, J. R., Johnson, C. R., Wong, C. S., & Bankhurst, A. D. (2007). Needle phobia and stress-reducing medical devices in pediatric and adult chemotherapy patients. *Journal of Pediatric Oncology Nursing*, *24*(1), 20-28.

Kim, H., Seong, K.-Y., Lee, J. H., Park, W., Yang, S. Y., & Hahn, S. K. (2019). Biodegradable Microneedle Patch Delivering Antigenic Peptide–Hyaluronate Conjugate for Cancer Immunotherapy. *ACS Biomaterials Science & Engineering*, *5*(10), 5150-5158.

Kim, Y.-C., Park, J.-H., & Prausnitz, M. R. (2012). Microneedles for drug and vaccine delivery. *Advanced Drug Delivery Reviews*, *64*(14), 1547-1568. https://doi.org/https://doi.org/10.1016/j.addr.2012.04.005

Klarhöfer, M., Csapo, B., Balassy, C., Szeles, J., & Moser, E. (2001). High-resolution blood flow velocity measurements in the human finger. *Magnetic Resonance in Medicine: An Official Journal of the International Society for Magnetic Resonance in Medicine*, *45*(4), 716-719.

Knowlton, S., Anand, S., Shah, T., & Tasoglu, S. (2018). Bioprinting for neural tissue engineering. *Trends in Neurosciences*, *41*(1), 31-46.

Knowlton, S., Joshi, A., Syrrist, P., Coskun, A. F., & Tasoglu, S. (2017). 3D-printed smartphone-based point of care tool for fluorescence-and magnetophoresis-based cytometry. *Lab on a Chip*, *17*(16), 2839-2851.

Knowlton, S., Joshi, A., Yenilmez, B., Ozbolat, I. T., Chua, C. K., Khademhosseini, A., & Tasoglu, S. (2016). Advancing cancer research using bioprinting for tumor-on-a-chip platforms. *International Journal of Bioprinting*, *2*(2).

Knowlton, S., Onal, S., Yu, C. H., Zhao, J. J., & Tasoglu, S. (2015). Bioprinting for cancer research. *Trends in Biotechnology*, *33*(9), 504-513.

Knowlton, S., Sencan, I., Aytar, Y., Khoory, J., Heeney, M., Ghiran, I., & Tasoglu, S. (2015). Sickle cell detection using a smartphone. *Scientific Reports*, *5*, 15022.

Knowlton, S., & Tasoglu, S. (2016). A bioprinted liver-on-a-chip for drug screening applications. *Trends in Biotechnology*, *34*(9), 681-682.

Knowlton, S., Yenilmez, B., Anand, S., & Tasoglu, S. (2017). Photocrosslinking-based bioprinting: examining crosslinking schemes. *Bioprinting*, *5*, 10-18.

Knowlton, S., Yenilmez, B., & Tasoglu, S. (2016). Towards single-step biofabrication of organs on a chip via 3D printing. *Trends in Biotechnology*, *34*(9), 685-688.

Knowlton, S., Yu, C. H., Ersoy, F., Emadi, S., Khademhosseini, A., & Tasoglu, S. (2016). 3D-printed microfluidic chips with patterned, cell-laden hydrogel constructs. *Biofabrication*, *8*(2), 025019.

Knowlton, S., Yu, C. H., Jain, N., Ghiran, I. C., & Tasoglu, S. (2015). Smart-phone based magnetic levitation for measuring densities. *PloS One*, *10*(8), e0134400.

Knowlton, S. M., Sadasivam, M., & Tasoglu, S. (2015). Microfluidics for sperm research. *Trends in Biotechnology*, *33*(4), 221-229.

Kolluru, C., Williams, M., Chae, J., & Prausnitz, M. R. (2019). Recruitment and collection of dermal interstitial fluid using a microneedle patch. *Advanced healthcare materials*, *8*(3), 1801262.

Krieger, K. J., Bertollo, N., Dangol, M., Sheridan, J. T., Lowery, M. M., & O'Cearbhaill, E. D. (2019). Simple and customizable method for fabrication of high-aspect ratio microneedle molds using low-cost 3D printing. *Microsystems & nanoengineering*, *5*(1), 1-14.

Krieger, K. J., Bertollo, N., Dangol, M., Sheridan, J. T., Lowery, M. M., & O'Cearbhaill, E. D. (2019). Simple and customizable method for fabrication of high-aspect ratio microneedle molds using low-cost 3D printing. *Microsystems & Nanoengineering*, *5*(1), 42. https://doi.org/10.1038/s41378-019-0088-8

Krieger, K. J., Liegey, J., Cahill, E. M., Bertollo, N., Lowery, M. M., & O'Cearbhaill, E. D. (2020). Development and Evaluation of 3D-Printed Dry Microneedle Electrodes for Surface Electromyography. *Advanced Materials Technologies*, 2000518.

Kusama, S., Sato, K., Matsui, Y., Kimura, N., Abe, H., Yoshida, S., & Nishizawa, M. (2021). Transdermal electroosmotic flow generated by a porous microneedle array patch. *Nature Communications*, *12*(1), 658. https://doi.org/10.1038/s41467-021-20948-4

Lambert, P. H., & Laurent, P. E. (2008). Intradermal vaccine delivery: Will new delivery systems transform vaccine administration? *Vaccine*, *26*(26), 3197-3208. https://doi.org/https://doi.org/10.1016/j.vaccine.2008.03.095

Lee, J.-Y., An, J., & Chua, C. K. (2017). Fundamentals and applications of 3D printing for novel materials. *Applied Materials Today*, *7*, 120-133. https://doi.org/https://doi.org/10.1016/j.apmt.2017.02.004

Lee, K.-S., Kim, R. H., Prabhakaran, P., Yang, D.-Y., Lim, T. W., & Park, S. H. (2007). Two-photon stereolithography. *Journal of Nonlinear Optical Physics & Materials*, *16*(01), 59-73.

Lee, K. J., Jeong, S. S., Roh, D. H., Kim, D. Y., Choi, H.-K., & Lee, E. H. (2020). A practical guide to the development of microneedle systems–In clinical trials or on the market. *International Journal of Pharmaceutics*, *573*, 118778.

Lepowsky, E., & Tasoglu, S. (2018). 3D printing for drug manufacturing: A perspective on the future of pharmaceuticals. *International Journal of Bioprinting*, *4*(1).

Li, C., Guan, G., Reif, R., Huang, Z., & Wang, R. K. (2012). Determining elastic properties of skin by measuring surface waves from an impulse mechanical stimulus using phase-sensitive optical coherence tomography. *Journal of The Royal Society Interface*, *9*(70), 831-841. https://doi.org/doi:10.1098/rsif.2011.0583

Li, C. G., Dangol, M., Lee, C. Y., Jang, M., & Jung, H. (2015). A self-powered one-touch blood extraction system: a novel polymer-capped hollow microneedle integrated with a pre-vacuum actuator. *Lab on a Chip*, *15*(2), 382-390.

Li, C. G., Lee, C. Y., Lee, K., & Jung, H. (2013). An optimized hollow microneedle for minimally invasive blood extraction. *Biomedical microdevices*, *15*(1), 17-25.

Li, C. G., Lee, K., Lee, C. Y., Dangol, M., & Jung, H. (2012). A Minimally Invasive Blood-Extraction System: Elastic Self-Recovery Actuator Integrated with an Ultrahigh-Aspect-Ratio Microneedle. *Advanced materials*, *24*(33), 4583-4586.

Li, J., Liu, B., Zhou, Y., Chen, Z., Jiang, L., Yuan, W., & Liang, L. (2017). Fabrication of a Ti porous microneedle array by metal injection molding for transdermal drug delivery. *PloS One*, *12*(2).

Li, W., Terry, R. N., Tang, J., Feng, M. R., Schwendeman, S. P., & Prausnitz, M. R. (2019). Rapidly separable microneedle patch for the sustained release of a contraceptive. *Nature Biomedical Engineering*, *3*(3), 220-229.

Li, Y., Zhang, H., Yang, R., Laffitte, Y., Schmill, U., Hu, W., Kaddoura, M., Blondeel, E. J. M., & Cui, B. (2019). Fabrication of sharp silicon hollow microneedles by deep-reactive ion etching towards minimally invasive diagnostics. *Microsystems & Nanoengineering*, *5*(1), 41. https://doi.org/10.1038/s41378-019-0077-y

Liao, Z., Li, D., Wang, X., Li, L., & Zou, Q. (2018). Cancer Diagnosis Through IsomiR Expression with Machine Learning Method. *Current Bioinformatics*, *13*(1), 57-63. https://doi.org/10.2174/1574893611666160609081155

Lightman, S., Hurvitz, G., Gvishi, R., & Arie, A. (2017). Miniature wide-spectrum mode sorter for vortex beams produced by 3D laser printing. *Optica*, *4*(6), 605-610.

Ligon, S. C., Liska, R., Stampfl, J. r., Gurr, M., & Mülhaupt, R. (2017). Polymers for 3D printing and customized additive manufacturing. *Chemical Reviews*, *117*(15), 10212-10290.

Lim, J., Tahk, D., Yu, J., Min, D.-H., & Jeon, N. L. (2018). Design rules for a tunable merged-tip microneedle. *Microsystems & nanoengineering*, *4*(1), 1-10.

Lim, S. H., Ng, J. Y., & Kang, L. (2017). Three-dimensional printing of a microneedle array on personalized curved surfaces for dual-pronged treatment of trigger finger. *Biofabrication*, *9*(1), 015010.

Lin, Y.-H., Lee, I.-C., Hsu, W.-C., Hsu, C.-H., Chang, K.-P., & Gao, S.-S. (2016). Rapid fabrication method of a microneedle mold with controllable needle height and width. *Biomedical Microdevices*, *18*(5), 85.

Liu, W., Zhong, Z., Hu, N., Zhou, Y., Maggio, L., Miri, A. K., Fragasso, A., Jin, X., Khademhosseini, A., & Zhang, Y. S. (2018). Coaxial extrusion bioprinting of 3D microfibrous constructs with cell-favorable gelatin methacryloyl microenvironments. *Biofabrication*, *10*(2), 024102.

Liu, Z., Mao, H., Wu, C.-Y., Feichtenhofer, C., Darrell, T., & Xie, S. (2022). A ConvNet for the 2020s. *arXiv preprint arXiv:2201.03545*.

Loizidou, E. Z., Inoue, N. T., Ashton-Barnett, J., Barrow, D. A., & Allender, C. J. (2016). Evaluation of geometrical effects of microneedles on skin penetration by CT scan and finite element analysis. *European journal of pharmaceutics and biopharmaceutics*, *107*, 1-6.

Lu, Y., Mantha, S. N., Crowder, D. C., Chinchilla, S., Shah, K. N., Yun, Y. H., Wicker, R. B., & Choi, J.-W. (2015). Microstereolithography and characterization of poly (propylene fumarate)-based drug-loaded microneedle arrays. *Biofabrication*, *7*(4), 045001.

Luzuriaga, M. A., Berry, D. R., Reagan, J. C., Smaldone, R. A., & Gassensmith, J. J. (2018). Biodegradable 3D printed polymer microneedles for transdermal drug delivery. *Lab on a Chip*, *18*(8), 1223-1230.

Ma, Y., Wang, W., He, M., Liu, Y., Li, C., Zhong, Y., Bu, Q., Huang, D., Qian, H., & Chen, W. (2024). PVA-based bulk microneedles capable of high insulin loading and pH-triggered degradation for multi-responsive and sustained hypoglycemic therapy [10.1039/D3BM01760E]. *Biomaterials Science*, *12*(2), 507-517. https://doi.org/10.1039/D3BM01760E

Makvandi, P., Kirkby, M., Hutton, A. R. J., Shabani, M., Yiu, C. K. Y., Baghbantaraghdari, Z., Jamaledin, R., Carlotti, M., Mazzolai, B., Mattoli, V., & Donnelly, R. F. (2021). Engineering Microneedle Patches for Improved Penetration: Analysis, Skin Models and Factors Affecting Needle Insertion. *Nano-Micro Letters*, *13*(1), 93. https://doi.org/10.1007/s40820-021-00611-9

Mansor, N. H. A., Markom, M. A., Tan, E. S. M. M., & Adom, A. H. (2019). Design and Fabrication of Biodegradable Microneedle Using 3D Rapid Prototyping Printer. Journal of Physics: Conference Series,

Mazzoli, A. (2013). Selective laser sintering in biomedical engineering. *Medical & Biological Engineering & Computing*, *51*(3), 245-256.

McAllister, D. V., Wang, P. M., Davis, S. P., Park, J.-H., Canatella, P. J., Allen, M. G., & Prausnitz, M. R. (2003). Microfabricated needles for transdermal delivery of macromolecules and nanoparticles: fabrication methods and transport studies. *Proceedings of the National Academy of Sciences*, *100*(24), 13755-13760.

Mikszta, J. A., Alarcon, J. B., Brittingham, J. M., Sutter, D. E., Pettis, R. J., & Harvey, N. G. (2002). Improved genetic immunization via micromechanical disruption of skin-barrier function and targeted epidermal delivery. *Nature Medicine*, *8*(4), 415-419.

Miller, P. R., Taylor, R. M., Tran, B. Q., Boyd, G., Glaros, T., Chavez, V. H., Krishnakumar, R., Sinha, A., Poorey, K., Williams, K. P., Branda, S. S., Baca, J. T., & Polsky, R. (2018). Extraction and biomolecular analysis of dermal interstitial fluid collected with hollow microneedles. *Communications Biology*, *1*(1), 173. https://doi.org/10.1038/s42003-018-0170-z

Mishra, R. K., Mohan, A. V., Soto, F., Chrostowski, R., & Wang, J. (2017). A microneedle biosensor for minimally-invasive transdermal detection of nerve agents. *Analyst*, *142*(6), 918-924.

Miyano, T., Tobinaga, Y., Kanno, T., Matsuzaki, Y., Takeda, H., Wakui, M., & Hanada, K. (2005). Sugar micro needles as transdermic drug delivery system. *Biomedical Microdevices*, *7*(3), 185-188.

Mohri, M., Rostamizadeh, A., & Talwalkar, A. (2018). *Foundations of machine learning*. MIT press.

Mojeiko, G., de Brito, M., Salata, G. C., & Lopes, L. B. (2019). Combination of microneedles and microemulsions to increase celecoxib topical delivery for potential application in chemoprevention of breast cancer. *International Journal of Pharmaceutics*, *560*, 365-376.

Morde, R. S. (2018). *Micro-3D printing of bio-inspired microneedle with enhanced adhesion capabilities* Rutgers University-School of Graduate Studies].

Moreira, A. F., Rodrigues, C. F., Jacinto, T. A., Miguel, S. P., Costa, E. C., & Correia, I. J. (2019). Microneedle-based delivery devices for cancer therapy: A review.

Pharmacological Research, *148*, 104438. https://doi.org/https://doi.org/10.1016/j.phrs.2019.104438

Moussi, K., Bukhamsin, A., Hidalgo, T., & Kosel, J. (2020). Biocompatible 3D Printed Microneedles for Transdermal, Intradermal, and Percutaneous Applications. *Advanced Engineering Materials*, *22*(2), 1901358.

Mukerjee, E., Collins, S., Isseroff, R. R., & Smith, R. (2004). Microneedle array for transdermal biological fluid extraction and in situ analysis. *Sensors and Actuators A: Physical*, *114*(2-3), 267-275.

Muñiz Castro, B., Elbadawi, M., Ong, J. J., Pollard, T., Song, Z., Gaisford, S., Pérez, G., Basit, A. W., Cabalar, P., & Goyanes, A. (2021). Machine learning predicts 3D printing performance of over 900 drug delivery systems. *Journal of Controlled Release*, *337*, 530-545. https://doi.org/https://doi.org/10.1016/j.jconrel.2021.07.046

Nagarkar, R., Singh, M., Nguyen, H. X., & Jonnalagadda, S. (2020). A review of recent advances in microneedle technology for transdermal drug delivery. *Journal of Drug Delivery Science and Technology*, 101923.

NASA. (1995). *Man-Systems Integration Standards, Revision B*. NASA. Retrieved Access Date: 02/15/2022 from msis.jsc.nasa.gov/sections/section04.htm

Nejad, H. R., Sadeqi, A., Kiaee, G., & Sonkusale, S. (2018a). Low-cost and cleanroom-free fabrication of microneedles. *Microsystems & Nanoengineering*, *4*(1), 1-7.

Nejad, H. R., Sadeqi, A., Kiaee, G., & Sonkusale, S. (2018b). Low-cost and cleanroom-free fabrication of microneedles. *Microsystems & Nanoengineering*, *4*(1), 17073. https://doi.org/10.1038/micronano.2017.73

Netea, R., Lenders, J., Smits, P., & Thien, T. (2003). Both body and arm position significantly influence blood pressure measurement. *Journal of human hypertension*, *17*(7), 459-462.

Ngo, T. D., Kashani, A., Imbalzano, G., Nguyen, K. T. Q., & Hui, D. (2018). Additive manufacturing (3D printing): A review of materials, methods, applications and challenges. *Composites Part B: Engineering*, *143*, 172-196. https://doi.org/https://doi.org/10.1016/j.compositesb.2018.02.012

Ni, G., Ge, X., Liu, L., Zhang, J., Wang, X., Liu, J., Liu, L., & Liu, Y. (2020). Towards Indicating Human Skin State In Vivo Using Geometry-Dependent Spectroscopic Contrast Imaging. *IEEE Photonics Technology Letters*, *32*(12), 697-700.

Nicholas, D., Logan, K. A., Sheng, Y., Gao, J., Farrell, S., Dixon, D., Callan, B., McHale, A. P., & Callan, J. F. (2018a). Rapid paper based colorimetric detection of glucose using a hollow microneedle device. *International Journal of Pharmaceutics*, *547*(1-2), 244-249.

Nicholas, D., Logan, K. A., Sheng, Y., Gao, J., Farrell, S., Dixon, D., Callan, B., McHale, A. P., & Callan, J. F. (2018b). Rapid paper based colorimetric detection of glucose using a hollow microneedle device. *International Journal of Pharmaceutics*, *547*(1), 244-249. https://doi.org/https://doi.org/10.1016/j.ijpharm.2018.06.002

Norman, J. J., Arya, J. M., McClain, M. A., Frew, P. M., Meltzer, M. I., & Prausnitz, M. R. (2014). Microneedle patches: Usability and acceptability for self-vaccination against influenza. *Vaccine*, *32*(16), 1856-1862. https://doi.org/https://doi.org/10.1016/j.vaccine.2014.01.076

Ochoa, M., Zhou, J., Rahimi, R., Badwaik, V., Thompson, D., & Ziaie, B. (2015, 21-25 June 2015). Rapid 3D-print-and-shrink fabrication of biodegradable microneedles with complex geometries. 2015 Transducers - 2015 18th

International Conference on Solid-State Sensors, Actuators and Microsystems (TRANSDUCERS),

Oh, N. G., Hwang, S. Y., & Na, Y. H. (2022). Fabrication of a PVA-Based Hydrogel Microneedle Patch. *ACS Omega*, *7*(29), 25179-25185. https://doi.org/10.1021/acsomega.2c01993

Olatunji, O., Das, D. B., Garland, M. J., Belaid, L., & Donnelly, R. F. (2013). Influence of Array Interspacing on the Force Required for Successful Microneedle Skin Penetration: Theoretical and Practical Approaches. *Journal of Pharmaceutical Sciences*, *102*(4), 1209-1221. https://doi.org/https://doi.org/10.1002/jps.23439

Osareh, A., & Shadgar, B. (2010, 20-22 April 2010). Machine learning techniques to diagnose breast cancer. 2010 5th International Symposium on Health Informatics and Bioinformatics,

Ostchega, Y. (2011). *Resting pulse rate reference data for children, adolescents, and adults: United States, 1999-2008*. US Department of Health and Human Services, Centers for Disease Control and Prevention, National Center for Health Statistics.

Paré, G., Sicotte, C., & Jacques, H. (2006). The effects of creating psychological ownership on physicians' acceptance of clinical information systems. *Journal of the American Medical Informatics Association*, *13*(2), 197-205.

Park, C., Kim, M. H., Hong, S. M., Go, J. S., & Shin, B. S. (2015). A study on the comparison mechanical properties of 3D printing prototypes with laminating direction. *Journal of the Korean Society of Manufacturing Technology Engineers*, *24*(3), 334-341.

Park, Y.-H., Ha, S. K., Choi, I., Kim, K. S., Park, J., Choi, N., Kim, B., & Sung, J. H. (2016). Fabrication of degradable carboxymethyl cellulose (CMC) microneedle with laser writing and replica molding process for enhancement of transdermal drug delivery. *Biotechnology and bioprocess engineering*, *21*(1), 110-118.

Paszke, A., Gross, S., Massa, F., Lerer, A., Bradbury, J., Chanan, G., Killeen, T., Lin, Z., Gimelshein, N., & Antiga, L. (2019). Pytorch: An imperative style, high-performance deep learning library. *Advances in neural information processing systems*, *32*.

Paul, R., Saville, A. C., Hansel, J. C., Ye, Y., Ball, C., Williams, A., Chang, X., Chen, G., Gu, Z., Ristaino, J. B., & Wei, Q. (2019). Extraction of Plant DNA by Microneedle Patch for Rapid Detection of Plant Diseases. *ACS Nano*, *13*(6), 6540-6549. https://doi.org/10.1021/acsnano.9b00193

Pedregosa, F., Varoquaux, G., Gramfort, A., Michel, V., Thirion, B., Grisel, O., Blondel, M., Prettenhofer, P., Weiss, R., & Dubourg, V. (2011). Scikit-learn: Machine learning in Python. *the Journal of machine Learning research*, *12*, 2825-2830.

Pere, C. P. P., Economidou, S. N., Lall, G., Ziraud, C., Boateng, J. S., Alexander, B. D., Lamprou, D. A., & Douroumis, D. (2018). 3D printed microneedles for insulin skin delivery. *International Journal of Pharmaceutics*, *544*(2), 425-432.

Pistor, M. L. P. (1975). Device for cutaneous therapeutic treatment. In: Google Patents.

Potluri, V., Kathiresan, P. S., Kandula, H., Thirumalaraju, P., Kanakasabapathy, M. K., Pavan, S. K. S., Yarravarapu, D., Soundararajan, A., Baskar, K., Gupta, R., Gudipati, N., Petrozza, J. C., & Shafiee, H. (2018). An inexpensive smartphone-based device for point-of-care ovulation testing. https://doi.org/10.1039/C8LC00792F

Prausnitz, M. R. (2004). Microneedles for transdermal drug delivery. *Advanced Drug Delivery Reviews*, *56*(5), 581-587. https://doi.org/https://doi.org/10.1016/j.addr.2003.10.023

Prausnitz, M. R., & Langer, R. (2008). Transdermal drug delivery. *Nature Biotechnology*, *26*(11), 1261-1268. https://doi.org/10.1038/nbt.1504

Quan, H., Zhang, T., Xu, H., Luo, S., Nie, J., & Zhu, X. (2020). Photo-curing 3D printing technique and its challenges. *Bioactive Materials*, *5*(1), 110-115.

Queiroz, M. L. B., Shanmugam, S., Santos, L. N. S., Campos, C. d. A., Santos, A. M., Batista, M. S., Araújo, A. A. d. S., & Serafini, M. R. (2020). Microneedles as an alternative technology for transdermal drug delivery systems: a patent review. *Expert Opinion on Therapeutic Patents*, *30*(6), 433-452.

Rad, Z. F., Nordon, R. E., Anthony, C. J., Bilston, L., Prewett, P. D., Arns, J.-Y., Arns, C. H., Zhang, L., & Davies, G. J. (2017). High-fidelity replication of thermoplastic microneedles with open microfluidic channels. *Microsystems & nanoengineering*, *3*(1), 1-11.

Rahmani Dabbagh, S., Rezapour Sarabi, M., Birtek, M. T., Mustafaoglu, N., Zhang, Y. S., & Tasoglu, S. (2022). 3D bioprinted organ-on-chips. *Aggregate*, *n/a*(n/a), e197. https://doi.org/https://doi.org/10.1002/agt2.197

Rajeswari, N. R., & Malliga, P. (2013). Microfluidic system using microneedles for targeted drug delivery in cancer therapy. International Conference on Smart Structures and Systems-ICSSS'13,

Ranschaert, E. R., Morozov, S., & Algra, P. R. (2019). *Artificial intelligence in medical imaging: opportunities, applications and risks*. Springer.

Ren, L., Jiang, Q., Chen, Z., Chen, K., Xu, S., Gao, J., & Jiang, L. (2017). Flexible microneedle array electrode using magnetorheological drawing lithography for bio-signal monitoring. *Sensors and Actuators A: Physical*, *268*, 38-45. https://doi.org/https://doi.org/10.1016/j.sna.2017.10.042

Rezapour Sarabi, M., Jiang, N., Ozturk, E., Yetisen, A. K., & Tasoglu, S. (2021). Biomedical optical fibers [10.1039/D0LC01155J]. *Lab on a Chip*, *21*(4), 627-640. https://doi.org/10.1039/D0LC01155J

Russell, L. M., Wiedersberg, S., & Delgado-Charro, M. B. (2008). The determination of stratum corneum thickness: an alternative approach. *European journal of pharmaceutics and biopharmaceutics : official journal of Arbeitsgemeinschaft fur Pharmazeutische Verfahrenstechnik e.V*, *69*(3), 861-870. https://doi.org/10.1016/j.ejpb.2008.02.002

S.B.V.J, C., & Mannayee, G. (2022). Structural analysis and simulation of solid microneedle array for vaccine delivery applications. *Materials Today: Proceedings*, *65*, 3774-3779. https://doi.org/https://doi.org/10.1016/j.matpr.2022.06.483

Safi, S., Thiessen, T., & Schmailzl, K. J. (2018). Acceptance and resistance of new digital technologies in medicine: qualitative study. *JMIR research protocols*, *7*(12), e11072.

Samant, P. P., Niedzwiecki, M. M., Raviele, N., Tran, V., Mena-Lapaix, J., Walker, D. I., Felner, E. I., Jones, D. P., Miller, G. W., & Prausnitz, M. R. (2020). Sampling interstitial fluid from human skin using a microneedle patch. *Science Translational Medicine*, *12*(571), eaaw0285. https://doi.org/10.1126/scitranslmed.aaw0285

Samant, P. P., & Prausnitz, M. R. (2018). Mechanisms of sampling interstitial fluid from skin using a microneedle patch. *Proceedings of the National Academy of Sciences*, *115*(18), 4583-4588.

Sandler, M., Howard, A., Zhu, M., Zhmoginov, A., & Chen, L.-C. (2018). Mobilenetv2: Inverted residuals and linear bottlenecks. Proceedings of the IEEE conference on computer vision and pattern recognition,

Sarabi, M. R., Ahmadpour, A., Yetisen, A. K., & Tasoglu, S. (2021). Finger-Actuated Microneedle Array for Sampling Body Fluids. *Applied Sciences*, *11*(12), 5329. https://www.mdpi.com/2076-3417/11/12/5329

Sarabi, M. R., Alseed, M. M., Karagoz, A. A., & Tasoglu, S. (2022). Machine Learning-Enabled Prediction of 3D-Printed Microneedle Features. *Biosensors-Basel*, *12*(7). https://doi.org/ARTN 491

10.3390/bios12070491

Sarabi, M. R., Bediz, B., Falo, L. D., Korkmaz, E., & Tasoglu, S. (2021). 3D printing of microneedle arrays: challenges towards clinical translation. *Journal of 3D Printing in Medicine*. https://doi.org/10.2217/3dp-2021-0010

Sarabi, M. R., Yetisen, A. K., & Tasoglu, S. (2022). Magnetic levitation for space exploration. *Trends in biotechnology*. https://doi.org/https://doi.org/10.1016/j.tibtech.2022.03.010

Sarlo, R., & Tarazaga, P. A. (2016). A neural network approach to 3D printed surrogate systems. In *Topics in Modal Analysis & Testing, Volume 10* (pp. 215-222). Springer.

Sears, N. A., Seshadri, D. R., Dhavalikar, P. S., & Cosgriff-Hernandez, E. (2016). A Review of Three-Dimensional Printing in Tissue Engineering. *Tissue Engineering Part B: Reviews*, *22*(4), 298-310. https://doi.org/10.1089/ten.teb.2015.0464

Semin, J. N., Palm, D., Smith, L. M., & Ruttle, S. (2020). Understanding breast cancer survivors' financial burden and distress after financial assistance. *Supportive Care in Cancer*, 1-8.

Sequeira, A., & Janela, J. (2007). An overview of some mathematical models of blood rheology. *A Portrait of State-of-the-Art Research at the Technical University of Lisbon*, 65-87.

Serex, L., Bertsch, A., & Renaud, P. (2018). Microfluidics: A new layer of control for extrusion-based 3D printing. *Micromachines*, *9*(2), 86.

Shahrubudin, N., Lee, T. C., & Ramlan, R. (2019). An Overview on 3D Printing Technology: Technological, Materials, and Applications. *Procedia Manufacturing*, *35*, 1286-1296. https://doi.org/https://doi.org/10.1016/j.promfg.2019.06.089

Shi, Y., Zhang, Y., Baek, S., De Backer, W., & Harik, R. (2018). Manufacturability analysis for additive manufacturing using a novel feature recognition technique. *Computer-Aided Design and Applications*, *15*(6), 941-952. https://doi.org/10.1080/16864360.2018.1462574

Son, D., Liimatainen, V., & Sitti, M. (2021). Machine Learning-Based and Experimentally Validated Optimal Adhesive Fibril Designs. *Small*, *17*(39), 2102867. https://doi.org/https://doi.org/10.1002/smll.202102867

Sukhov, A., Adamopoulos, I. E., & Maverakis, E. (2016). Interactions of the Immune System with Skin and Bone Tissue in Psoriatic Arthritis: A Comprehensive Review. *Clinical Reviews in Allergy & Immunology*, *51*(1), 87-99. https://doi.org/10.1007/s12016-016-8529-8

Sullivan, S. P., Koutsonanos, D. G., del Pilar Martin, M., Lee, J. W., Zarnitsyn, V., Choi, S.-O., Murthy, N., Compans, R. W., Skountzou, I., & Prausnitz, M. R. (2010). Dissolving polymer microneedle patches for influenza vaccination. *Nature medicine*, *16*(8), 915-920.

Tabriz, A. G., Douroumis, D., & Boateng, J. (2020). 3D printed scaffolds for wound healing and tissue regeneration. *Therapeutic Dressings and Wound Healing Applications*, 385-398.

Takeuchi, K., Takama, N., Kim, B., Sharma, K., Paul, O., & Ruther, P. (2019a). Microfluidic chip to interface porous microneedles for ISF collection. *Biomedical microdevices*, *21*(1), 1-10.

Takeuchi, K., Takama, N., Kim, B., Sharma, K., Paul, O., & Ruther, P. (2019b). Microfluidic chip to interface porous microneedles for ISF collection. *Biomedical Microdevices*, *21*(1), 28.

Tan, R., Yang, X., Lu, H., Yang, L., Zhang, T., Miao, J., Feng, Y., & Shen, Y. (2022). Nanofiber-based biodegradable millirobot with controllable anchoring and adaptive stepwise release functions. *Matter*, *5*(4), 1277-1295.

Tasoglu, S. (2022). Toilet-based continuous health monitoring using urine. *Nature Reviews Urology*, *19*(4), 219-230. https://doi.org/10.1038/s41585-021-00558-x

Tasoglu, S., & Demirci, U. (2013). Bioprinting for stem cell research. *Trends in Biotechnology*, *31*(1), 10-19.

Taylor, R. M., Maharjan, D., Moreu, F., & Baca, J. T. (2020a). Parametric study of 3D printed microneedle (MN) holders for interstitial fluid (ISF) extraction. *Microsystem Technologies*, *26*(6), 2067-2073.

Taylor, R. M., Maharjan, D., Moreu, F., & Baca, J. T. (2020b). Parametric study of 3D printed microneedle (MN) holders for interstitial fluid (ISF) extraction. *Microsystem Technologies*, 1-7.

Taylor, R. M., Miller, P. R., Ebrahimi, P., Polsky, R., & Baca, J. T. (2018). Minimally-invasive, microneedle-array extraction of interstitial fluid for comprehensive biomedical applications: transcriptomics, proteomics, metabolomics, exosome research, and biomarker identification. *Laboratory animals*, *52*(5), 526-530.

Tejavibulya, N., Colburn, D. A., Marcogliese, F. A., Yang, K.-A., Guo, V., Chowdhury, S., Stojanovic, M. N., & Sia, S. K. (2019). Hydrogel Microfilaments toward Intradermal Health Monitoring. *Iscience*, *21*, 328-340.

Teymourian, H., Tehrani, F., Mahato, K., & Wang, J. (2021). Lab under the Skin: Microneedle Based Wearable Devices. *Advanced healthcare materials*, 2002255.

Tran, K. T., Gavitt, T. D., Farrell, N. J., Curry, E. J., Mara, A. B., Patel, A., Brown, L., Kilpatrick, S., Piotrowska, R., & Mishra, N. (2020). Transdermal microneedles for the programmable burst release of multiple vaccine payloads. *Nature Biomedical Engineering*, 1-10.

Tran, K. T., Gavitt, T. D., Le, T. T., Graichen, A., Lin, F., Liu, Y., Tulman, E. R., Szczepanek, S. M., & Nguyen, T. D. (2023). A Single-Administration Microneedle Skin Patch for Multi-Burst Release of Vaccine against SARS-CoV-2. *Advanced Materials Technologies*, *8*(3), 2200905.

Tran, K. T. M., Gavitt, T. D., Farrell, N. J., Curry, E. J., Mara, A. B., Patel, A., Brown, L., Kilpatrick, S., Piotrowska, R., Mishra, N., Szczepanek, S. M., & Nguyen, T. D. (2021). Transdermal microneedles for the programmable burst release of multiple vaccine payloads. *Nature Biomedical Engineering*, *5*(9), 998-1007. https://doi.org/10.1038/s41551-020-00650-4

Uddin, M. J., Scoutaris, N., Economidou, S. N., Giraud, C., Chowdhry, B. Z., Donnelly, R. F., & Douroumis, D. (2020). 3D printed microneedles for anticancer therapy of skin tumours. *Materials Science and Engineering: C*, *107*, 110248.

Van Der Walt, S., Colbert, S. C., & Varoquaux, G. (2011). The NumPy array: a structure for efficient numerical computation. *Computing in science & engineering*, *13*(2), 22-30.

Vincze, G., Barner, J. C., & Lopez, D. (2004). Factors Associated With Adherence to Self-Monitoring of Blood Glucose Among Persons With Diabetes. *The Diabetes Educator*, *30*(1), 112-125. https://doi.org/10.1177/014572170403000119

Wang, D., Wang, T., Liu, J., Yu, H., Jiao, S., Feng, B., Zhou, F., Fu, Y., Yin, Q., & Zhang, P. (2016). Acid-activatable versatile micelleplexes for PD-L1 blockade-enhanced cancer photodynamic immunotherapy. *Nano Letters*, *16*(9), 5503-5513.

Wang, P. M., Cornwell, M., & Prausnitz, M. R. (2005). Minimally invasive extraction of dermal interstitial fluid for glucose monitoring using microneedles. *Diabetes Technology & Therapeutics*, *7*(1), 131-141.

Wang, R., Jiang, X., Wang, W., & Li, Z. (2017). A microneedle electrode array on flexible substrate for long-term EEG monitoring. *Sensors and Actuators B: Chemical*, *244*, 750-758. https://doi.org/https://doi.org/10.1016/j.snb.2017.01.052

Wang, Z., Luan, J., Seth, A., Liu, L., You, M., Gupta, P., Rathi, P., Wang, Y., Cao, S., Jiang, Q., Zhang, X., Gupta, R., Zhou, Q., Morrissey, J. J., Scheller, E. L., Rudra, J. S., & Singamaneni, S. (2021). Microneedle patch for the ultrasensitive quantification of protein biomarkers in interstitial fluid. *Nature Biomedical Engineering*, *5*(1), 64-76. https://doi.org/10.1038/s41551-020-00672-y

Wen, D., Khan, S. M., Xu, A. J., Ibrahim, H., Smith, L., Caballero, J., Zepeda, L., de Blas Perez, C., Denniston, A. K., & Liu, X. (2022). Characteristics of publicly available skin cancer image datasets: a systematic review. *The Lancet Digital Health*, *4*(1), e64-e74.

World Economic Forum Top 10 Emerging Technologies (www.weforum.org/reports/top-10-emerging-technologies-2020). (2020). W. E. Forum. weforum.org/reports/top-10-emerging-technologies-2020

Wu, L., Shrestha, P., Iapichino, M., Cai, Y., Kim, B., & Stoeber, B. (2021). Characterization method for calculating diffusion coefficient of drug from polylactic acid (PLA) microneedles into the skin. *Journal of Drug Delivery Science and Technology*, *61*, 102192. https://doi.org/https://doi.org/10.1016/j.jddst.2020.102192

Wu, M., Zhang, Y., Huang, H., Li, J., Liu, H., Guo, Z., Xue, L., Liu, S., & Lei, Y. (2020). Assisted 3D printing of microneedle patches for minimally invasive glucose control in diabetes. *Materials Science and Engineering: C*, 111299.

Xenikakis, I., Tzimtzimis, M., Tsongas, K., Andreadis, D., Demiri, E., Tzetzis, D., & Fatouros, D. G. (2019). Fabrication and finite element analysis of stereolithographic 3D printed microneedles for transdermal delivery of model dyes across human skin in vitro. *European Journal of Pharmaceutical Sciences*, *137*, 104976.

Xie, J., Huang, S., Huang, H., Deng, X., Yue, P., Lin, J., Yang, M., Han, L., & Zhang, D.-k. (2021). Advances in the Application of Natural Products and the Novel Drug Delivery Systems for Psoriasis [Review]. *Frontiers in pharmacology*, *12*. https://doi.org/10.3389/fphar.2021.644952

Xie, L., Zeng, H., Sun, J., & Qian, W. (2020). Engineering Microneedles for Therapy and Diagnosis: A Survey. *Micromachines*, *11*(3), 271. https://www.mdpi.com/2072-666X/11/3/271

Xu, N., Zhang, M., Xu, W., Ling, G., Yu, J., & Zhang, P. (2022). Swellable PVA/PVP hydrogel microneedle patches for the extraction of interstitial skin fluid toward minimally invasive monitoring of blood glucose level [10.1039/D1AN02288A]. *Analyst*, *147*(7), 1478-1491. https://doi.org/10.1039/D1AN02288A

Yang, B., Fang, X., & Kong, J. (2020). Engineered Microneedles for Interstitial Fluid Cell-Free DNA Capture and Sensing Using Iontophoretic Dual-Extraction Wearable Patch. *Advanced Functional Materials*, *30*(24), 2000591. https://doi.org/https://doi.org/10.1002/adfm.202000591

Yang, J., Li, Y., Ye, R., Zheng, Y., Li, X., Chen, Y., Xie, X., & Jiang, L. (2020). Smartphone-powered iontophoresis-microneedle array patch for controlled transdermal delivery. *Microsystems & nanoengineering*, *6*(1), 112. https://doi.org/10.1038/s41378-020-00224-z

Yang, J., Liu, X., Fu, Y., & Song, Y. (2019). Recent advances of microneedles for biomedical applications: drug delivery and beyond. *Acta Pharmaceutica Sinica B*, *9*(3), 469-483. https://doi.org/https://doi.org/10.1016/j.apsb.2019.03.007

Yao, W., Li, D., Zhao, Y., Zhan, Z., Jin, G., Liang, H., & Yang, R. (2020). 3D Printed Multi-Functional Hydrogel Microneedles Based on High-Precision Digital Light Processing. *Micromachines*, *11*(1), 17.

Yao, W., Li, Y., & Ding, G. (2012). Interstitial fluid flow: the mechanical environment of cells and foundation of meridians. *Evidence-Based Complementary and Alternative Medicine*, *2012*.

Yendeti, B., & Soma, V. R. (2020). Direct Fabrication of sub-100 nm Nanoneedles in Silver using Femtosecond Laser Direct Writing. *Defence Science Journal*, *70*(2), 197-200.

Yenilmez, B., Knowlton, S., & Tasoglu, S. (2016). Self-contained handheld magnetic platform for point of care cytometry in biological samples. *Advanced Materials Technologies*, *1*(9), 1600144.

Yenilmez, B., Knowlton, S., Yu, C. H., Heeney, M. M., & Tasoglu, S. (2016). Label-free sickle cell disease diagnosis using a low-cost, handheld platform. *Advanced Materials Technologies*, *1*(5), 1600100.

Yeung, C., Chen, S., King, B., Lin, H., King, K., Akhtar, F., Diaz, G., Wang, B., Zhu, J., & Sun, W. (2019). A 3D-printed microfluidic-enabled hollow microneedle architecture for transdermal drug delivery. *Biomicrofluidics*, *13*(6), 064125.

Yigci, D., Rezapour Sarabi, M., Ustun, M., Atceken, N., Sokullu, E., Onder, T. B., & Tasoglu, S. (2022). 3D Bioprinted Glioma Models. *Progress in Biomedical Engineering*. http://iopscience.iop.org/article/10.1088/2516-1091/ac7833

Yokoyama, M., Chihara, N., Tanaka, A., Katayama, Y., Taruya, A., Ishida, Y., Yuzaki, M., Honda, K., Nishimura, Y., Kondo, T., Akasaka, T., & Kato, N. (2020). A biodegradable microneedle sheet for intracorporeal topical hemostasis. *Scientific reports*, *10*(1), 18831. https://doi.org/10.1038/s41598-020-75894-w

Yosipovitch, G., Mills, K. C., Nattkemper, L. A., Feneran, A., Tey, H. L., Lowenthal, B. M., Pearce, D. J., Williford, P. M., Sangueza, O. P., & D'Agostino, R. B. (2014). Association of pain and itch with depth of invasion and inflammatory cell constitution in skin cancer: results of a large clinicopathologic study. *JAMA dermatology*, *150*(11), 1160-1166.

You, S., Li, J., Zhu, W., Yu, C., Mei, D., & Chen, S. (2018). Nanoscale 3D printing of hydrogels for cellular tissue engineering [10.1039/C8TB00301G]. *Journal of Materials Chemistry B*, *6*(15), 2187-2197. https://doi.org/10.1039/C8TB00301G

Yu, K.-H., Beam, A. L., & Kohane, I. S. (2018). Artificial intelligence in healthcare. *Nature Biomedical Engineering*, *2*(10), 719-731. https://doi.org/10.1038/s41551-018-0305-z

Yu, L. M., Tay, F. E. H., Guo, D. G., Xu, L., & Yap, K. L. (2009). A microfabricated electrode with hollow microneedles for ECG measurement. *Sensors and*

Actuators A: Physical, *151*(1), 17-22. https://doi.org/https://doi.org/10.1016/j.sna.2009.01.020

Zhang, J., Hu, Q., Wang, S., Tao, J., & Gou, M. (2020). Digital light processing based three-dimensional printing for medical applications. *International Journal of Bioprinting*, *6*(1).

Zhang, L., Yang, G., Johnson, B. N., & Jia, X. (2019). Three-dimensional (3D) printed scaffold and material selection for bone repair. *Acta Biomaterialia*, *84*, 16-33. https://doi.org/https://doi.org/10.1016/j.actbio.2018.11.039

Zhang, X., Chen, G., Bian, F., Cai, L., & Zhao, Y. (2019). Encoded microneedle arrays for detection of skin interstitial fluid biomarkers. *Advanced materials*, *31*(37), 1902825.

Zheng, M., Wang, Z., Chang, H., Wang, L., Chew, S. W. T., Lio, D. C. S., Cui, M., Liu, L., Tee, B. C. K., & Xu, C. (2020). Osmosis-Powered Hydrogel Microneedles for Microliters of Skin Interstitial Fluid Extraction within Minutes. *Advanced healthcare materials*, *9*(10), 1901683. https://doi.org/https://doi.org/10.1002/adhm.201901683

Zhu, J., Zhou, X., Kim, H. J., Qu, M., Jiang, X., Lee, K., Ren, L., Wu, Q., Wang, C., & Zhu, X. (2020). Gelatin methacryloyl microneedle patches for minimally invasive extraction of skin interstitial fluid. *Small*, *16*(16), 1905910.

Zhu, J., Zhou, X., Libanori, A., & Sun, W. (2020). Microneedle-based bioassays. *Nanoscale Advances*.

Ziesmer, J., Tajpara, P., Hempel, N.-J., Ehrström, M., Melican, K., Eidsmo, L., & Sotiriou, G. A. (2021). Vancomycin-Loaded Microneedle Arrays against Methicillin-Resistant Staphylococcus Aureus Skin Infections. *Advanced Materials Technologies*, *6*(7), 2001307. https://doi.org/https://doi.org/10.1002/admt.202001307

Zoudani, E. L., & Soltani, M. (2020). A new computational method of modeling and evaluation of dissolving microneedle for drug delivery applications: Extension to theoretical modeling of a novel design of microneedle (array in array) for efficient drug delivery. *European Journal of Pharmaceutical Sciences*, *150*, 105339. https://doi.org/https://doi.org/10.1016/j.ejps.2020.105339

Appendix

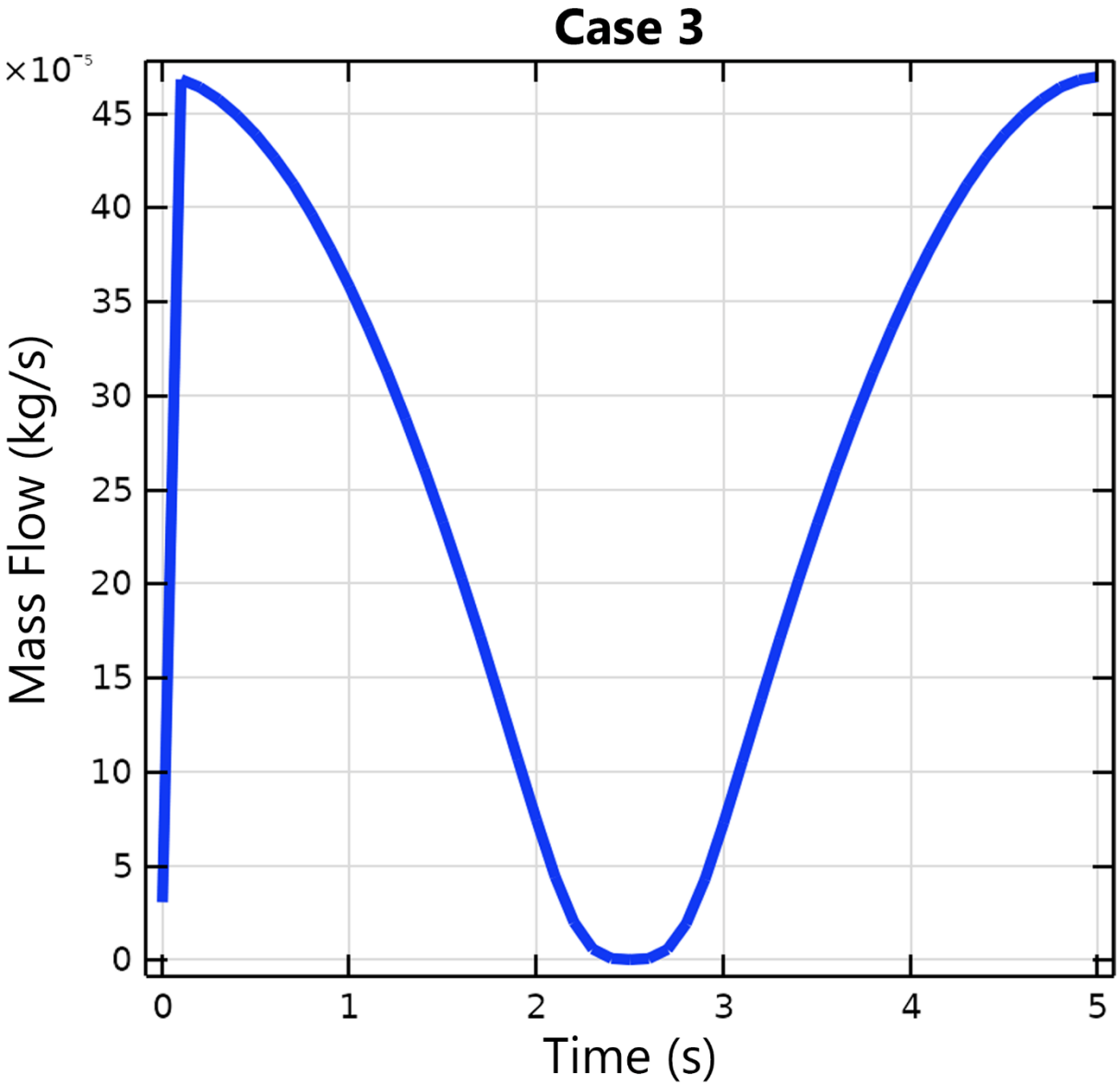

Supplementary Figure 3.S.1. Mass flow curve result at the reservoir for Case 3 in Table 3.3. The curve shows the mass flow rate in $kg.s^{-1}$ for time in seconds. Time duration is 5 s.

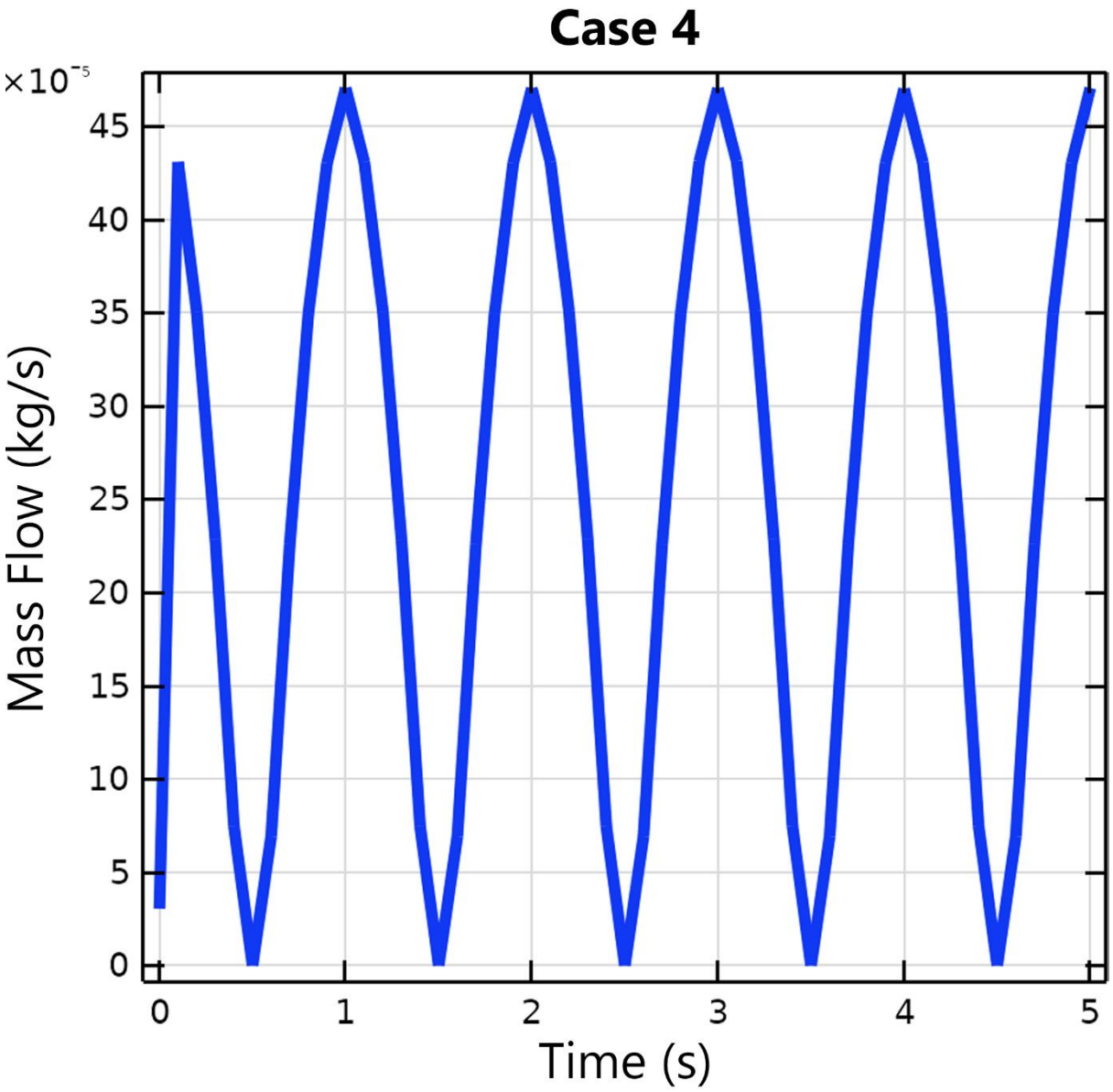

Supplementary Figure 3.S.2. Mass flow curve result at the reservoir for Case 4 in Table 3.3. The curve shows the mass flow rate in $kg.s^{-1}$ for time in seconds. Time duration is 5 s.

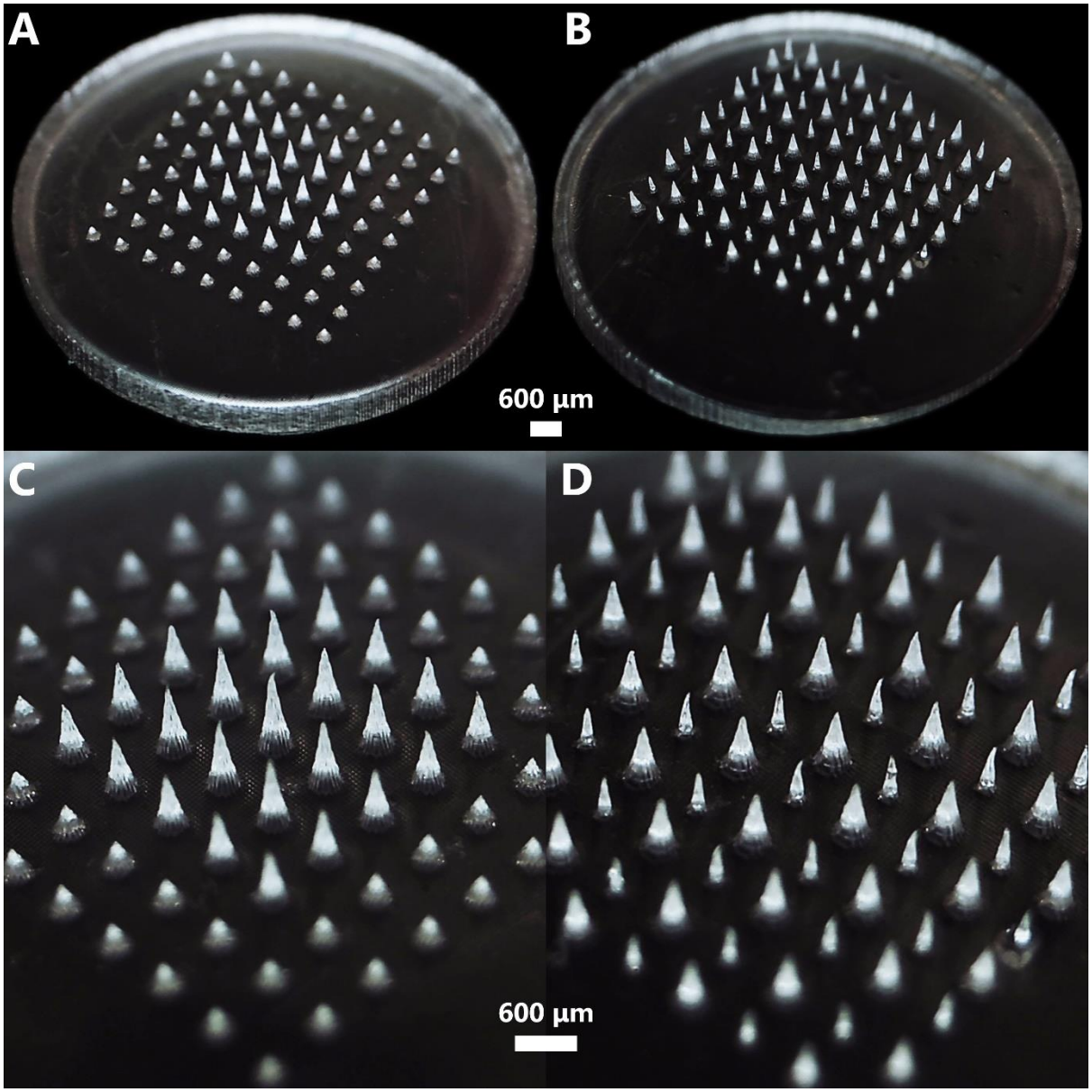

Supplementary Figure 5.S.1. Microscopy photos of the nonlinear MNAs. (A) The mountain design MNA under optical microscope. (B) The wave design MNA under optical microscope. (C) Needles' close up view for the mountain design. (D) Needles' close up view for the wave design. Scale bars for all = 600 µm.

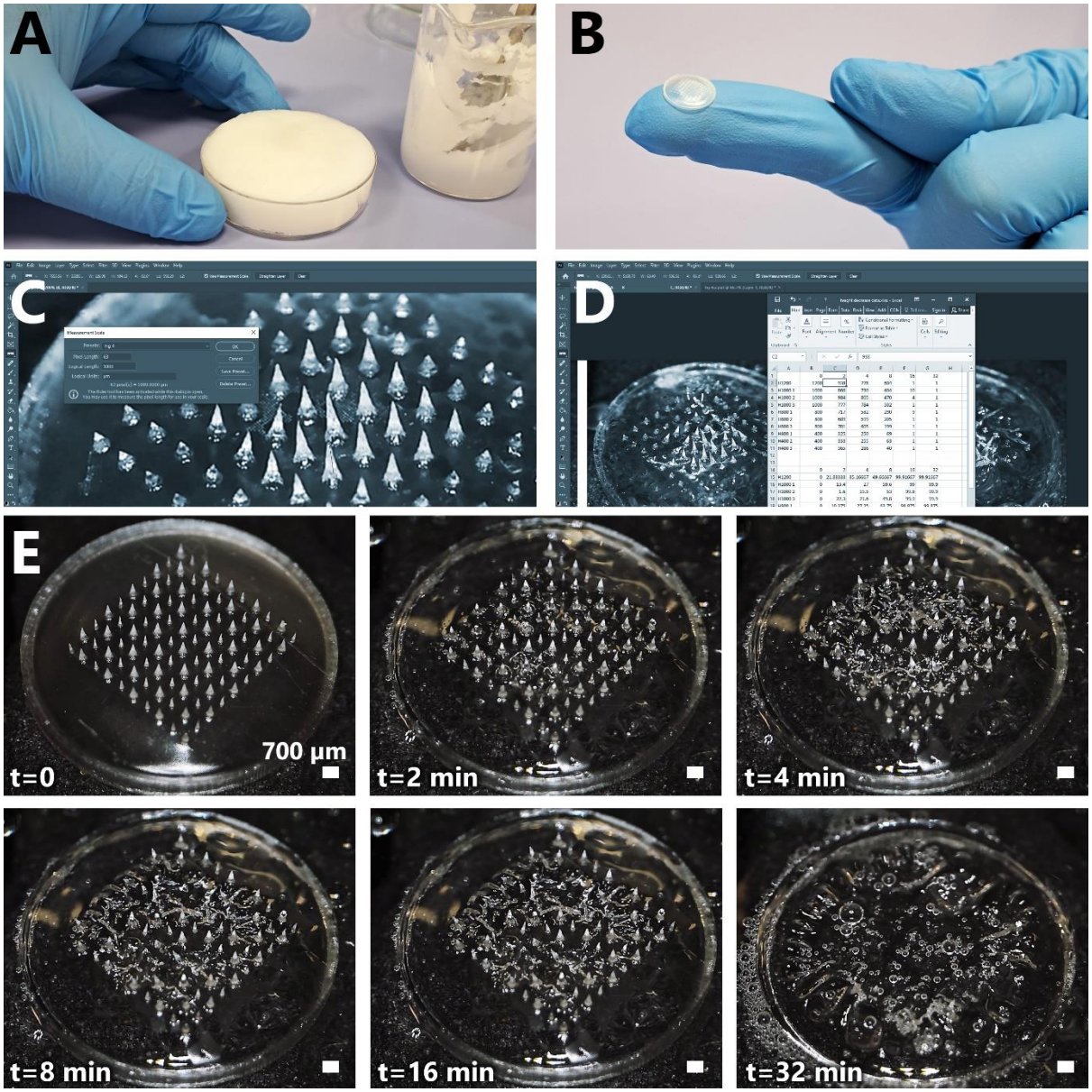

Supplementary Figure 5.S.2. Preparation of artificial human skin and characterization of MNAs drug delivery efficiency based on MN degradation. (A-B) Upon preparation of the solution resembling human skin, MNAs were inserted into it by hand. (C-D) Optical microscopic photos of the MNAs after insertion were taken. In these photos, size reduction of the needles for each geometry of the MNAs was inspected in Adobe Photoshop using Ruler Tool. (E) Within several time intervals, optical microscopic photos of the wave MNAs after insertion into artificial human skin were taken. Scale bars for all: 700 µm.

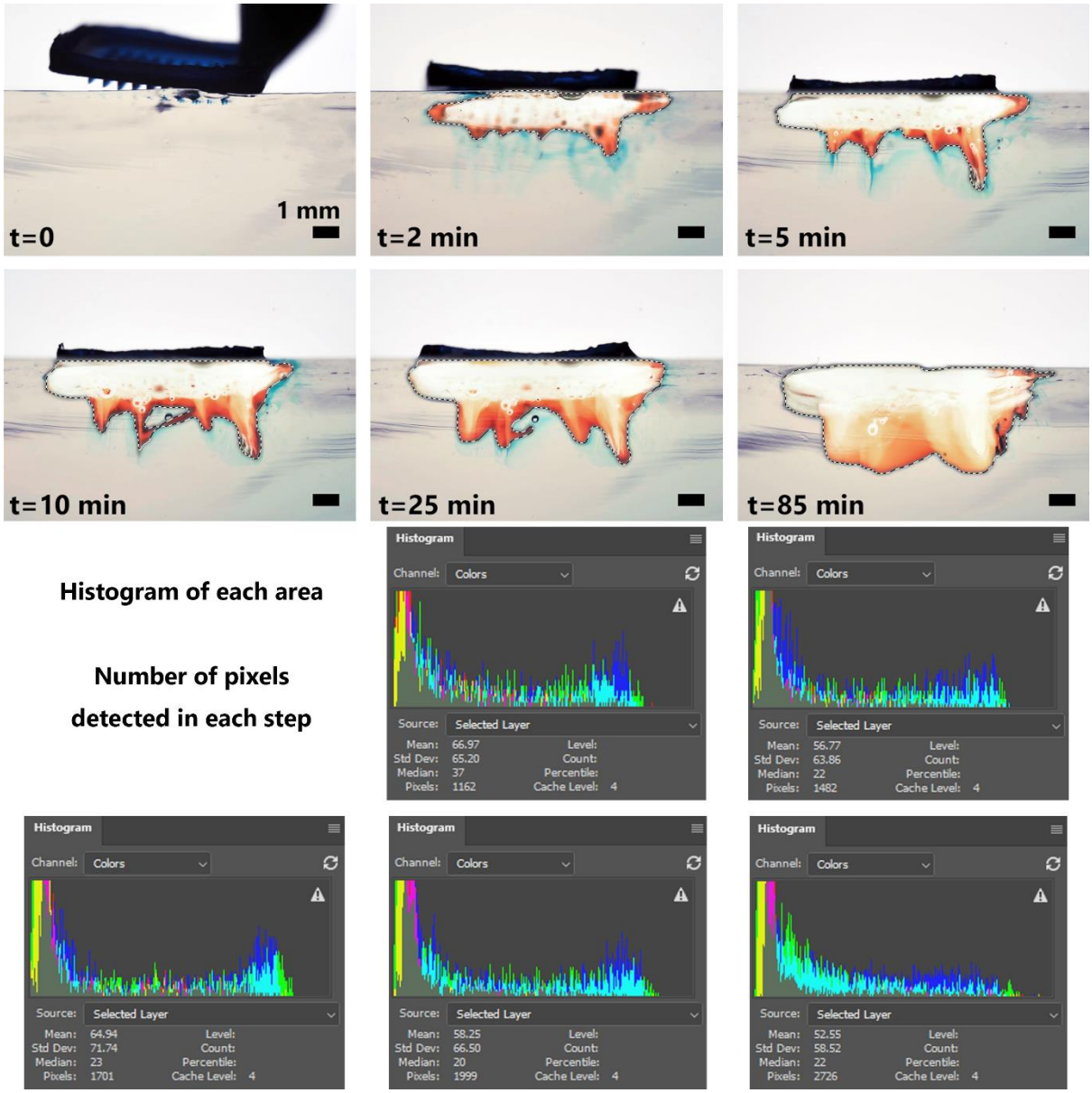

Supplementary Figure 5.S.3. Image analysis for characterization of MNAs' drug delivery efficiency based on MN degradation inside the bovine gel using number of detected pixels.

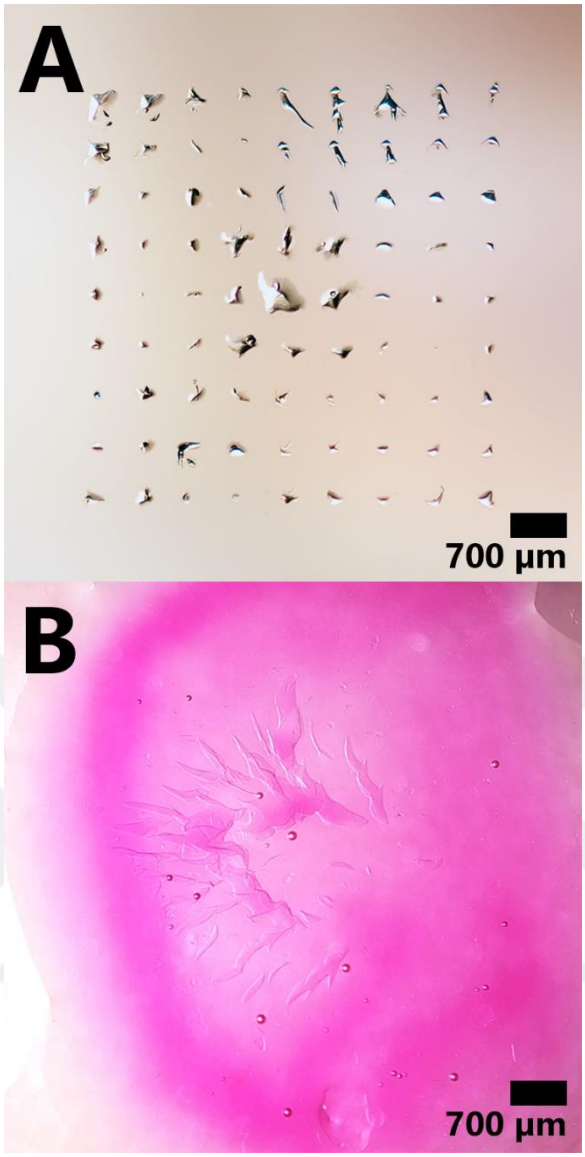

Supplementary Figure 5.S.4. (A) Top view of the gelatin right after removal of the inserted MNA (t=0) along with (B) top view of the gelatin after RhB delivery (t=40 min). Scale bars for all: 700 µm.